

Czech Technical University in Prague  
Faculty of Electrical Engineering  
Department of Physics

# The Study of a Fibre Z–Pinch

Ing. Daniel Klír  
Supervisor: Prof. RNDr. Pavel Kubeš, CSc.

A thesis submitted for the degree of Doctor of Philosophy  
PhD Programme: Electrical Engineering and Informatics  
Branch of Study: Plasma Physics

September 2005

## DECLARATION

I declare that this doctoral thesis has not been submitted as an exercise for a degree at this or any other university and that it is entirely my own work.

Prague, September 2005

Daniel Klír

## ACKNOWLEDGEMENTS

First of all, I would like to make grateful acknowledgement to my supervisor Prof. RNDr. Pavel Kubeš, CSc. (Faculty of Electrical Engineering, Czech Technical University in Prague) for his continued encouragement and kind help throughout my work on this thesis.

I also wish to express my gratitude to doc. Ing. Jozef Kravárik, CSc. (FEE, Czech Technical University in Prague) and the research teams at the Z–pinch facility S–300 (Kurchatov Institute, Moscow) and plasma focus device PF–1000 (Institute of Plasma Physics and Laser Microfusion, Warsaw) for their extensive assistance during our experiments.

I am also grateful to all who provided me with invaluable advice, inspiration, and encouragement. Prof. Dr. Hans J. Kunze (Ruhr Universität, Bochum) deserves special mention here.

I thank to the Ministry of Education of the Czech Republic (research programs INGO No. 1P2004LA235, No. 1P05ME761 and LC528), the Grant Agency of the Czech Republic (grant No. 202–03–H162) and Czech Technical University in Prague (research program No. 6840770016) for their financial support.

Finally, my sincere thanks go to my wife Michaela for her support.

## ABSTRACT

This thesis presents the results of fibre Z–pinch experiments carried out on the Z–150 device at the Czech Technical University in Prague. The generator that was used to drive the experiments consisted of one capacitor of  $3 \mu\text{F}$  capacitance. In the case of 20 kV charging voltage, the current was peaking at 80 kA with a 850 ns quarter period. The Z–pinch was formed from carbon fibres of 15  $\mu\text{m}$  diameter and 1 cm length. The discharge was observed by number of diagnostics which included a voltage probe, Rogowski coil, two filtered PIN diodes, a hard X–ray detector, gated XUV spectrograph, time-integrated X–ray pinhole camera, gated VUV pinhole camera, and schlieren system. This comprehensive set of diagnostics enabled us to describe the gross dynamics of the Z–pinch.

It was found out that after the breakdown a low density coronal plasma was formed while the fibre diameter remained almost unchanged. This low density corona (ion density of about  $10^{16} \text{ cm}^{-3}$ ) was carrying almost all the current of the order of 10 kA. When the current had built up, i.e. after about 150 ns, the implosion of the corona onto the central fibre occurred. The implosion velocity approached the value of  $2 \times 10^5 \text{ m s}^{-1}$ . When the imploded corona had reached the fibre, the dip in  $dI/dt$ , voltage peak up to 10 kV, and XUV pulse of a  $10 \div 30$  ns width were observed. XUV radiation was emitted from several bright spots which corresponded to the interaction of  $m = 0$  instability necks with the dense core. The electron temperature and density were approximately 80 eV and  $10^{19} \text{ cm}^{-3}$ , respectively. Although the presence of a fibre did not significantly suppress MHD instabilities, they were not disruptive.

After the fibre ablation, i.e. after 500 ns, material evaporated from electrodes started to play a dominant role. The observed plasma column seemed to be MHD unstable and when  $m = 0$  instabilities had developed, XUV, soft X–ray and hard X–ray pulses were emitted from several hot spots, particularly near the anode. At that time the voltage peak of up to 30 kV was detected.

In each phase of the discharge, the energetics of the Z–pinch and basic plasma parameters were estimated.

## CONTENTS

<i>Introduction</i> . . . . .	1
1. <i>Brief Survey of Z–Pinch Research and Application</i> . . . . .	3
1.1 Historical Perspective of Z–Pinches . . . . .	3
1.2 Present State and Applications of Z–Pinches . . . . .	8
1.2.1 Source of radiation . . . . .	8
1.2.2 Controlled thermonuclear fusion . . . . .	13
1.2.3 Other applications . . . . .	19
1.3 Fibre Z–pinch . . . . .	20
1.3.1 Cryogenic deuterium fibres . . . . .	20
1.3.2 Carbon and deuterated polyethylene fibres . . . . .	20
1.3.3 Contemporary state of art . . . . .	21
1.3.4 Fibre Z–pinch drivers . . . . .	21
1.3.5 Our experiment . . . . .	22
2. <i>Theoretical Background</i> . . . . .	26
2.1 Equilibrium Z–pinches . . . . .	26
2.1.1 Bennett equilibrium . . . . .	26
2.1.2 Pease–Braginskii current and radiative collapse . . . . .	28
2.1.3 Ideal MHD stability of equilibrium Z–pinch . . . . .	30
2.2 Dynamic Z–pinches . . . . .	34
2.2.1 Magnetic compression . . . . .	34
2.2.2 Stability of dynamic pinches . . . . .	35
3. <i>Apparatus and Diagnostics</i> . . . . .	37
3.1 Z–pinch Device Z–150 . . . . .	37
3.2 Current Generator . . . . .	39
3.3 Experimental Chamber and Vacuum System . . . . .	41

3.4	Z–pinch Load	43
3.5	Diagnostics	44
3.5.1	Voltage probe	45
3.5.2	Rogowski coil	45
3.5.3	Filtered PIN diodes	48
3.5.4	Hard X–ray detector	50
3.5.5	XUV spectrograph	52
3.5.6	X–ray pinhole camera	67
3.5.7	Gated VUV pinhole camera	69
3.5.8	Laser probing	69
3.6	Control and Synchronising Units	72
3.7	Digital Storage Oscilloscopes	73
4.	<i>Experimental Results</i>	74
4.1	Breakdown	75
4.2	Latent Stage	77
4.3	Plasma–on–Fibre	80
4.3.1	Implosion	81
4.3.2	Stagnation	86
4.3.3	Expansion	88
4.3.4	Multiple pulses	89
4.3.5	Experimental data interpretation	90
4.4	Fibre Ablation	96
4.5	Discharge in Electrode Vapour	97
4.5.1	Evaporation of material from electrodes	98
4.5.2	Magnetic pinching of evaporated material	98
4.5.3	Development of plasma instabilities	99
4.5.4	Experimental data interpretation	101
4.6	Z–pinch Disintegration	102
4.7	Energetics of Z–pinch	102
4.8	Influence of Electrodes	104
4.9	Various Fibre Diameters	106

5. Discussion . . . . .	107
5.1 Fibre Z–pinch Experiments . . . . .	107
5.2 Implosion of Coronal Plasma onto Central Fibre . . . . .	108
5.3 Wire–Array and Gas–Puff Implosion onto Central Fibre . . . . .	110
5.4 Plasma–on–Wire . . . . .	111
5.5 Discharge in Electrode Vapour and Bright Spots . . . . .	112
Summary, Conclusions and Prospects . . . . .	114
A. Applied Spectroscopic Methods . . . . .	136
A.1 Introduction . . . . .	136
A.2 Radiative Processes . . . . .	137
A.3 Collisional Processes in Plasma . . . . .	138
A.4 Charge State Distribution and Population of Energy Levels . . . . .	140
A.4.1 Charge state distribution . . . . .	140
A.4.2 Level populations . . . . .	141
A.5 Local Thermodynamic Equilibrium . . . . .	142
A.6 Prerequisites for Local Thermodynamic Equilibrium . . . . .	143
A.7 Radiative Transfer . . . . .	144
A.8 Intensity of Spectral Lines . . . . .	146
A.9 Spectroscopic Measurements of Plasma Parameters . . . . .	147
B. Code <i>FLY</i> . . . . .	149
B.1 Basic Parameters . . . . .	149
B.2 Description . . . . .	150
B.3 <i>FLY</i> . . . . .	150
B.4 <i>FLYPAPER</i> . . . . .	150
B.5 <i>FLYSPEC</i> . . . . .	150
B.6 Code Limitation . . . . .	151
B.7 Platform . . . . .	151
C. Deuterated Fibre Experiment on S–300 facility . . . . .	152
C.1 Introduction . . . . .	152
C.2 Apparatus and Diagnostics . . . . .	153
C.2.1 Current generator and Z–pinch load . . . . .	153

C.2.2	Diagnostics	153
C.3	Experimental Results	154
C.3.1	Current waveform and X-ray emission	154
C.3.2	Neutron measurements	156
C.4	Discussion	157
C.5	Conclusion	159
<i>D.</i>	<i>MATLAB Simulation of R–L–C Circuit with Time–Dependent Resistance</i>	160

## LIST OF FIGURES

1.1	Van Marum’s electrostatic generator in Teylers Museum . . . . .	3
1.2	Dynamic hohlraum . . . . .	14
1.3	Dynamic hohlraum created from two nested wire–arrays . . . . .	14
1.4	Static hohlraum with two $Z$ –pinch radiation sources at the ends . . . . .	15
2.1	Sausage instability, $m = 0$ . . . . .	31
2.2	Kink instability, $m = 1$ . . . . .	31
3.1	$Z$ –pinch device Z–150, Czech Technical University, Prague . . . . .	37
3.2	Block diagram of the Z–150 device . . . . .	38
3.3	Electric scheme of the Z–150 device . . . . .	39
3.4	“Short” circuit . . . . .	39
3.5	Damped oscillation of a “short” circuit . . . . .	40
3.6	Equivalent electric circuit of the discharge with a fibre . . . . .	40
3.7	Side-on view of the experimental chamber and spark gap . . . . .	41
3.8	End-on view of the experimental chamber . . . . .	42
3.9	Brass conical electrodes with a carbon fibre . . . . .	43
3.10	Upper cover of the experimental chamber . . . . .	43
3.11	Schematic diagram and picture of diagnostic set–up, end–on view . . . . .	45
3.12	Equivalent circuit of $dI/dt$ probe . . . . .	46
3.13	Reverse bias connection of PIN diodes . . . . .	48
3.14	Transmission of an Al and Be filter . . . . .	49
3.15	Spectral responsivities of PIN diodes . . . . .	50
3.16	Transmission of Al filters used together with a hard X–ray detector . . . . .	51
3.17	Rowland circle spectrograph . . . . .	53
3.18	LPS–VUV1–3S–M spectrograph . . . . .	54
3.19	Registration by a plane detector . . . . .	54
3.20	LPS–VUV1 spectrograph geometry of detection . . . . .	56

---

3.21	Example of a spectrum recorded by the UV-film UF-4	58
3.22	Calibration of wavelengths by an aluminium filter	58
3.23	Diffraction efficiency of gratings no. 1–4	61
3.24	Reflectivity of a gold thick layer for unpolarised light	62
3.25	Gold coated MCP detector with 4 stripes	62
3.26	Characteristic curve of the UF-4 film	64
3.27	Inverse sensitivity of films in the 2–14 nm region	64
3.28	Typical spectral dependence of quantum efficiency of MCPs	64
3.29	XUV spectrum together with a pinhole image	67
3.30	X-ray pinhole camera for time-integrated imaging	68
3.31	VUV pinhole camera for time-resolved imaging	68
3.32	Optical layout of the schlieren system, scale 1:30	71
3.33	Block diagram of synchronising a discharge and diagnostics	72
4.1	Waveforms of current, current derivative, voltage and PIN diode signals recorded in discharge no. 050128-1	75
4.2	Breakdown phase in discharge no. 050128-1	76
4.3	Latent phase in discharge no. 050128-1	77
4.4	VUV pinhole images recorded in the latent phase	79
4.5	XUV spectrum detected at 110 ns, shot no. 011016-1	79
4.6	Plasma-on-fibre phase in discharge no. 050128-1	80
4.7	VUV pinhole images detected in shot no. 030828-1. The collapse of a coronal plasma onto a fibre with the velocity of $2 \times 10^5 \text{ m s}^{-1}$	81
4.8	Zippering from the cathode with the velocity of $10^5 \text{ m s}^{-1}$	82
4.9	XUV pinhole images in shot no. 021031-1. Zippering with the velocity of $10^5 \text{ m s}^{-1}$	83
4.10	Temperature dependence of intensities of selected lines	84
4.11	XUV spectrum in shot no. 011031-3. Synthetic spectra simulated with FLY code for optically thin plasma	85
4.12	Ratio of Ly- $\alpha$ and He- $\alpha$ lines of carbon ions for optically thin plasma	85
4.13	Simultaneous XUV spectrum, schlieren and pinhole images exposed at the peak of the XUV pulse	86
4.14	Cooling after stagnation in discharge no. 040225-2	88
4.15	Expanded dense core and helix observed after the expansion	89

4.16	Experiment vs. MATLAB simulation of the $R$ – $L$ – $C$ circuit . . . . .	91
4.17	Observed $m = 0$ instability in shot no. 040421-1. Off-axis bright spots originated from the later stage of a discharge . . . . .	93
4.18	Schlieren images that recorded the ablation of a fibre . . . . .	96
4.19	Sharp density gradient near the cathode . . . . .	96
4.20	Discharge in electrode vapour . . . . .	97
4.21	Material evaporated from electrodes in shot no. 021024-2 . . . . .	98
4.22	Implosion of material evaporated from electrodes . . . . .	99
4.23	$Z$ –pinch plasma during the onset of an intensive X–ray pulse . . . . .	100
4.24	Time–integrated XUV spectrum, shot no. 050427-2 . . . . .	101
4.25	PIN diode signal together with the current waveform and signal of a Be–filtered PIN diode, shot no. 050512-1 . . . . .	103
4.26	Time–integrated visible and X–ray images, shot no. 040422-1 . . . . .	103
4.27	PIN diode signals for different materials and shapes of electrodes . . . . .	104
4.28	Comparison of two time–integrated XUV spectra when brass and steel electrodes were used . . . . .	105
4.29	VUV pinhole image in the discharge with bisectional electrodes made of stainless steel . . . . .	106
5.1	Spatially resolved X–ray spectrum recorded on the PF–1000 plasma focus.	111
A.1	Several possible radiative and collisional processes . . . . .	138
C.1	Diagnostic set–up on the S–300 generator, Moscow . . . . .	153
C.2	Current waveform, emitted power of soft X–rays, hard X–ray signal, and streak photograph, shot no. 030606-1 . . . . .	155
C.3	Time–integrated X–ray pinhole images and the sequence of gated X–ray images, shot no. 030606-1 . . . . .	155
C.4	XUV spectrum in the $200 \div 600$ eV spectral range, shot no. 030606-1 . . . . .	156
C.5	Scintillator signals in shot no. 030606-1, neutron yield $2 \times 10^7$ . . . . .	157
D.1	$R$ – $L$ – $C$ circuit with a time–dependent resistance . . . . .	160

## LIST OF TABLES

1.1	Electrical characteristics of the largest sub-microsecond Z–pinches . . . . .	9
1.2	Basic parameters of the largest microsecond Z–pinches . . . . .	10
1.3	Basic parameters of some Z–pinches with “pulse compression” . . . . .	11
1.4	Electrical characteristics of C, CH, CD and D fibre Z–pinches I . . . . .	23
1.5	Electrical characteristics of C, CH, CD and D fibre Z–pinches II . . . . .	24
1.6	Electrical characteristics of C, CH, CD and D fibre Z–pinches III . . . . .	25
3.1	Sub-systems of the Z–150 device . . . . .	38
3.2	Basic parameters of the Z–150 device . . . . .	41
3.3	Significant physical properties of carbon at 20°C and 100 kPa . . . . .	44
3.4	Significant energies of carbon atoms . . . . .	44
3.5	Basic parameters of the P6015 Tektronix HV probe . . . . .	45
3.6	Basic parameters of the Bicron BCF–12 scintillating fibre . . . . .	51
3.7	Basic parameters of the HAMAMATSU PMT tube . . . . .	51
3.8	Definition of wavelength ranges used in our work . . . . .	52
3.9	Basic parameters of the LPS–VUV1–3S–M spectrograph . . . . .	55
3.10	Basic parameters of the gratings . . . . .	55
3.11	Properties of the UF–4 ultraviolet film . . . . .	63
3.12	Parameters of MCP used as an active detector in our spectrograph . . . . .	63
3.13	Basic parameters of the CCD detector . . . . .	64
3.14	Resolving power of our spectrograph for some wavelengths, gratings and detectors . . . . .	66
4.1	Energetics of our fibre Z–pinch . . . . .	102

## LIST OF SYMBOLS

Throughout the thesis we use the following symbols representing physical quantities and constants.

Symbol	Physical quantity or constant	Unit
$a$	diameter of stop in schlieren system	m
$A$	area	$\text{m}^2$
$A$	atomic mass number	
$A$	constant in bremsstrahlung radiation $P_{\text{BS}}$ in Eq. 2.17	$\text{kg}^{1/2} \text{m}^4 \text{s}^{-2}$
$A_{u \rightarrow}$	transition probability for emission from level “u”	$\text{s}^{-1}$
$A_{ul}$	transition probability for emission from level “u” to “l”	$\text{s}^{-1}$
$b$	radius of experimental chamber	m
$\vec{B}$	magnetic field	T
$c$	speed of light in vacuum	$\text{m s}^{-1}$
$c_p$	isobaric specific heat	$\text{J K}^{-1}$
$c_s$	ion sound speed	$\text{m s}^{-1}$
$c_V$	isochoric specific heat	$\text{J K}^{-1}$
$C$	constant	
$C$	capacitance	F
$C_0$	capacitance of capacitor bank	F
$C_a$	probability of collision of one ion A with electrons	$\text{s}^{-1}$
$C_{u \rightarrow}$	probability of collision depopulating upper level “u”	$\text{s}^{-1}$
$d$	groove spacing of grating	m
$d_D$	thickness of dead layer	m
$d_F$	thickness of filter	m
$d_{\text{RES}}$	spatial resolution of pinhole camera	m
$d_S$	thickness of sensitive layer	m

Symbol	Physical quantity or constant	Unit
$D$	distance between grating centre and detector plane	m
$D_0$	fog density of film	
$\mathcal{D}$	diameter of lens	m
$e$	electric charge	C
$\vec{E}$	electric field	$\text{V m}^{-1}$
$E_1$	energy of ground state	J
$E_{\text{H}}$	ionization energy of hydrogen	J
$E_{\text{ion}}$	ionization energy	J
$E_{\text{l}}$	energy of lower level	J
$E_{\text{u}}$	energy of upper level	J
$f$	focal length of lens	m
$f_{\text{e}}(v)$	electron velocity distribution	$\text{m}^{-1} \text{s}$
$f_{\text{lu}}$	absorption oscillator strength ( $\text{l} \rightarrow \text{u}$ )	
$f_{\text{ul}}$	emission oscillator strength ( $\text{u} \rightarrow \text{l}$ )	
$F$	calibration factor	$\text{V/A s}$
$\vec{f}_p$	pressure gradient, force density	$\text{N m}^{-3}$
$\vec{f}_m$	magnetic force density	$\text{N m}^{-3}$
$g$	gain coefficient	$\text{m}^{-1}$
$g$	gravitational acceleration	$\text{m s}^{-2}$
$\bar{g}$	average Gaunt-factor	
$g_{\text{i}}^z$	statistical weight of level “i” in ionic stage $z$	
$g_{\text{l}}$	statistical weight of lower level “l”	
$g_{\text{u}}$	statistical weight of upper level “u”	
$G$	conductance	$\Omega^{-1}$
$h$	Planckian constant	$\text{J K}^{-1}$
$i_{\text{PIN}}$	current generated in PIN diode	A
$i_{\text{C}}$	current induced in Rogowski coil	A
$I$	relative intensity of spectral line	
$I$	electric current	A
$I(r)$	current flowing inside radius $r$	A
$I_0$	total current in Z-pinch	A

Symbol	Physical quantity or constant	Unit
$I_{\text{PB}}$	Pease–Braginskii current	A
$\vec{j}$	current density	$\text{A m}^{-2}$
$k$	axial wave number	$\text{m}^{-1}$
$k$	Boltzmann constant	$\text{J K}^{-1}$
$l$	length of pinch column or active media	m
$l$	distance between grating centre and spectral line	m
$l$	wave function of lower level “l”	
$l_{\Omega}$	characteristic length along line of sight	m
$L$	inductance	H
$L_0$	inductance of a short circuit	H
$L_C$	inductance of Rogowski coil	H
$L_P$	plasma inductance	H
$L_S$	inductance of solenoid	H
$L_{\nu}$	spectral radiance	$\text{W m}^{-2} \text{ sr}^{-1} \text{ Hz}^{-1}$
$m$	azimuthal wave number	$\text{rad}^{-1}$
$m$	diffraction order	
$m_e$	electron mass	kg
$M$	magnification of image	
$M_i$	ion mass	kg
$n, n_i$	density of ions, plasma density	$\text{m}^{-3}$
$n_A$	density of ions A	$\text{m}^{-3}$
$n_e$	electron density	$\text{m}^{-3}$
$n_{\text{TH}}$	thermal limit	
$n_u$	number density of electrons in upper level	$\text{m}^{-3}$
$n^z$	density of ionization stage $z$	$\text{m}^{-3}$
$N$	refractive index	
$N_a, N_i$	atom line density, ion line density	$\text{m}^{-1}$
$p$	kinetic pressure	Pa
$P_J$	Ohmic power	W
$P_R$	radiated power	W
$Q$	fusion gain	
$Q^z(T_e)$	partition function of ionic stage $z$	

Symbol	Physical quantity or constant	Unit
$r$	radial coordinate	m
$r_B$	Bohr radius	m
$\vec{r}$	displacement vector	m
$\vec{r}^0$	unit vector in radial direction	m
$R$	pinch radius	m
$R$	resistance	$\Omega$
$R_a$	number of transitions “a” per unit time and per unit volume	$s^{-1} m^{-3}$
$R_{u \rightarrow}^c$	rate of collisions depopulating upper level “u”	$s^{-1} m^{-3}$
$R_{\rightarrow u}^c$	rate of collisions filling upper level “u”	$s^{-1} m^{-3}$
$R_{r \rightarrow u}^r$	rate of radiative processes filling upper level “u”	$s^{-1} m^{-3}$
$R_0$	initial pinch radius	m
$R_0$	initial resistance	$\Omega$
$R_C$	resistance of Rogowski coil	$\Omega$
$R_G$	radius of grating curvature	m
$R_L$	resistance of load	$\Omega$
$R_P$	plasma resistance	$\Omega$
$R_R$	radius of Rowland circle	m
$\mathcal{R}$	resolving power of spectrograph	
$\mathcal{R}_{\max}$	maximum attainable resolving power	
$\mathcal{R}_i$	responsivity	$A W^{-1}$
$s$	distance between entrance slit and grating centre	m
$S$	ionization rate coefficient	$m^3 s^{-1}$
$S$	Lundquist number	
$S^*$	critical Lundquist number	
$S_\nu(\vec{r})$	source function	$W m^{-2} sr^{-1} Hz^{-1}$
$\mathcal{S}_\lambda$	film sensitivity	$J cm^{-2}$
$\mathbb{S}$	total electron spin quantum number	
$t$	time	s
$t_0$	beginning of implosion	s
$t_{10\%-90\%}$	rise time	s

Symbol	Physical quantity or constant	Unit
$T$	temperature	K, eV
$T_B$	Bennett temperature	K, eV
$T_{1/4}$	quarter period of oscillation circuit	s
$T_e$	electron temperature	K, eV
$T_i$	ion temperature	K, eV
$u$	wave function of upper level “u”	
$U$	voltage	V
$U_0$	charging voltage	V
$U_{osc}$	voltage at oscilloscope	V
$v$	velocity	$\text{m s}^{-1}$
$v_A$	Alfvén velocity	$\text{m s}^{-1}$
$v_{De}$	electron drift velocity	$\text{m s}^{-1}$
$v_{exp}$	expansion velocity	$\text{m s}^{-1}$
$v_{imp}$	implosion velocity	$\text{m s}^{-1}$
$v_{Ti}$	thermal ion velocity	$\text{m s}^{-1}$
$V$	volume	$\text{m}^3$
$w$	energy need for creation of one electron–hole pair in Si	J
$W$	width of grating in dispersion plane	m
$W_{imp}$	energy delivered to the axis during the implosion	J
$x$	distance between spectral line $\lambda_0$ and the zeroth order	m
$x_0$	distance between the zeroth order and perpendicular from grating centre upon detector	m
$x_\lambda$	distance between spectral line $\lambda$ and perpendicular from grating centre upon detector	m
$X$	collisional excitation/deexcitation rate coefficient	$\text{m}^3 \text{s}^{-1}$
$X_{\rightarrow u}$	excitation rate coefficient of upper level “u”	$\text{m}^3 \text{s}^{-1}$
$X_{l \rightarrow u}$	excitation rate coefficient of upper level from lower level	$\text{m}^3 \text{s}^{-1}$
$X_{u \rightarrow}$	deexcitation rate coefficient of upper level “u”	$\text{m}^3 \text{s}^{-1}$
$X_{u \rightarrow l}$	deexcitation rate coefficient of upper level to lower level	$\text{m}^3 \text{s}^{-1}$
$y$	location of imaged point on entrance slit	m

Symbol	Physical quantity or constant	Unit
$z$	axial coordinate	m
$z$	effective nuclear charge, ionic charge	
$\bar{z}$	average ion charge	
$\vec{z}^0$	unit vector in axial direction	m
$Z$	atomic number	
$Z_0$	characteristic impedance	$\Omega$
$\alpha$	recombination coefficient	$\text{m}^3 \text{s}^{-1}$
$\alpha$	angle between grating plane and spectrograph axis	m
$\beta(r)$	$2\mu p(r)/B(r)$	
$\gamma$	ratio of specific heats	
$\gamma_\lambda$	film contrast	
$\Gamma$	exponential factor	$\text{s}^{-1}$
$\Gamma_z$	flux density of ions of charge $z$	$\text{m}^{-2} \text{s}^{-1}$
$\delta\lambda$	spectral resolution	m, nm
$\Delta E_{ul}$	energy difference between level “u” and “l”	J
$\epsilon_\nu$	emissivity / volume emission coefficient	$\text{W m}^{-3} \text{sr}^{-1} \text{Hz}^{-1}$
$\epsilon_0$	vacuum permittivity	$\text{F m}^{-1}$
$\eta$	viscosity	$\text{kg s}^{-1} \text{m}^{-1}$
$\eta$	quantum efficiency	
$\kappa(\nu, \vec{r})$	effective absorption coefficient	$\text{m}^{-1}$
$\lambda$	period of perturbation	$\text{m}^{-1}$
$\lambda$	wavelength	m, nm
$\lambda_0$	focused wavelength	m, nm
$\lambda_0$	wavelength of line centre	m, nm
$\lambda_B$	blaze wavelength of grating	m, nm
$\Lambda$	$\ln \Lambda$ is Coulomb logarithm	
$\mu$	permeability	$\text{H m}^{-1}$
$\mu_D$	absorption coefficients of dead layer	$\text{m}^{-1}$
$\mu_F$	absorption coefficients of filter	$\text{m}^{-1}$
$\mu_S$	absorption coefficients of sensitive layer	$\text{m}^{-1}$

Symbol	Physical quantity or constant	Unit
$\nu$	photon frequency	Hz
$\nu_0$	photon frequency of line centre	Hz
$\pi$	Ludolphian number	
$\rho$	mass density	$\text{kg m}^{-3}$
$\rho_i$	average ion Larmor radius	m
$\bar{\rho}$	average mass density	$\text{kg m}^{-3}$
$\sigma$	specific conductivity	$\text{S m}^{-1}$
$\sigma_{\text{Spitzer}}$	Spitzer conductivity (Spitzer, 1962)	$\text{S m}^{-1}$
$\sigma(\nu)$	microscopic cross-section of process	$\text{m}^{-2}$
$\sigma_0$	coefficient in Spitzer conductivity $\sigma_0(kT_e)^{3/2}/(\bar{z} \ln \Lambda)$	$\text{S m}^{-1} \text{J}^{-3/2}$
$\tau$	confinement time	s
$\tau$	time when instabilities first appears	s
$\tau(\nu, \vec{r})$	optical depth	
$\tau_A$	Alfvén transit time	s
$\tau_i$	ion-ion collision time	s
$\tau_u$	life time of upper level “u”	s
$\phi_0$	grazing angle of incidence	m
$\phi$	grazing angle of diffraction	m
$\Phi$	incident power of radiation	W
$\theta$	azimuthal angle, coordinate	rad
$\vec{\theta}^0$	unit vector in azimuthal direction	m
$\vartheta$	deflection angle of laser beam	rad
$\vec{\xi}$	Lagrangian displacement	m
$\omega$	angular frequency	$\text{rad s}^{-1}$
$\omega_{ci}$	ion cyclotron frequency	$\text{rad s}^{-1}$
$\Omega$	solid angle	srad
$\emptyset$	diameter of pinhole	m, $\mu\text{m}$

## INTRODUCTION

The major concern of this thesis is a *Z*–pinch which belongs to one of the most fascinating objects in plasma physics due to its natural occurrence and variety of applications. A *pinch* is defined as plasma configuration in which an electric current generates magnetic field that tends to confine the plasma (cf. Spielman and de Groot, 2001). The prefix “*Z*” was added in the 1950s to denote the confinement driven by an axial (*z*) current.

### *Scope of Thesis: Fibre Z–pinch Experiments in Vacuum*

First, it should be stressed that this thesis does not focus on *Z*–pinches in general but is limited to the so–called *fibre Z–pinch*. *Z*–pinches could be initiated by electrical power sources from various discharge loads (gas, wire, low–density foam, cylindrical array of wires, cylindrical foil, etc.), however, we are studying mainly the pinch formed from a fibre with few micrometers in diameter. In our work we distinguish between a fibre and a wire. The expression “fibre” here means a wire with a very low conductivity, such as cryogenic deuterium, deuterated polyethylene, carbon, etc. The reason for making such distinction is that the dynamics of a fibre *Z*–pinch substantially differs from the behaviour of a metal wire, such as aluminium, copper, gold.

Furthermore, *Z*–pinch discharge can occur in vacuum, gas, water, etc. So far our research has been restricted to discharges *in vacuum*.

As far as the experimental study is concerned, the fibre *Z*–pinch was carried out on a slow current generator *Z*–150 at the Czech Technical University in Prague. Nevertheless, we also performed experiments<sup>1</sup> on more powerful *S*–300 generator at Kurchatov Institute, Moscow.

---

<sup>1</sup> To draw a comparison between these two experiments, the results from *S*–300 device are included in appendix C.

## *Aim of Thesis*

We aim at presenting the most important results of our Z–pinch research at the Department of Physics, Faculty of Electrical Engineering, CTU in Prague. The primary objective of our research is the *description of our fibre Z–pinch dynamics* because to our knowledge no systematic effort has been made to study a Z–pinch initiated from a carbon fibre in vacuum using a low voltage capacitive discharge. We believe that our findings help us to get deeper insight into processes taking place in Z–pinches.

## *Layout of Thesis*

The thesis is organised as follows:

Chapter 1 presents a brief survey of the past and present Z–pinch research. The emphasis is put on applications of a Z–pinch in controlled thermonuclear fusion and as a powerful source of X–ray radiation. The last part of this chapter is devoted to fibre Z–pinches which were treated in more detail.

Chapter 2 provides basic theoretical background for equilibrium and dynamic Z–pinches and thus creates the ground to which following chapters inevitably refer.

Chapter 3 describes in detail the current generator and diagnostics used in our experiment at the Czech Technical University.

Chapter 4 brings forward the most important results we have obtained. The results are shown chronologically, i.e. according to the phase in which they were recorded. Experimental data interpretation is given after each phase of our Z–pinch.

Chapter 5 contains the overall discussion within the framework of other experiments too.

Finally, the main results are summarised, and conclusions together with research prospects are presented.

## *Author's Share in Experiment*

The experiment itself has been carried out mainly by doc. Jozef Kravárik, CSc. The author's place was in data acquisition, data processing (XUV spectroscopy, X–ray optics, theory of detection) and elementary interpretation of results (Z–pinch physics). Chapters 3–5 together with conclusions are examples of his own work.

## Chapter 1

### BRIEF SURVEY OF Z-PINCH RESEARCH AND APPLICATION

#### 1.1 *Historical Perspective of Z-Pinches*

The following section was based on Sethian (1997); Liberman et al. (1999); Ryutov et al. (2000); Haines et al. (2000); Spielman and de Groot (2001); Sweeney (2002).

##### *Early beginnings of Z-pinches*

The first experimental study of “Z-pinch” could be assigned to the Dutch chemist and physicist Martinus van Marum. In the late of the 17th century, he designed and used a large electrostatic generator (see Fig. 1.1) that was built by an English instrument–maker John Cuthbertson in Amsterdam.



*Fig. 1.1: Van Marum's electrostatic generator in Teylers Museum (Teylers Museum, 2005).*

The machine consisted of two parallel rotating glass discs (1.62 m in diameter) and four–man power. Its 100 capacitors (“Leyden Jars”) were 4 mm thick Bohemian glass bottles of about 35 cm diameter and 60 cm hight. The capacitance of a single jar was

around 5 nF and hence the total capacitance was 0.5  $\mu$ F. The permissible voltage might have been over 60 kV, in which case the bank's energy was at least 1 kJ<sup>1</sup>. At the time when van Marum carried out experiments with exploding wires, the expected discharge time was about 0.5  $\mu$ s and a peak current of 60 kA.

The term “pinch” and also the first systematic research of Z–pinches, however, began in the 20<sup>th</sup> century. In 1905, Pollock and Barracough observed the distortion of a lighting conductor caused by the  $\vec{j} \times \vec{B}$  force. In 1934, W. H. Bennett derived the well-known *equilibrium* of magnetically self–focusing streams of charged particles with a temperature  $T_B$  (see subsection 2.1.1 and Bennett, 1934). About three years later, L. Tonks resumed the Bennett theory and introduced the term “pinch” to describe the self–constricted plasma.

### Z–pinches for fusion

The growing interest in Z–pinches started in the 1950s in conjunction with controlled thermonuclear fusion research. The D–T Z–pinch, in which an electric current both heats and confines a plasma, was suggested to be a possible fusion system (see Haines, 1996). This idea was supported by a high number of neutrons ( $10^8$  per one pulse) observed in the first experiments with deuterium gas (20 kV capacitor bank and 1.5  $\mu$ s implosion time). Later, Anderson with his colleagues showed that neutrons were not produced by a Maxwellian plasma. He proposed that the deuterons were accelerated by axial electric fields created by the growth of  $m = 0$  instabilities (Anderson et al., 1958). This was consistent with Kurchatov's explanation (Kurchatov, 1957), Kruskal's and Schwarzschild's theoretical work (Kruskal and Schwarzschild, 1954), and earlier experiments carried by Carruthers and Davenport, 1957.

Despite this fact, further experiments were carried out on the Columbus-II machine at Los Alamos and the SuperFast Pinch (300 kA, 20 kA/ns) at Space Technology Laboratories. The idea was to use a fast driver to reach fusion conditions before instabilities could grow. Unfortunately, this approach did not achieve the results either and a plasma still exhibited MHD instabilities.

The problem of MHD stability was investigated to a large extent also in the 1950s. The basic stability criteria were established (Kadomtsev, 1963)<sup>2</sup>. These derived criteria showed that it is impossible to eliminate instabilities in cylindrical configurations. For

<sup>1</sup> With this machine, van Marum was able to create 60 cm long sparks in the air. In this experiment, the voltage was over 330 kV and the energy was 30 kJ (Spielman and de Groot, 2001).

<sup>2</sup> Especially the energy principle helped in quantifying plasma instabilities.

instance, toroidal systems of magnetic confinement that were also free from electrode phenomena seemed to be more stable. All these facts together with the conclusion that neutrons were not of thermal origin led to the abandonment of *linear* Z-pinch as a fusion power source. As a result, more complex schemes of magnetically confined plasma devices (such as the Tokamak) were suggested and researched in an attempt to reduce MHD instabilities.

### *Z-pinches as sources of radiation*

In the 1960s, Z-pinches were used as efficient UV, XUV and soft X-ray sources. The first Z-pinch X-ray sources were exploding wires of  $10 \div 100 \mu\text{m}$  diameters (Chace and Moore, 1968). The typical parameter of discharges was the charging voltage of tens of kilovolts. The capacitor banks were discharged into a load via spark gaps with microsecond discharge time. The Z-pinch plasma reached usually the temperature of  $10 \div 100 \text{ eV}$ . The peak electron density was up to  $10^{21} \text{ cm}^{-3}$ . Because the absorption mean free path was less than the diameter of a plasma column, the plasma radiation was close to the one of the blackbody.

Greater interest in Z-pinches was renewed in association with the development of nanosecond pulsed-power technologies in the 1970s. These drivers were able to deliver MV voltages, MA currents and TW electrical powers to a load. The new pulsed-power generators were used to drive single wires. The limitation of a single wire was its high initial impedance of  $\approx 1 \Omega$  that limited the conversion of the stored electrical energy to radiation. It was found that the implosion of a plasma onto its axis is a more effective way to generate radiation than resistive and compressional heating of an equilibrium plasma column (Linhart, 1961; Turchi and Baker, 1973; Stallings et al., 1976). For that reason, a single wire was replaced by e.g. a cylindrical array of wires, a thin cylindrical foil, an annular gas puff, a low-density foam cylinder, etc. In these configurations, the stored electrical energy is converted into the kinetic energy of magnetically confined, imploding plasma. At the stagnation, the kinetic energy is thermalised and the significant part of energy is radiated in sub-keV and keV radiation. This way, Z-pinches have become powerful radiation sources with X-ray powers at levels previously attainable only on the largest laser facility. Some current applications of Z-pinches as radiation sources will be given in subsection 1.2.1.

As regards the physics of a cylindrical load, it substantially differs from that of a sin-

gle wire or fibre. In the case of a single wire with a diameter of the order of ten micrometers, the time needed for establishing radial equilibrium is usually much shorter than the duration of a current pulse. That is why the pinch is assumed to be in the Bennett equilibrium. Ohmic and compressional heating are the most important. Such pinch is classified as *equilibrium*.

In the case of a cylindrical load with the initial diameter of a few centimetres, the implosion time is comparable with the driving current pulse. When the implosion stops, the plasma starts to expand and never reaches the Bennett-type equilibrium. The kinetic energy of implosion is the most dominant process of energy deposition into a plasma. Such pinches are called *dynamic*.

### *Rebirth of Z-pinch fusion research*

The progress in pulsed-power technology led to new attempts in using Z-pinches in fusion research. The “classical” effort pursued at Imperial College, Naval Research Laboratory, and Los Alamos National Laboratory was to develop a stable linear Z-pinch.

One of the first experiments was carried out with *compressional Z-pinch* at Imperial College, London in the late 1970s. The Z-pinch was created in a quartz tube of 1 cm diameter containing a deuterium filling. The discharge started on the insulating wall and the electric current (100 kA peak, 100 ns rise time) created the imploding plasma shell which was preceded by a shock-wave. Though a high number of neutrons was observed ( $10^{12}$  neutrons per shot), a low ion temperature indicated that neutrons were not produced by a Maxwellian plasma. Similar results were obtained at a 3 MA current on the Angara 5-1 device in Troitsk, Soviet Union (Batyunin, 1990).

Another attempt was not only to use a fast driver to reach fusion conditions before instabilities could grow but also to employ the effect of radiative collapse (cf. subsection 2.1.2 on page 28). In order to achieve magnetic fusion, Z-pinches should operate at the Pease–Braginski current (1.4 MA for hydrogen). Haines and Hammel derived the current waveform that is necessary to follow so as to keep the plasma column at a constant diameter. The temperature of 10 keV requires a current channels of  $\approx 100 \mu\text{m}$  diameter (Hammel et al., 1983). In order to have  $100 \mu\text{m}$  current channel, it seemed convenient to start with a small initial diameter of a plasma column. Therefore, the pinch was initiated by a focused laser or electron beam that ionised a channel on the axis — this is how a *gas-embedded* pinch is formed.

One of experiments with gas-embedded pinches was pursued at Los Alamos (High Density Z-Pinch experiments). These gas-embedded experiments demonstrated the possibility of producing  $m = 0$  stable Z-pinches (Hammel et al., 1983). However, these pinches could not reach multi-hundred eV temperatures because they rapidly accreted particles from the surrounding gas. In order to overcome this problem, the research group in Naval Research Laboratory formed the pinch inside small quartz capillary of 100  $\mu\text{m}$  inner diameter. A capillary reduced the accretion and the occurrence of MHD instabilities but its wall also caused rapid cooling of a plasma. It was a bad news for fusion purposes but on the other hand it seemed promisingly for a recombination mechanism for X-ray lasers (Rocca et al., 1988).

Different suggestion how to overcome the accretion was to initiate Z-pinch from very small diameter fibres of cryogenic solid deuterium in vacuum (Scudder, 1985). As it is the subject of our thesis, the research of *fibre Z-pinches* will be described in its own section 1.3.

Nowadays, a simple linear Z-pinch is not considered to be a feasible source for fusion energy (Sethian, 1997). Current applications of Z-pinches for fusion will be described in the following section.

## 1.2 Present State and Applications of Z-Pinches

There are numerous applications of Z-pinches at present but among the most important ones belong the pinches used (i) in controlled thermonuclear fusion research and (ii) as efficient sources of radiation. Since the use of a Z-pinch in fusion research is closely connected with its application as a radiation source, we begin with the description of the latter one first.

### 1.2.1 Source of radiation

Currently, the most important application of (dynamic) Z-pinches is their use as X-ray sources. Attractive properties of Z-pinches are mainly the simplicity of design, high power density, high X-ray energy output, and very high efficiency of transformation of stored electrical energy to radiation.

#### *Source of blackbody radiation*

Sandia's Z machine is now the most powerful X-ray source that is capable to generate nearly 2 MJ of thermal X-rays with a peak power of 280 TW in one pulse (Matzen, 1997; Deeney et al., 1998; Matzen et al., 1999). More than 15% of the stored electrical energy of 11.5 MJ is converted into X-rays. Such a high peak power and radiated energy were achieved as a result of the implosion of very high-wire-number arrays (Sanford et al., 1996; Deeney et al., 1997; Spielman et al., 1998) and nested wire-arrays (Deeney et al., 1998). As the implosion of high-Z material happened in the closed cavity, the radiation became close to the one of the blackbody.

The primary interest of the research is to use Z-pinch sources for inertial confinement fusion (see paragraph 1.2.2). However, there are other reasons for studying these X-ray sources which are also unique for other high-energy-density physics experiments:

- the study of radiation hydrodynamics (Olson et al., 1997), radiation transport, opacity measurements (Bailey et al., 2002a),
- the study of material properties under extreme conditions (Olson et al., 1997), shock physics, measurement of the equation of state under multi-mega-bar pressure,
- the laboratory study of weapons processes, survivability of weapons systems, etc.

Name	Location	Current [MA]	Rise time [ns]	Energy [kJ]	Power [TW]	Impedance [ $\Omega$ ]	Ref.
Z	SNL, USA	20	105	11400	50	0.12	(Spielman et al., 1997)
Saturn	SNL, USA	10.5	40	4000	32	0.11	(Spielman et al., 1989)
Angara 5-1	Triniti Troitsk, Russia	5	90	1400	9	0.25	(Grabovsky E., 2001)
S-300	Kurchatov Institute Moscow, Russia	4	70	920	8	0.15	(Chernenko et al., 1996)
Double Eagle	Physics International San Leandro, USA	4	100		7	0.33	(Sincerny et al., 1985)
Ambiorix	CEA Bruyeres Le Chatel, France	2.4	50	300	6	0.5	
MIG	HCEI Tomsk, Russia	1.9	80			0.65	(Sorokin and Chaikovsky, 2002)
MAGPIE	Imperial College London, Great Britain	1.4	150	336	1	1.25	(Mitchell et al., 1996)
NTF “Zebra”	University of Nevada Reno, USA	1.2	100	200	1	1.9	(NTF, 2005)

Tab. 1.1: Electrical characteristics of the largest sub-microsecond Z-pinchers.

At this point it might be useful to give the list of the largest pulsed power facilities used in Z-pinch mode (see Tab. 1.1). The list of devices may not be complete since there are more pulsed power generators that can be used in Z-pinch mode. However, they are mainly used as bremsstrahlung diodes or as accelerators of charged particles.

For next generation of Z-pinch facilities it is important to know scaling laws. Therefore, recent experiments on Sandia's Z machine (and be it said that not only there) were focused on the scaling of X-ray emission with a current (Stygar et al., 2004). They found that the total radiated X-ray energy varied as  $I^{1.73 \pm 0.18}$  and the peak power varied as  $I^{1.24 \pm 0.18}$ . Nevertheless, recent experiments close to  $I^2$  law are more perspective for future generators.

#### *Source of kiloelectronvolt radiation*

Besides being excellent Planckian-like X-ray sources, Z-pinches are also sources of non-LTE, K-shell or L-shell radiation. Ne, Kr or Ar gas puffs and Al, Ni or Ti wire-arrays have proven to be powerful sources of kiloelectronvolt emission (see a nice review written by Pereira and Davis, 1988). As an outstanding example we could mention Sandia's experiments with an argon double-shell Z-pinch. Sze et al. (2001) reported K-shell X-ray output of 274 kJ in a 15 TW peak power and 12 ns FWHM pulse.

#### *Long-implosion-time Z-pinches*

As was mentioned above, the interest in Z-pinches was renewed with the development of pulsed power generators that are low impedance ( $\lesssim 1\Omega$ ) water-line systems producing mega-ampere currents with 100-ns rise time. These fast high-current generators are very large and require high voltages. In order to reduce the complexity and cost of generators, lower voltage, long-implosion-time (0.1  $\mu$ s  $\div$  2  $\mu$ s) plasma radiation sources (PRS) have been studied. A comprehensive review was given by Deeney et al. (2001).

Name	Location	Current	Rise time	Energy
Atlas	LANL, USA	40 $\div$ 50 MA	5 $\div$ 10 $\mu$ s	36 MJ
Shiva	Air Force Research Laboratory, USA	12 $\div$ 30 MA	8 $\div$ 10 $\mu$ s	9.4 MJ
Pegasus	LANL, USA	6 $\div$ 12 MA	4 $\div$ 8 $\mu$ s	4.3 MJ

Tab. 1.2: Basic parameters of the largest microsecond Z-pinches.

Experiments on Shiva and Pegasus drivers<sup>3,4</sup> showed that Z–pinches with very long implosion times ( $\approx 1 \mu\text{s}$ ) were efficient, high–yield X–ray sources but that the peak power was not so high as in the case of 100–ns–class implosions.

The significant increase in the radiated power was achieved when plasma flow switches and flux compression were used to reduce the implosion times from microseconds to the hundreds of nanoseconds. Currently, experiments with plasma radiating sources are being pursued on the devices listed below in Tab. 1.3.

Name	Location	Current	Rise time	Note
Decade Quad	Titan San Leandro, USA	8 MA	300 ns	Flux compr. 15 MA in constr.
ECF2	Centre d'Etudes Gramat, France	5 MA	200 ns 1200 ns	Flux compr. 10 MA in constr.
ACE–4	Maxwell Laboratories San Diego, USA	2.5 MA 4 MA	100 ns 2000 ns	POS
GIT–12	HCEI Tomsk, Russia	2.5 MA 4.6 MA	70 ns 1600 ns	POS

Tab. 1.3: Basic parameters of several Z–pinches with “pulse compression”.

A longer ( $\approx 200 \text{ ns}$ ) implosion time is researched not only as a low–cost plasma radiating source but also as a possible approach<sup>5</sup> to the next generation of drivers with the current above 20 MA. It was one of the reasons why a long–pulse mode is also investigated on Double Eagle, Saturn and Z drivers (Deeney et al., 1999; Spielman et al., 1998). Although it is clear that long–implosion–time Z–pinches still need to be improved, the energy output and radiated power are comparable to those achieved with less than 100–ns implosion–times.

### X–ray laser

During the 1980s, some researchers held belief that powerful Z–pinches (such as Double Eagle, BlackJack 5, Gamble II, and Saturn) could be used for X–ray laser pumping.

<sup>3</sup> Their characteristics are displayed in Tab. 1.2.

<sup>4</sup> The largest devices, such as Atlas, Shiva, etc. were not primarily built for radiation experiments but for conducting hydrodynamic experiments supporting weapons–physics experiments.

<sup>5</sup> The rise time of a current is given by  $dI/dt \approx U/L_0$ . Therefore, if we want to achieve higher currents with an unchanged voltage  $U$  and inductance  $L_0$ , it is necessary to prolong rise time.

There were two main reasons supporting this idea. Firstly, the Z-pinch geometry with plasma lengths in centimetres and diameters in millimetres is naturally favourable for X-ray lasers (Elton, 1990). Secondly, Z-pinches can effectively deliver high energy density (up to  $10 \text{ MJ/cm}^{-3}$ ) into a plasma.

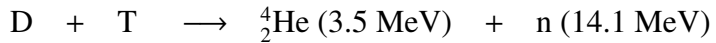
As far as a pinch plasma is concerned, the population inversion was demonstrated by resonant photopumping (Porter et al., 1992), recombination pumping (Steden and Kunze, 1990; Kunze, 1994; Shin et al., 1996; Ellwi et al., 2000, 2001; Metzner et al., 1996; Koshelev et al., 1994; Wagner et al., 1996; Eberl et al., 1998), and pumping by charge-exchange recombination (Koshelev et al., 1994; Koshelev and Kunze, 1997). However, the noticeable gain length product  $gl$  and, by extension, the significant X-ray laser output were achieved only by collisional excitation in a capillary discharge (Rocca et al., 1994).

#### *EUV lithography*

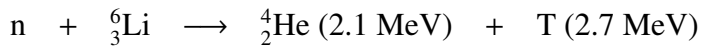
Last but not least application that will be mentioned is EUV lithography (Bailey et al., 1982; McGeoch, 1998). Several companies (such as XTREME technologies, CYMER Inc., Philips, Intel, Cutting Edge Optronics) make an effort to develop the most suitable EUV source at 13.5 nm. Gas discharge-produced plasma and laser-produced plasma belong among two prospective candidates. Both major technologies compete for high volume manufacturing and have their pros and cons (Stamm, 2004).

### 1.2.2 Controlled thermonuclear fusion

For more than 50 years, scientists have been trying to harness the fusion energy for peaceful purposes. The fusion reaction, the fundamental energy-producing process in stars, occurs when two nuclei of lighter elements are fused together to form a heavier element. Among possible reactions, the highest rate has the fusion of deuterium and tritium to helium



The free energy of 17.6 MeV is given to the  $\alpha$ -particle and the remaining neutron. This fast escaping neutron can produce tritium from lithium (the material that is intended to form the blanket surrounding a plasma)



As deuterium can be easily extracted from water and lithium can be found in the earth's crust, this kind of energy could be cheap and accessible worldwide.

Unfortunately, fusion reactions take place only when the fusing nuclei are brought close together. In order to overcome the Coulomb barrier of charged particles, the nuclei need to have the sufficient kinetic energy — the case which can happen e.g. during collisions of ions in a high temperature plasma. However, to create a plasma with very high temperature is not the only condition that we need in order to achieve fusion. It is also necessary to sustain the plasma at certain density  $n$  for sufficiently long time  $\tau$  so as a large number of fusion reactions could occur. The British physicist J. D. Lawson derived a simple criterion under which a plasma will generate  $Q$ -times more energy than is required to create and sustain it: the product of the particle density  $n$  and the confinement time  $\tau$  should be higher than a certain value, in the case of a D-T mixture

$$n\tau > Q \cdot 10^{14} \text{ cm}^{-3} \text{ s} \quad (1.1)$$

Currently, the most promising concepts seem to be magnetic confinement fusion (MCF) with a long confinement time ( $\tau \gtrsim 0.1$  s) and inertial confinement fusion (ICF) with a high density plasma ( $n \gtrsim 10^{26} \text{ cm}^{-3}$ ). The development of both concepts has passed the stage of *Proof-of-Principle*. The basic science is understood and the physics of the concept near fusion-relevant regimes is being explored (i.e. *Performance Extension*).

As far as Z-pinches are concerned, there are two substantially different ways of their application in the fusion research. The historically first way is the *direct* heating and confining of a D-T plasma via Z-pinch effect. The second approach is the use of a Z-pinch as a driver for ICF. We shall describe the latter first.

### Z-pinch as driver for ICF

Z-pinch, more precisely Sandia's Z machine, is the world's most powerful laboratory X-ray source. Such a large volume, near-Planckian X-ray source provides a well-characterised indirect driver for experiments relevant to the *Inertial Confinement Fusion* programme<sup>6</sup>. The high X-ray production efficiency ranked Z-pinch among three major drivers for *Inertial Fusion Energy* (IFE)<sup>7</sup>. Besides Z-pinches, lasers (KrF or DPSSL) and heavy ion drivers (induction linacs) are considered.

In one of the most perspective concepts, the Z-pinch radiation is produced during the collision of an imploding liner (high-Z wire-array) with an inner shell (a low density foam "convertor"). The inward travelling shock-wave generates radiation that is trapped by the outer imploding high-Z shell. Therefore, the shell acts as a hohlraum wall and becomes a high temperature blackbody radiator. Later, the generated blackbody radiation drives a spherically symmetric DT capsule in very similar way as in ICF indirectly driven by lasers. Since the shell is moving, we call it "dynamic hohlraum" or "flying radiation case" (Smirnov, 1991).

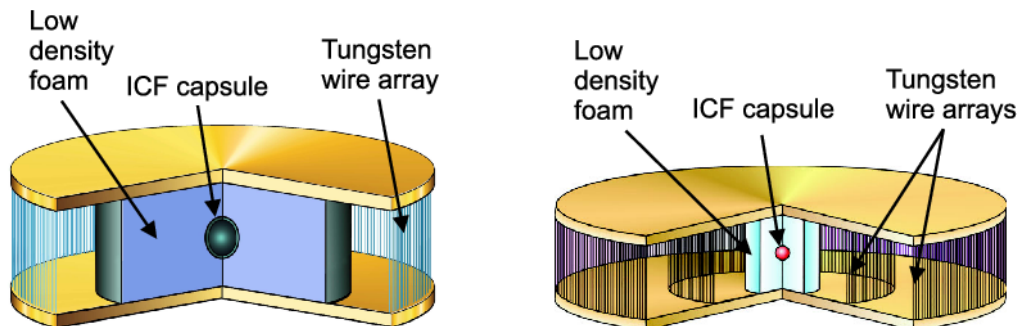


Fig. 1.2: Dynamic hohlraum.

Fig. 1.3: Dynamic hohlraum created from two nested wire-arrays.

<sup>6</sup> It is possible to study ablator physics and radiation symmetrization experiments (Matzen, 1999).

<sup>7</sup> Inertial fusion science and applications have come to be referred to as "inertial fusion energy" or IFE, whereas "inertial confinement fusion" or ICF denotes high energy density phenomena produced by either multiple high-energy laser beams or energetic pulsed power systems (Plasmas International, 2005).

Recently, dynamic hohlraum ICF experiments on  $Z$  accelerator have been created from two annular tungsten wire–arrays (a 240–wire 40–mm diameter outer array and a 120–wire 20–mm diameter inner array, see Fig. 1.3, Bailey et al., 2002b; Slutz et al., 2003a; Bailey et al., 2004; Ruiz et al., 2004). This way, a deuterium–filled capsule absorbed  $\approx 24$  kJ of X–rays from a  $\approx 220$  eV dynamic hohlraum. The thermonuclear neutron yield from the D–D reaction was up to  $8 \times 10^{10}$  which is the highest D–D neutron yield ever reached with X–ray drivers. Argon spectra confirmed a hot fuel with electron temperature and density of 1 keV and  $(1 \div 4) \times 10^{23}$  cm $^{-3}$ , respectively. The temperature of ions inferred from the neutron energy distribution was  $4.8 \pm 1.5$  keV. All these values show that the dynamic hohlraum can produce high temperature radiation and deliver a large amount of energy into the ICF capsule. However, in order to achieve higher convergence ratio, it is necessary to improve radiation symmetry control. Therefore, other complementary indirect drive concepts for high–yield IFE are being explored.

The seriously investigated concept of a double–pinch hohlraum is shown in Fig. 1.4. This concept used two dynamic hohlräums to drive a static–walled hohlraum. Experiments on  $Z$  machine demonstrated a 70 eV hohlraum temperature, 3% drive symmetry and 14  $\div$  20 convergence ratio (Cuneo et al., 2002).

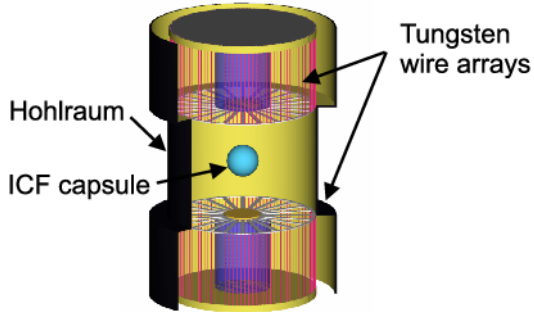


Fig. 1.4: Static hohlraum with two  $Z$ –pinch radiation sources at the ends.

The results of the past ten years were so attractive that the  $Z$ –pinch IFE Road Map and the concept of power plant were developed (Rochau et al., 2003). The design of high–yield dynamic hohlraum includes a single 12 MJ, 54 MA  $Z$ –pinch driver that produces a 350 eV radiation temperature, 2.4 MJ absorbed capsule energy and 550 MJ thermonuclear yield (Lash et al., 2000). Yet, before the high–yield 60 MA driver “ $ZX$ ” can be constructed, the 26 MA refurbished  $Z$  machine “ $ZR$ ” must first provide scaling information on a capsule (Weinbrecht et al., 2003).

The present effort is thus concentrated on demonstrating single-shot, high-yield fusion capsules. However, the rep-rated ( $\approx 0.1$  Hz) Z-pinch is needed for IFE (Slutz et al., 2003c). As a possible rep-rated pulsed power technology, linear transformer drivers (LTD) could be applied. The necessary separation between the fusion target and the power plant should be provided by a recyclable transmission line (Slutz et al., 2003b). It is planned that 1 MA driver Z-PoP (Proof-of-Principle, 1 MV voltage, 100 ns rise time, 0.1 Hz repetition) will be constructed in near future.

In spite of a rapid progress in Z-pinch driven ICF, many questions have remained to be answered. We mention at least some of them here:

- How to achieve spherically symmetric irradiation of the capsule when a Z-pinch is cylindrical by nature?
- How to control the shape and intensity of the X-ray pulse?
- How to prevent the early preheating of the capsule?
- How to mitigate gross hydrodynamic instabilities, e.g. Rayleigh–Taylor instability?

It is apparent that more experiments on these issues are still needed. Unfortunately, the number of shots on powerful devices is limited. Smaller-scale experiments are therefore used to elucidate Z-pinch physics.

Several smaller-scale experiments focus on the effect of a single wire because it helps to understand the initiation stage of wire–array Z-pinches (e.g. initial energy deposition, expansion rates, seeding of instabilities that later influence Rayleigh–Taylor instability, etc.). These experiments are pursued e.g. at Sandia National Laboratories, Albuquerque (Sarkisov et al., 2004), Imperial College, London (Lebedev et al., 2000, 2001), University of Michigan, Ann Arbor (Johnston et al., 2003), Cornell University, Ithaca (Kalantar and Hammer, 1993; Pikuz et al., 1999b,a; Sinars et al., 2000b,a; Hammer and Sinars, 2001; Duselis et al., 2004), University of Nevada, Reno (NTF, 2005).

The study of the initial stage of a discharge allowed to improve MHD capability including a “cold–start”. Recently, 3D resistive MHD simulation of wire–array Z-pinches have been developed (Eulerian code “Gorgon”, Chittenden et al., 2004, and Arbitrary–Lagrangian–Eulerian code ALEGRA–HEDP, Garasi et al., 2004).

*Direct heating and confining of a fusion plasma via Z–pinch effect*

The other mentioned approach of the Z–pinch use in the fusion research is the direct heating and confining of a fusion plasma via pinch effect. The accomplishment of this goal has been somewhat problematic from the beginning of Z–pinch research (see subsection 1.1). There were serious doubts about issues of crucial importance, such as how to suppress magnetohydrodynamic instabilities and the interaction of the plasma with a wall? Since the early attempts, a large number of ideas have been proposed to overcome these difficulties:

- A *quasiequilibrium Z–pinch* with direct heating of a DT mixture (e.g. cryogenic DT fibre, see subsection 1.3).
- *Staged pinch*. In this case, the azimuthal magnetic field (generated by the current flowing in a DT fibre) is compressed by an imploding liner. When the imploding liner approaches the fibre, the inductance of the fibre decreases, the current in the fibre rapidly increases, and the fibre is heated and compressed (Rahman et al., 1995).
- *Z–pinch stabilised by a strong axial flow*. What happens here is that a plasma is accelerated between two coaxial electrodes and after that the Z–pinch effect occurs. This concept is very similar to a plasma focus.
- *Adiabatic compression* and heating of a DT plasma during cylindrically or spherically symmetric implosion of a liner (Degnan, 1995).
- *Magnetised Target Fusion*. This concept is based on adiabatic compression of a *magnetised* plasma. In comparison with the previous concept, the heat losses from the fusion plasma to walls are suppressed by weak magnetic field with  $\beta \gtrsim 1$ . As examples of the MTF concept we can mention (i) the compression of field reverse configuration (Ryutov and Siemon, 2001) and (ii) the MAGO<sup>8</sup> project of Los Alamos National Laboratory and All–Russian Scientific Research Institute of Experimental Physics (Lindemuth et al., 1995).
- *High yield systems*. They are characterised by the propagating of a nuclear burn wave that is ignited in some part of a cylindrical column, e.g. in the neck of an  $m = 0$  instability (Linhart, 1994; Chittenden et al., 2005).

---

<sup>8</sup> MAGnitnoye Obzhatiye = Magnetised Target Fusion.

All these concepts have not been explored to such an extent as ICF and MFC were. Thus one may ask what the motive for such alternative approaches is.

One of the main reasons is that the region between conventional magnetic fusion ( $n_e \lesssim 10^{14} \text{ cm}^{-3}$ ) and inertial fusion ( $n_e \gtrsim 10^{26} \text{ cm}^{-3}$ ) offers vast possibilities for smaller and cheaper fusion experiments (Siemon et al., 1999). We often speak about *Magneto–Inertial Fusion* that represents the all–inclusive set of inertially confined approaches to fusion that involve magnetic field in an essential way. Magnetic field is then used to suppress the heat flow from the inertially confined plasma and therefore requirements on fusion drivers could be reduced.

### 1.2.3 Other applications

Except the above mentioned applications of a Z-pinch, there are yet other possibilities of using this device. The following list briefly summarises few of them:

- Lab-astrophysics (Ryutov and Remington, 2002). The generation of highly supersonic plasma jets with MACH number of 50 can serve as an example (Lebedev et al., 2002).
- Controlled generation of high magnetic fields ( $\approx 1000$  T) by magnetic field compression in an imploding cylindrical shell (Felber et al., 1985).
- Generation of charged and neutral particles for industrial, scientific and medical applications.
- Optical guidance of terrawatt laser pulses in a capillary discharge (Hosokai et al., 2000).
- Spectroscopy of highly charged ions (Pereira and Davis, 1988).

### 1.3 Fibre Z–pinch

#### 1.3.1 Cryogenic deuterium fibres

The high density Z–pinches formed from dielectric fibres were investigated in the 1980s and 1990s in connection with the research of controlled thermonuclear fusion and radiative collapse (see subsection 2.1.2). The notion was to heat and ionise the fibre from frozen deuterium and to confine the high density and high temperature plasma column within a small diameter.

The first experiments were performed at Naval Research Laboratory (Sethian et al., 1987) and Los Alamos National Laboratory (Scudder, 1985; Hammel and Scudder, 1987). Z–pinch plasma in these experiments seemed to be stable for many radial Alfvén transit times (cf. Eq. 2.27 on page 31), whereas the neutron yield approached  $10^{10}$ . This promising result led to the modification of the Z–pinch theory when the arbitrary current distribution (Coppins, 1989), resistivity (Cochran and Robson, 1990b; Culverwell and Coppins, 1990), viscosity (Cochran and Robson, 1990a), the Hall term and electron pressure gradient in Ohm’s law (Coppins et al., 1984), pressure anisotropy (Coppins and Scheffel, 1992), etc. were included in fluid models. Further, finite ion Larmor radius effects were calculated via Vlasov–fluid model (Scheffel et al., 1997). Nevertheless, none of these improvements could explain the experimentally observed stability (see a nice review of the Z–pinch stability written by Coppins, 1997). With the use of a “cold–start” MHD simulation, Lindemuth et al. (1989) calculated that the enhanced stability was due to the presence of the solid core of a fibre which lasted for a very long time. The subsequent calculation showed that rather than enhancing the stability, the core partially masked the evidence of instabilities (Lindemuth, 1990; Sheehey et al., 1992). Similarly discouraging results were obtained from further and better diagnosed experiments on new generators at NRL (Sethian et al., 1990b) and Los Alamos (Scudder et al., 1990) as well as on KALIF at Kernforschungszentrum Karlsruhe (Kies et al., 1991) and on MAGPIE at Imperial College in London (Lebedev et al., 1998).

#### 1.3.2 Carbon and deuterated polyethylene fibres

The fibres from carbon and deuterated polymer were also employed in the Z–pinch experiments because their discharge behaviour was roughly the same as the frozen deuterium ones (Lebedev et al., 1998; Riley et al., 1996); at the same time they were easily avail-

able and could be handled much easier. The main difference is an atomic number ( $Z = 1$  for hydrogen or deuterium, and  $Z = 6$  for carbon). Furthermore, carbon or deuterated polymer fibres radiate more than pure deuterium fibres. The carbon and polymer fibres also require more energy for producing fully stripped ions.

Stephanakis et al. (1972) pursued the first experiments with deuterated polymer fibre on the Gamble II facility in the 1970s. The number of detected neutrons exceeded the value of  $10^{10}$ . From that time on, several tens of experiments with carbon and deuterated polymer fibres were performed but the neutron yield has never been higher. The list of most important experiments is displayed in Tab. 1.4, 1.5 and 1.6<sup>9</sup>. The results of these experiments – those that are relevant to our work – are given in the discussion part in chapter 5.

### 1.3.3 Contemporary state of art

To our knowledge, the last experiments with deuterium fibres were performed in the late 1990s and the idea of nuclear fusion and radiative collapse in fibre Z–pinches was abandoned. During that period of time, the theory and MHD modelling were improved to such a degree that it was possible to explain gross dynamics of the discharge as well as a few “fine” phenomena (e.g. Chittenden et al., 1997) of fibre Z–pinches. However, several key–points (such as the mechanism of neutron production, the generation of electron and ion beams, etc.) remained still unresolved.

### 1.3.4 Fibre Z–pinch drivers

All the above cited experiments utilised high–voltage pulsed–power systems instead of a simple capacitor bank. According to Mitchell et al. (1996), there were two principal reasons:

- High voltage transients caused by changes of plasma inductance and resistance could damage low impedance and low voltage capacitors.
- The current rise must be fast enough to prevent the early expansion of a plasma column.

---

<sup>9</sup> The list does not include experiments with glass and polyamide fibres because only fragmentary results were published. The only exception is Figura’s experiment on the IMP generator at Imperial College in London (Figura et al., 1991).

### *1.3.5 Our experiment*

Our research is based on the results from a carbon fibre Z–pinch driven by a slow (microsecond–long) capacitive discharge. The purpose of this small scale experiment is a detailed description of fibre Z–pinch dynamics<sup>10</sup>. On one hand, the use of a capacitor as a current generator has the aforementioned disadvantages, but on the other hand, it could provide new experimental results which can be compared with those obtained at more powerful devices. We hope that this comparison will enable us better understanding of general characteristics of fibre Z–pinches. Also, we would like to take the advantage of a small–scale experiment which could be easily modified and, in some cases, better diagnosed, while it remains interesting from the physical point of view.

---

<sup>10</sup> Our experiment also serves for preparing diagnostics which is used on more powerful current generators (e.g. S–300 generator at Kurchatov Institute in Moscow and plasma focus PF–1000 at IPPLM institute in Warsaw.).

Name	Location	Current [kA]	Rise time [ns]	Energy [kJ]	Voltage [kV]	Fibre	Diameter [μm]	Length [cm]	Neutrons	Ref./Note
Gamble II	NRL, USA	1200	50	600	CH, CD	10 ÷ 190			$10^{10}$	Stephanakis et al. (1972)
Gamble II	NRL, USA	700	50	50	1000	CH, CD	8 ÷ 150		$10^{10}$	Young et al. (1977)
Poseidon	NRL, USA	640	130	500	D	60 ÷ 125	5		$8 \times 10^9$	Sethian et al. (1987)
ZFX	NRL, USA	450	640	60	210	D	125	5	$4 \times 10^8$	Sethian et al. (1989)
ZFX	NRL, USA	1000	670			D	125		$2 \times 10^9$	Sethian et al. (1990a)
ZFX	NRL, USA	920	840			CD	40			
ZFX	NRL, USA					C	7			
ZFX	NRL, USA					D	125			Sethian et al. (1990b)
HDZP-I	LANL, USA	350	150	12	600	D	40	5	$10^7 \div 10^8$	Scudder (1985)
HDZP-II	LANL, USA	650	100	100	D	20			$3 \times 10^9$	Shlachter (1990)
Zebra						D				
HDZP-II	LANL, USA	800							$5 \times 10^9$	Scudder et al. (1990)
Zebra										
HDZP-II	LANL, USA	700	100	210	3200	CD	15 ÷ 150	5		Scudder et al. (1994)
Zebra										
HDZP-II	LANL, USA	800	100	100	2200	CD	3 ÷ 60	5	$2 \times 10^9$	Riley et al. (1996)
Zebra										

Tab. 1.4: Electrical characteristics of carbon, polymer, and deuterium fibre Z–pinches I.

Name	Location	Current [kA]	Rise time [ns]	Energy [kJ]	Voltage [kV]	Fibre	Diameter [µm]	Length [cm]	Neutrons	Ref./Note
IMP	Imperial College London, GB	100	55	5	400	C	7, 33	2		Beg et al. (1997)
IMP	Imperial College London, GB	160	80	11	600	C	360	1.4		Davies et al. (1997)
IMP	Imperial College London, GB	200	60	20	800	C	7	2		Lorenz et al. (1998, 1999)
MAGPIE	Imperial College London, GB	1400	150	200	1900	CD	50 ÷ 200	2.5	$10^9$	Mitchell et al. (1998)
MAGPIE	Imperial College London, GB	1000	150	120	1400	C	7, 33	2.5		Aliaga-Rosset et al. (1998)
MAGPIE	Imperial College London, GB	1000	200			D	100	2.3	$5 \times 10^9$	Haines (1997)
Kalif	KFZ, Karlsruhe Germany	800	60		2000	D	25 ÷ 50	3 ÷ 5	$10^{10}$	Lebedev et al. (1998)
Kalif	KFZ, Karlsruhe Germany	1000	90		2000	C, CD hair	7 ÷ 300	3 ÷ 6	$10^{10}$	Decker and Kies (1989)
Kalif	KFZ, Karlsruhe Germany	1000	90			C	7			Kies et al. (1991)

Tab. 1.5: Electrical characteristics of carbon, polymer, and deuterium fibre Z–pinches II.

Name	Location	Current [kA]	Rise time [ns]	Energy [kJ]	Voltage [kV]	Fibre	Diameter [μm]	Length [cm]	Neutrons	Ref./Note
SPEED 2	Duesseldorf Univ. Germany	3000	400		300	CD, D			$10^9$	Decker and Kies (1989)
S-300	Kurchatov Inst. Moscow, Russia	2000	190			CD	100	1	$10^8 \div 10^9$	see Appendix C
LIMAY-I	Nagoya Univ. Japan	150	100	5	1000	C	7	2		Ishii et al. (1989)
LIMAY-I	Nagoya Univ. Japan	300	80	5	1000	C	7	2		Ishii et al. (1993)
	Inst. of Techn. Tokyo, Japan	1	100		30	C	7	2		Ishii et al. (1989) atmosph., water, vacuum
	Bochum Univ. Germany	30	1500	1	20	C	270	2.5		Haun (2001)
Z-150	CTU, Prague Czech Republic	100	800	1	$20 \div 30$	C	6, 15 80	1		Klír et al. (2004b) Klír (2002)

Tab. 1.6: Electrical characteristics of carbon, polymer, and deuterium fibre Z–pinches III.

## Chapter 2

### THEORETICAL BACKGROUND

This chapter provides theoretical background upon which the thesis is based. Because the dominant physical processes of equilibrium and dynamic pinches are substantially different, it might raise a question of what kind of pinch we are actually describing here. The title clearly suggests that our work is devoted mainly to a fibre Z–pinch. One can therefore expect an equilibrium pinch. However, as it will be shown later, many phenomena of dynamic pinches were also observed in our experiments. That's why this theoretical background comprises both equilibrium pinches and dynamic pinches.

#### 2.1 Equilibrium Z–pinches

##### 2.1.1 Bennett equilibrium (Liberman et al., 1999)

Steady–state equilibrium of a Z–pinch can be derived from Maxwell's equations and the ideal magnetohydrodynamic equations in which we set the velocity and all time derivatives to zero. We obtain so–called magnetostatic equations for perfectly conducting plasma

$$\nabla p - \vec{j} \times \vec{B} = 0 \quad (2.1)$$

$$\nabla \times \vec{B} = \mu \vec{j} \quad (2.2)$$

$$\nabla \cdot \vec{B} = 0 \quad (2.3)$$

By excluding the current density  $\vec{j}$  from equations 2.1 and 2.2, we get

$$\nabla p + \nabla \frac{\vec{B}^2}{2\mu} - \frac{1}{\mu} (\vec{B} \nabla) \vec{B} = 0 \quad (2.4)$$

In cylindrical geometry, we can rewrite it as follows:

$$\begin{aligned}
 (\vec{B}\nabla)\vec{B} &= \vec{r}^0(B_r \frac{\partial B_r}{\partial r} + \frac{B_\theta}{r} \frac{\partial B_r}{\partial \theta} + B_z \frac{\partial B_r}{\partial z} - \frac{1}{r} B_\theta B_\theta) \\
 &+ \vec{\theta}^0(B_r \frac{\partial B_\theta}{\partial r} + \frac{B_\theta}{r} \frac{\partial B_\theta}{\partial \theta} + B_z \frac{\partial B_\theta}{\partial z} + \frac{1}{r} B_\theta B_r) \\
 &+ \vec{z}^0(B_r \frac{\partial B_z}{\partial r} + \frac{B_\theta}{r} \frac{\partial B_z}{\partial \theta} + B_z \frac{\partial B_z}{\partial z})
 \end{aligned} \tag{2.5}$$

The Z–pinch is a cylindrically symmetric plasma column and therefore all quantities are function only of the radial coordinate  $r$ , i.e.  $\partial/\partial z = 0$  and  $\partial/\partial\theta = 0$ . Thus, the basic radial pressure balance relation for a Z–pinch is

$$\frac{\partial}{\partial r} \left( p + \frac{B^2}{2\mu} - \frac{B_r^2}{2\mu} \right) + \frac{1}{\mu} \frac{B_\theta^2}{r} = 0 \tag{2.6}$$

$$\frac{\partial}{\partial r} \left( p + \frac{B_\theta^2}{2\mu} + \frac{B_z^2}{2\mu} \right) + \frac{1}{\mu} \frac{B_\theta^2}{r} = 0 \tag{2.7}$$

Next, we assume the current flowing along the  $z$  axis. Since we do not consider external magnetic field  $B_z$ , Amper's law 2.2 gives only one non–zero component of magnetic field, namely azimuthal one  $B_\theta$ . Then equation 2.7 reduces to

$$\frac{\partial}{\partial r} \left( p + \frac{B_\theta^2}{2\mu} \right) + \frac{1}{\mu} \frac{B_\theta^2}{r} = 0 \tag{2.8}$$

$$\frac{\partial p}{\partial r} + \frac{1}{2\mu r^2} \frac{\partial}{\partial r} (B_\theta^2 r^2) = 0 \tag{2.9}$$

The first term in equation 2.8 represents the gradient of the magnetic and kinetic pressure. The second term is the tension force generated by the curvature of the azimuthal magnetic field. This “curvature force” acts towards field's line centre of curvature. Since we have only one equation 2.9 for two independent functions  $p(r)$  and  $B_\theta(r)$ , one of them can be taken arbitrary. From experimentalist's point of view, it is convenient to choose arbitrarily the magnetic field  $B_\theta(r)$  and hence the current  $I(r)$ . If we introduce Amper's law

$$B_\theta(r) = \frac{\mu I(r)}{2\pi r} \tag{2.10}$$

into equation 2.9, we find that

$$\frac{\partial p}{\partial r} + \frac{\mu}{8\pi^2 r^2} \frac{\partial I^2(r)}{\partial r} = 0 \tag{2.11}$$

By integrating this equation *per partes* and using the boundary condition at the pinch radius  $p(R) = 0$ , we obtain

$$\mu I_0^2 = 16\pi^2 \int_0^R rp(r)dr \quad (2.12)$$

At this point, it is appropriate to define the ion line density as

$$N_i = 2\pi \int_0^R n_i(r)rdr \quad (2.13)$$

and the Bennett temperature<sup>1</sup>, as

$$T_B = \frac{2\pi}{kN_i(1 + \bar{z})} \int_0^R p(r)rdr \quad (2.14)$$

Substituting  $N_i$  and  $T_B$  in 2.12, we easily find the well-known Bennett condition in the following form

$$\frac{\mu I_0^2}{8\pi} = kT_B N_i(1 + \bar{z}) \quad (2.15)$$

This equation represents an integral equilibrium valid for any profiles of  $p(r)$  and  $I(r)$ . For practical use, the Bennett relation can be rewritten as

$$T_B \doteq 3.12 \frac{I_0^2}{(1 + \bar{z})N_i} \quad [\text{keV; MA, } 10^{18} \text{ cm}^{-1}] \quad (2.16)$$

It follows that the lower line density  $N_i$  is, the higher plasma temperature  $T_B$  can be achieved. However, if the line density  $N_i$  is too low, microinstabilities driven by the current can be triggered (see paragraph 2.1.3).

### 2.1.2 Pease–Braginskii current and radiative collapse

The balance between the kinetic and magnetic pressure is not the only condition that is necessary for a steady-state equilibrium. The Z–pinch in radial equilibrium should satisfy also the energy balance. If we neglect axial heat losses absorbed by the electrodes,

---

<sup>1</sup> It is the weighted temperature. The weighting goes over plasma density

$$T_B = \frac{2\pi}{kN_i(1 + \bar{z})} \int_0^R p(r)rdr = \frac{1}{k(1 + \bar{z})} \frac{\int_0^R p(r)rdr}{\int_0^R n_i(r)rdr} = \frac{\int_0^R [T_i(r)n_i(r) + T_e(r)n_e(r)]rdr}{\int_0^R (1 + \bar{z})n_i(r)rdr}$$

For an isothermal plasma, where  $T_e = T_i$ , the weighted temperature equals the average temperature  $T_B = \bar{T}_e = \bar{T}_i$ .

the condition of the balance between ohmic heating  $P_J$  and radiative cooling  $P_R$  must be fulfilled. To evaluate radiated power and Joule heating power, we will consider optically thin plasma, uniform temperature, uniform current density, and bremsstrahlung radiation only

$$P_R = P_{BS} = A\bar{z}^3(kT_e)^{1/2}I \int_0^R \int_0^{2\pi} n_i^2(r)rd\theta dr \quad (2.17)$$

$$P_J = \frac{1}{G}I_0^2 = \frac{l\bar{z}\ln\Lambda}{\pi R^2\sigma_0(kT_e)^{3/2}}I_0^2 \quad (2.18)$$

By using equation 2.15 and a parabolic density profile  $n_i(r) = n_{\max}(1 - r^2/R^2)$ , we obtain

$$\frac{P_J}{P_{BS}} = \frac{I_{PB}^2}{I_0^2} \quad (2.19)$$

where

$$I_{PB} = \frac{\pi}{\mu} \sqrt{\frac{48\ln\Lambda}{\sigma_0 A}} \frac{1 + \bar{z}}{\bar{z}} \quad (2.20)$$

is known as the Pease–Braginskii current. Its value for a deuterium plasma<sup>2</sup> is  $I_{PB} \approx 1.4$  MA.

The pinch radius does not change only if the current is equal to the Pease–Braginskii one. At currents above this value, radiation losses exceed Joule heating, which results, according to the first law of thermodynamics, in the negative value of the external work  $p dV$ . Hence, the pinch radius decreases. In other words, the pinch undergoes a spontaneous contraction and the radiative collapse occurs. The collapse will continue until the opacity and degeneracy of electron gas begin to play their role.

In this connection it is important to note that the value of the Pease–Braginskii current could be substantially changed by anomalous resistivity, leakage currents, axial magnetic field, resonant line and recombination radiation, opacity, axial and radial heat losses, particle losses, etc. From the experimental point of view, we could mention the influence of the decreasing pinch radius and increasing plasma inductance which can lead to the drop of the electric current delivered from an external generator. However, what we would like to point out is that whatever the critical current is, the energy balance determines whether the pinch expands or collapses.

<sup>2</sup> Coulomb logarithm equals  $\ln\Lambda \approx 10$ .

### 2.1.3 Ideal MHD stability of equilibrium Z–pinch

The stability of Z–pinches is a primary object of interest because the plasma has to be stable for a sufficiently long confinement time in order to burn thermonuclear reactions. During the early stage of fusion research it was shown that linear Z–pinches are highly MHD unstable. During the last decades, linear and non–linear analysis of magnetohydrodynamic and kinetic instabilities was undertaken and stability criteria were deduced. With reference to this thesis, we will restrict ourselves to basic definitions and results of linear theory.

#### Linear perturbation theory

As far as the linear perturbation theory is concerned, the starting point is a set of linearised MHD equations. We assume the plasma to be in the steady–state equilibrium. After that we perturb slightly this equilibrium. We take the advantage of linear theory and use the Fourier analysis to express the Lagrangian displacement

$$\vec{\xi}(\vec{r}, t) = \vec{\xi}_0(\vec{r}) e^{i(m\theta+kz)+\Gamma t} \quad (2.21)$$

where  $\text{Re}(\Gamma)$  is the growth rate,  $m$  and  $k$  are azimuthal and axial wave numbers.

The nomenclature of instabilities could be derived from the previous equation 2.21: MHD instabilities are often classified according to the azimuthal wave number  $m$ . The sausage (axisymmetric) instability corresponds to  $m = 0$ , whereas the kink (helical) instability to  $m = 1$ .

Since all perturbed quantities are expressed in terms of displacement vector  $\vec{\xi}(\vec{r}, t)$ , the set of differential MHD equations can be converted to algebraical ones (with respect to time). Consequently, the solution of algebraical equations could provide eigenvalues  $\Gamma$  and thus the answer about stability. If  $\text{Re}(\Gamma)$  is negative, we speak about the exponentially stable system. Unfortunately, in the case of the Bennett equilibrium and the ideal MHD model, the growth rate of an  $m = 0$  instability is positive of the order of

$$\text{Re}(\Gamma) \sim \frac{v_A}{R} \quad (2.22)$$

where  $R$  is the pinch radius and  $v_A$  is the Alfvén velocity

$$v_A \approx \frac{B_{\max}}{\sqrt{\mu\bar{\rho}}} \quad (2.23)$$

Substituting

$$B_{\max} = \frac{\mu I_0}{2\pi R} \quad (2.24)$$

$$\bar{\rho} = \frac{N_i M_i}{\pi R^2} \quad (2.25)$$

into equation 2.23, we obtain the Alfvén velocity

$$v_A \approx \sqrt{\frac{\mu I_0^2}{4\pi N_i M_i}} \quad (2.26)$$

To compare theoretical predictions with experimental observations, it is convenient to define the number of *ideal MHD times* that have elapsed when instability first appeared at time  $\tau$

$$\int_0^\tau \Gamma(t) dt = \int_0^\tau \frac{v_A(t)}{R(t)} dt = \sqrt{\frac{\mu}{4\pi^2}} \int_0^\tau \frac{I_0(t)}{\sqrt{\bar{\rho}(t)} R^2(t)} dt \quad (2.27)$$

#### *Physical mechanisms of the sausage and kink instabilities*

A simple physical interpretation of the sausage and kink instability is illustrated in Fig. 2.1 and 2.2. If we imagine a plasma column in MHD equilibrium and with the axisymmetric perturbation (cf. Fig. 2.1, Horák and Krupka, 1981) then the toroidal loops of magnetic field will be shrunk in the neck. The magnetic field in the neck increases and cannot be balanced by the kinetic pressure. The rise of the Lorentz force  $\vec{j} \times \vec{B}$  causes the growth of a perturbation. The characteristic velocity of the perturbation growth is that of a fast magnetosonic wave  $v_A$ .

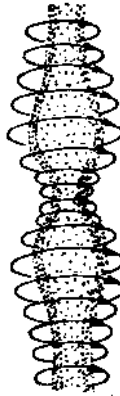


Fig. 2.1: Sausage instability,  $m = 0$ .



Fig. 2.2: Kink instability,  $m = 1$ .

The bending of a plasma column (cf. Fig. 2.2) demonstrates the same effect. The field strength is intensified along the inner face of the bend and reduced along the outer face. Thereby the instability will be amplified.

### Stability criteria

The necessary and sufficient condition for the  $m = 0$  and  $m \geq 1$  stability of Z–pinch was given by Kadomtsev (1963). He showed that the Z–pinch is stable against  $m = 0$  instabilities if the pressure profile fulfils the following inequality for all  $r$

$$-\frac{d \ln p(r)}{d \ln r} = -\frac{r}{p(r)} \frac{dp(r)}{dr} < \frac{4\gamma}{2 + \gamma\beta(r)} \quad (2.28)$$

where  $\gamma = c_p/c_V$  is the ratio of specific heats and  $\beta(r) = 2\mu p(r)/B_\theta^2(r)$  is the ratio of the kinetic and magnetic pressure. Since the pressure of a fibre pinch<sup>3</sup> falls to zero at the vacuum–plasma boundary, the pinch is always  $m = 0$  unstable.

As far as  $m \geq 1$  modes are concerned, the current density profile has to satisfy the condition (Liberman et al., 1999)

$$\frac{r^2}{B_\theta} \frac{d}{dr} \left( \frac{B_\theta}{r} \right) < \frac{1}{2}(m^2 - 4) \quad (2.29)$$

The analysis of this expression shows that every Z–pinch with the finite (non–singular) current density at the axis is  $m = 1$  unstable.

### Applicability of ideal MHD and non-ideal regimes of Z–pinches

The ideal MHD stability theory predicts the growth of instabilities on the Alfvén time scale. However, ideal MHD neglects resistivity, viscosity, thermal conduction, the finite ion Larmor radius, and other phenomena which may modify the instability growth time. In order to be valid, ideal MHD requires that the plasma fulfils the following conditions:

- First, the plasma must have a low resistivity which is usually quantified by the Lundquist number  $S = \mu\sigma v_A R$  (the ratio between the Lorentz force and resistive magnetic diffusion force). Culverwell and Coppins (1990) found the critical Lundquist number  $S^*$  below which the enhanced stability is predicted. This critical Lundquist number depends on  $kR$  ( $k$  is the axial wave number and  $R$  is the

<sup>3</sup> In the case of gas–embedded Z–pinches, the Kadomtsev’s criterion can be satisfied.

pinch radius) and, typically, one can take this number of  $10 \div 100$  (cf. Coppins and Culverwell, 1997).

- Second, the plasma must be highly collisional. In other words, the ion–ion collision time should be lower than the characteristic MHD time, i.e.  $\Gamma\tau_i < 1$ .
- Third, the ion Larmor radius must be small in comparison to the pinch radius, i.e.  $\rho_i/R \ll 1$ . Otherwise it is necessary to describe a collisional plasma by the Hall fluid model where the Hall term and the electron pressure gradient are included in Ohm’s law. When a plasma is collisionless, the Vlasov fluid model is more appropriate. In the regime where the ion Larmor radius is large  $\rho_i/R > 0.1$  and ions are magnetised  $\omega_{ci}\tau_i > 1$ , there is some theoretical and experimental evidence of reduction of instability growth rates.

Assuming the pinch in the Bennett equilibrium, these three dimensionless parameters ( $S$ ,  $\Gamma\tau_i$ ,  $\rho_i/R$ ) are functions of only two parameters, namely the ion line density  $N_i$  and the product of fourth power of the current and the pinch radius  $I^4R$ . If we plot  $I^4R$  against  $N_i$ , we obtain the diagram of the stability regimes (Haines and Coppins, 1991). In this diagram, the ideal MHD region occupies a fairly small space of the experimentally relevant regions.

### *Microinstabilities and turbulences*

Microinstabilities<sup>4</sup> are excited in a plasma when the drift velocity of electrons  $v_{De} = j_z/en_e$  exceeds the critical velocity which is typically of the order of the ion sound speed  $c_s = \sqrt{k(T_i + \bar{z}T_e)/M_i}$ . As a result, turbulences of electrostatic and electromagnetic field cause drifting electrons to be scattered. Since electrons are now scattered both from individual ions and from turbulent electromagnetic field, the anomalous contribution to resistivity has to be considered. This anomalous resistivity can occur not only in the neck of an  $m = 0$  instability, but also in a low density plasma boundary. In this region, the drift velocity  $v_{De}$  can grow to a higher value because the electron density approaches zero  $n_e \rightarrow 0$  and the current density  $j_z$  is finite.

---

<sup>4</sup> Lower hybrid and ion acoustic instabilities are usually most relevant in high–density Z–pinches (Rytov et al., 2000).

## 2.2 Dynamic Z–pinches

Most of the Z–pinches, including our fibre Z–pinch, are in radial equilibrium for a very short period, if at all. Therefore, the fully consistent approach requires to consider Z–pinch dynamics. The fluid dynamics can be described by the Euler equation of motion

$$\rho \frac{d^2 \vec{r}}{dt^2} = \vec{f}_p + \vec{f}_m = -\nabla p + \vec{j} \times \vec{B} \quad (2.30)$$

where the pressure gradient  $\vec{f}_p = -\nabla p$  and the magnetic force density  $\vec{f}_m = \vec{j} \times \vec{B}$  are included, whereas the momentum<sup>5</sup> of accreting material  $-\rho \vec{r}^2$ , viscous force  $\eta \Delta \vec{v}$  and other terms are neglected. To express the radial component of the previous equation, we can use the same derivation as we did for equation 2.11

$$\rho(r) \frac{d^2 r}{dt^2} = -\frac{\partial p(r)}{\partial r} - \frac{\mu}{8\pi^2 r^2} \frac{\partial I^2(r)}{\partial r} \quad (2.31)$$

### 2.2.1 Magnetic compression

One of the usual cases of a non–equilibrium state is the magnetic compression when the pressure gradient is small compared with the Lorentz force. It means

$$\rho(r) \frac{d^2 r}{dt^2} = -\frac{\mu}{8\pi^2 r^2} \frac{\partial I^2(r)}{\partial r} \quad (2.32)$$

Next, we assume the uniform current density and constant current<sup>6</sup>

$$I(r(t)) = I_0 \frac{r(t)^2}{R(t)^2} \quad (2.33)$$

and therefore

$$\rho(r) \frac{d^2 r(t)}{dt^2} = -\frac{\mu I_0^2 r(t)}{2\pi^2 R^4(t)} \quad (2.34)$$

It is evident that one has to know the density profile in order to solve this equation. To simplify the problem and to find an approximative solution, we can replace some quantities in Eq. 2.34

$$\rho(r) \longrightarrow \bar{\rho} \quad (2.35)$$

<sup>5</sup> This term cannot be neglected in the case of snowplough implosion where the mass is swept up by the collapsing shell.

<sup>6</sup> The implosion time is often much shorter than the current pulse width.

$$r \longrightarrow R(t) \quad (2.36)$$

Then we get

$$\bar{\rho} \frac{d^2 R(t)}{dt^2} \approx -\frac{\mu I_0^2}{2\pi^2 R^3(t)} \quad (2.37)$$

By using equation 2.25 and 2.26, we can derive the equation

$$R \frac{d^2 R}{dt^2} \approx -\frac{\mu I_0^2}{2\pi N_i M_i} = -2v_A^2 \quad (2.38)$$

This equation can be easily integrated by multiplication with the velocity  $dR(t)/dt$ , and by using the initial conditions  $R|_{t=0} = R_0$  and  $\dot{R}|_{t=0} = 0$

$$R \dot{R} \ddot{R} \approx -2v_A^2 \dot{R} \quad (2.39)$$

$$\frac{1}{2} \frac{d}{dt} \left( \frac{dR(t)}{dt} \right)^2 \approx -2v_A^2 \frac{d}{dt} \ln R(t) \quad (2.40)$$

$$\left( \frac{dR(t)}{dt} \right)^2 \approx 4v_A^2 \ln \frac{R_0}{R(t)} \quad (2.41)$$

$$\left| \frac{dR(t)}{dt} \right| \approx 2v_A \sqrt{\ln \frac{R_0}{R(t)}} \quad (2.42)$$

It follows that the implosion velocity is increasing with the decreasing pinch radius  $R(t)$ . Because the dependence is logarithmic and in addition to that in the square root, the implosion velocity  $v_{\text{imp}}$  is of the order of the Alfvén velocity

$$v_{\text{imp}} \approx 2v_A = \sqrt{\frac{\mu I_0^2}{\pi N_i M_i}} \quad (2.43)$$

### 2.2.2 Stability of dynamic pinches

The dynamic and equilibrium pinches differ in the extent to which instabilities matter in each case. The important difference arises from the fact that implosion/explosion takes a finite time, whereas a steady-state plasma is supposed to last for ever. For instance, instabilities with growth rates  $\Gamma \ll v_A/R$  are much more important in equilibrium pinches than in dynamic ones (Ryutov et al., 2000). Regarding the Rayleigh–Taylor instability, it plays a crucial role in all dynamic pinches, whereas in equilibrium pinches it does not develop.

### Rayleigh–Taylor instability

The RT instability is universal and occurs in all accelerating/decelerating systems where a high density fluid is “supported” by a lower density one. The growth rate of perturbations for a liquid supported by gravity is (Liberman et al., 1999)

$$\Gamma = \sqrt{gk} \quad (2.44)$$

where  $k = 2\pi/\lambda$  is the wave number of instability and  $g$  is the (gravitational) acceleration. In dynamic pinches, the gravity is represented by the magnetic field during the implosion and by the kinetic pressure during the explosion. It follows from equation 2.44 that the growth rate  $\Gamma$  is unlimited with increasing wave numbers  $k$ . However, for high wave numbers the dissipative effects (such as finite viscosity, thermal conductivity and resistivity) have to be considered. As a result, the maximum growth rate is finite.

Finally, we would like to mention the stabilising effect of the snowplough implosion. Although the mass accretion during the implosion could be destabilising, the reduction of the acceleration and the effect of the foregoing shock wave finally lead to the effective mitigation of RT instabilities.

## Chapter 3

### APPARATUS AND DIAGNOSTICS

This chapter deals with the experimental set-up of a Z-150 Z-pinch<sup>1</sup> (see Fig. 3.1), which is located at the Czech Technical University in Prague, Faculty of Electrical Engineering. This small device was employed for our fibre Z-pinch experiments, the results of which are presented in this thesis. During the past four years, we carried out more than 500 shots in a few series under different experimental conditions. The following sections describe the current generator, experimental chamber, Z-pinch load, and diagnostics. First of all, however, we introduce the block diagram and electrical scheme of the Z-150.

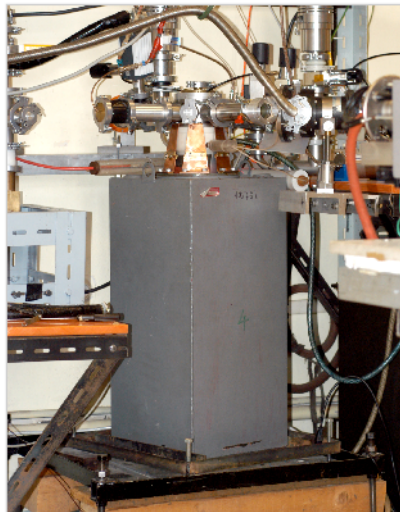


Fig. 3.1: Z-pinch device Z-150, Czech Technical University in Prague.

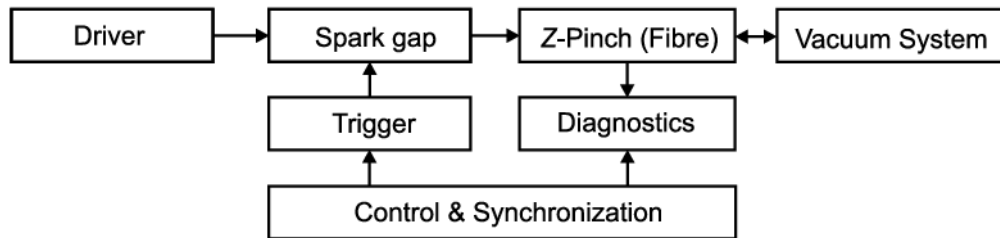
#### 3.1 Z-pinch Device Z-150

The block diagram in Fig. 3.2 shows that the Z-150 device can be divided into the sub-systems presented in Tab. 3.1. The electric scheme of the Z-150 is displayed in Fig. 3.3.

---

<sup>1</sup> The name Z-150 was derived from the expected current of 150 kA when 30 kV voltage is applied.

Driver	capacitor, high voltage transformer, rectifier, control unit
Spark gap	operates in nitrogen
Trigger	thyatron based, voltage $2 \times 15$ kV
Fibre Z-pinch	experimental chamber, electrode system, diagnostic ports
Vacuum system	rotary pump, turbo pumps, pressure gauges, valves
Diagnostics	Rogowski coil, voltage monitor, filtered PIN diodes, scintillator-photomultiplier hard X-ray detector, XUV spectrometer, X-ray and VUV pinhole cameras, laser diagnostics, digital storage oscilloscopes
Control & synchronization	master pulse generator, delay units

Tab. 3.1: Sub-systems of the *Z*-150 device.Fig. 3.2: Block diagram of the *Z*-150 device.

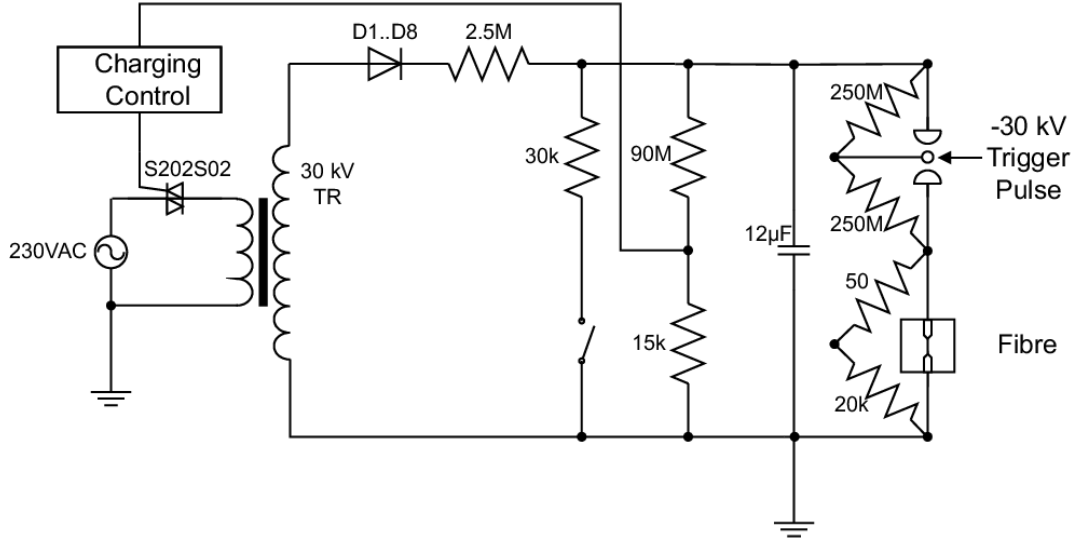


Fig. 3.3: Electric scheme of the Z-150 device.

### 3.2 Current Generator

The generator used to drive recent experiments<sup>2</sup> consisted of one capacitor with the capacitance of  $C_0 = 3 \mu\text{F}$ . The basic parameters of the generator were estimated from the damped oscillation of a “short” circuit, i.e. with short-circuited electrodes (cf. Fig. 3.4 and 3.5).

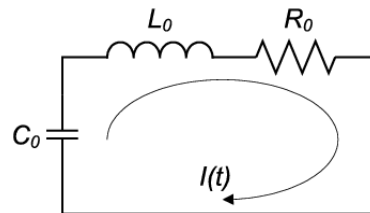


Fig. 3.4: “Short” circuit.

Since it was a simple  $R_0 - L_0 - C_0$  circuit in which the capacitor  $C_0$  was discharged to a  $L_0 - R_0$  load, we could expect the time dependence of  $dI/dt$  to be

$$\frac{dI}{dt} \propto e^{-\frac{R_0}{2L_0}t} \cos \omega t \quad (3.1)$$

<sup>2</sup> The first experiments were performed with four capacitors of  $12 \mu\text{F}$  capacitance. After multiple damages of an insulator we decided to use only one capacitor. Most of the results were very similar.

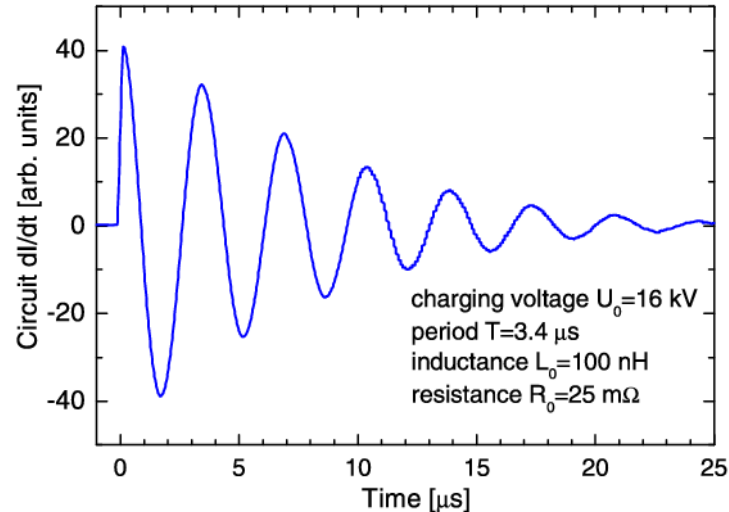


Fig. 3.5: Damped oscillation of a “short” circuit.

where the angular frequency  $\omega$  is equal to

$$\omega = \sqrt{\frac{1}{L_0 C_0} - \frac{R_0^2}{4L_0^2}} \approx \sqrt{\frac{1}{L_0 C_0}} \quad (3.2)$$

For the measured period of  $T = 2\pi\sqrt{L_0 C_0} \approx 3.4 \mu\text{s}$  and damping  $e^{-(R_0/2L_0)T/2} \approx 0.8$  (cf. Fig. 3.5), we calculated the inductance of  $L_0 \approx 100 \text{ nH}$  and the resistance of  $R_0 \approx 25 \text{ m}\Omega$ .

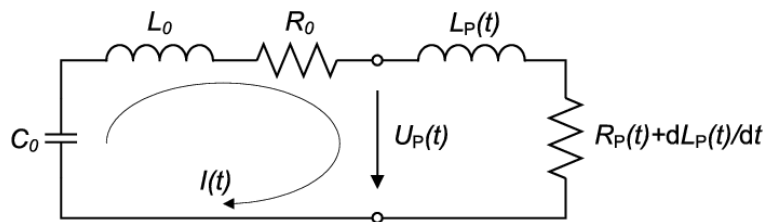


Fig. 3.6: Equivalent electric circuit of the discharge with a fibre.

When a 15  $\mu\text{m}$  carbon fibre was used as a load (see Fig. 3.6), the plasma resistance  $R_P$  and inductance  $L_P$  deeply affected the current waveform, especially  $dI/dt$ . In the case of a 20 kV charging voltage, the current was peaking at  $\approx 80 \text{ kA}$  with a rise time of 650  $\div$  800 ns. More details about our calibration of an electric current will be given in the subsection 3.5.2.

The basic parameters of the Z-150 device are summarised in Tab. 3.2.

Capacitance	$C_0 = 3 \mu\text{F}$
Inductance	$L_0 \approx 100 \text{ nH}$
Characteristic impedance	$Z_0 = \sqrt{L_0/C_0} \approx 180 \text{ m}\Omega$
Resistance	$R_0 \approx 25 \text{ m}\Omega$
Charging voltage	$U_0 = 16 \div 30 \text{ kV}$
Peak current in short-circuit	$I_{\max} \approx 90 \text{ kA}$ for $U_0 = 18 \text{ kV}$
Quarter period for short-circuit	$T_{1/4} \approx 850 \text{ ns}$
Peak current for 15 $\mu\text{m}$ carbon fibre	$I_{\max} \approx 80 \text{ kA}$ for $U_0 = 20 \text{ kV}$
Rise time for 15 $\mu\text{m}$ carbon fibre	$t_{10\% \text{--} 90\%} = 650 \div 800 \text{ ns}$

Tab. 3.2: Basic parameters of the Z-150 device.

### 3.3 Experimental Chamber and Vacuum System

The experimental chamber of a 6.5 cm height and 8 cm diameter was made of stainless steel (see Fig. 3.7 and 3.8). Its diameter was small in order to keep an inductance low. Altogether eight diagnostic ports were available. The size of four diagnostic ports was matched with the vacuum fitting NW40 and the size of the other four ports fitted with NW16.

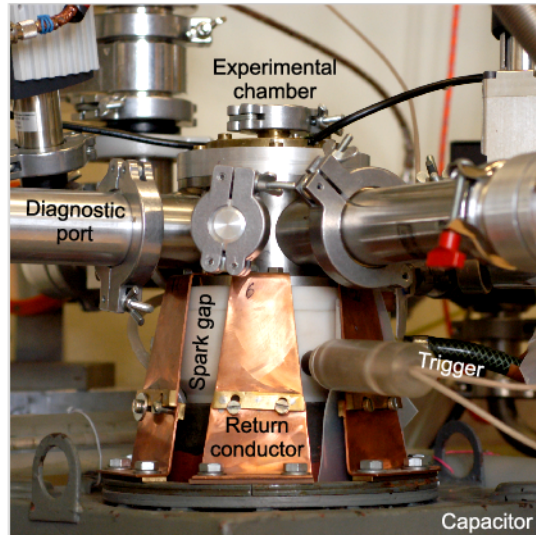
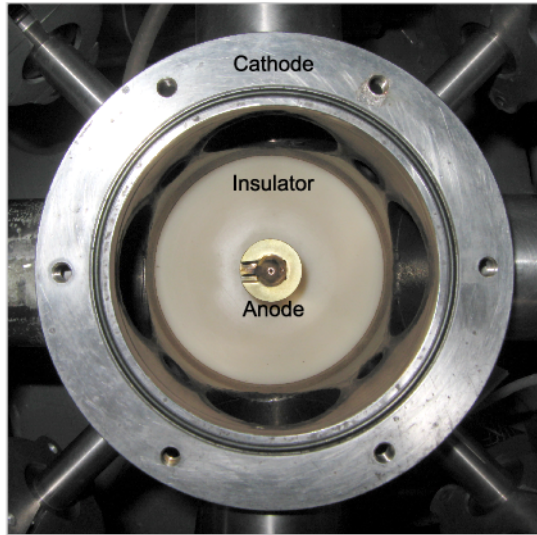


Fig. 3.7: Side-on view of the experimental chamber and spark gap.



*Fig. 3.8: End-on view of the experimental chamber (without the upper cover).*

The electrode system and fixing of carbon fibres varied during our experiment. As we wanted to distinguish general features of the experiment from specific ones, we performed a few experimental series with electrodes from different materials (copper, steel, brass, and bronze) and of different shapes (flat, conical, “bisectional”). The example of brass conical electrodes can be seen in Fig. 3.9.

Carbon fibres were mounted between the live anode and the cathode that were isolated from each other by an alkaline polyamide spacer. The  $dI/dt$  probe was placed near the cathode, in the upper cover of the experimental chamber (see Fig. 3.10).

The chamber was evacuated to a pressure of  $10^{-2}$  Pa. The vacuum was reached with the aid of three Leybold Turbovac50 turbo pumps which were backed by one rotary pump.



Fig. 3.9: Brass conical electrodes with a carbon fibre (15  $\mu\text{m}$  diameter and 9 mm length).

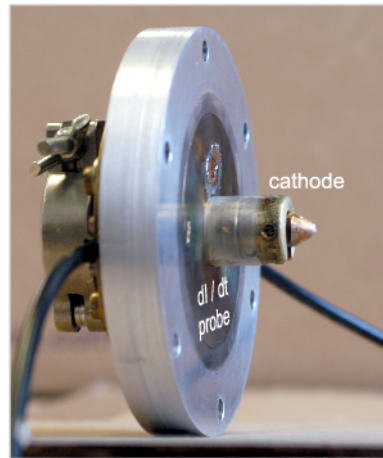


Fig. 3.10: Upper cover of the experimental chamber.

### 3.4 Z–pinch Load

Our Z–pinch was initiated from *carbon fibres* of various lengths and diameters. The carbon fibres of 15  $\mu\text{m}$  diameter and 7  $\div$  9 mm length were most frequently used but also fibres with 6 and 80  $\mu\text{m}$  diameter have been tried<sup>3</sup>. Some of important properties of carbon are presented in Tab. 3.3 and 3.4.

It is well known that Z–pinch dynamics is substantially determined by initial physical properties of a Z–pinch load. The characteristic initial physical property of carbon fibres is their high resistivity. The measured resistance of a 15  $\mu\text{m}$  carbon fibre was approximately 7  $\text{k}\Omega\text{ cm}^{-1}$ . As far as the inductance of a 1 cm long fibre is concerned, the

<sup>3</sup> We preferred 15  $\mu\text{m}$  fibres for three reasons: (i) they could be entirely ablated, (ii) the peak electron temperature exceeded 60 eV, and (iii) the discharge reproducibility was the best among tested fibres.

Density	$1.9 \div 2.3 \text{ g cm}^{-3}$
Concentration	$1.1 \times 10^{29} \text{ atoms m}^{-3}$
Specific resistance	$60 \mu\Omega \text{ m}$
Melting point	$3825 \text{ }^\circ\text{C}$ (sublimate)
Specific heat	$709 \text{ J kg}^{-1} \text{ K}^{-1}$

Tab. 3.3: Significant physical properties of carbon at  $20^\circ\text{C}$  and a pressure of 100 kPa (Lide, 1999).

calculated value of 10 nH is small compared with the short circuit inductance of 100 nH.

Atomization energy	7.4 eV
1 <sup>st</sup> ionization energy	11.3 eV
2 <sup>nd</sup> ionization energy	24.4 eV
3 <sup>rd</sup> ionization energy	47.9 eV
4 <sup>th</sup> ionization energy	64.5 eV
5 <sup>th</sup> ionization energy	392.1 eV
6 <sup>th</sup> ionization energy	490.0 eV

K- $\alpha_1$ transition energy	277.0 eV
K-edge energy	284.2 eV
He- $\alpha$ transition energy	304.3 eV ( ${}^3\text{P}_1$ )
He- $\alpha$ transition energy	307.8 eV ( ${}^1\text{P}_1$ )
Ly- $\alpha$ transition energy	367.5 eV

Tab. 3.4: Significant energies of a carbon atom (Chemical, 2005; Attwood, 1999).

### 3.5 Diagnostics

This subsection brings forward the description of various diagnostic tools that were employed to observe plasma dynamics. The diagnostic set-up that we have used most recently is displayed in Fig. 3.11.

The figure shows that the radiation emitted from the plasma was recorded with two filtered PIN diodes, a hard X-ray detector (PMT and scintillator BCF-12), a gated XUV spectrograph, a time-integrated X-ray pinhole camera, and a gated VUV pinhole camera. The laser probing enabled the visualization of the electron density gradient by the schlieren method. The electrical characteristics of the Z-pinch discharge were monitored by a voltage probe and Rogowski coil.

Fig. 3.11: Schematic diagram and picture of diagnostic set-up, end-on view.

Attenuation	1000× ( $\pm 5\%$ )
Bandwidth	75 MHz
Rise time	$\leq 4.5$ ns
Delay time	approx. 10 ns
Loading	100 M $\Omega$ , 3 pF
Max. voltage	20 kV DC, 40 kV pulse
Compensation	12 ÷ 60 pF

Tab. 3.5: Basic parameters of the P6015 Tektronix HV probe (Tektronix, 1987).

### 3.5.1 Voltage probe

The P6015 Tektronix high-voltage probe (attenuation 1000×, loading 100 M $\Omega$  and 3 pF) was used to monitor the voltage between the electrodes. This probe was developed for measurement of pulses up to 40 kV. The 75 MHz bandwidth and 4 ns rise-time enabled to capture fast changes. The most important characteristics are displayed in Tab. 3.5.

### 3.5.2 Rogowski coil

The Rogowski coil – in other words a toroidal coil with multiple turns, was used to measure a pulsed current in the discharge, or to be more precise the circuit  $dI/dt$ . The current  $I$  flowing through the upper (grounded) electrode also flew through the Rogowski coil. The alternating current  $dI/dt$  and hence alternating magnetic flux then induced the voltage  $L_C dI_C/dt$  inside the current probe.

As the coil was connected via 50  $\Omega$  coaxial cable to the resistor  $R_L = 50 \Omega$ , we can

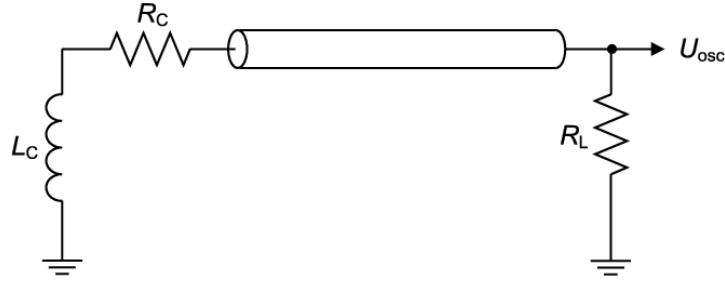


Fig. 3.12: Equivalent circuit of  $dI/dt$  probe.

write the simplified circuit equation as

$$\frac{dI}{dt} \propto L_C \frac{di_C}{dt} + (R_L + R_C)i_C \quad (3.3)$$

where  $R_C$  and  $L_C$  are the resistance and inductance of the Rogowski coil, respectively. In our case, the inductance of the Rogowski coil  $L_C$  was about 400 nH. Hence, the term  $L_C di_C/dt$  was negligible compared with  $R_L i_C$  for frequencies smaller than  $R_L/(2\pi L_C) \approx 20$  MHz. Under this frequency condition and for  $R_C \ll R_L$ , the output voltage at the oscilloscope was proportional to the derivative of the current

$$U_{\text{osc}} \propto R_L i_C \propto \frac{R_L}{R_L + R_C} \frac{dI}{dt} \propto \frac{dI}{dt} \quad (3.4)$$

During the last experiments, the Rogowski coil was replaced by the solenoid with the inductance of  $L_S = 30 \text{ nH}$ . It means that we measured  $dI/dt$  again, but for frequencies up to  $R_L/(2\pi L_S) \approx 250 \text{ MHz}$ .

### Calibration

The Rogowski coil was calibrated by discharging a capacitor into a short circuit (cf. Fig. 3.4 and subsection 3.2). In this simple case, the absolute value of a current could be calculated and thus the current probe could be calibrated against this known value. The current in a short circuit was evaluated as follows:

The equation describing a damped oscillation is

$$U_0 - \frac{\int_0^t I(t') dt'}{C_0} = R_0 I(t) + L_0 \frac{dI(t)}{dt} \quad (3.5)$$

Its solution for an under-damped circuit with

$$\frac{R_0}{2L_0} < \frac{1}{\sqrt{L_0 C_0}} \quad (3.6)$$

equals to

$$I = \frac{U_0}{\omega L_0} e^{-(R_0/2L_0)t} \sin \omega t, \quad \omega = \sqrt{\frac{1}{L_0 C_0} - \frac{R_0^2}{4L_0^2}} \quad (3.7)$$

Since the charging voltage  $U_0$  and capacitance  $C_0$  were known, and since the parameters  $\omega$ ,  $L_0$ , and  $R_0$  could be evaluated from the damped sinusoid (see Fig. 3.5), the current in a short circuit was simply obtained<sup>4</sup>.

However, our Rogowski coil did not measure  $I$  but  $dI/dt$

$$\frac{dI}{dt} = F U_{\text{osc}} \quad (3.8)$$

Therefore, the calibration factor  $F$  was gained after the numerical integration of the voltage measured by oscilloscope

$$I(t) \approx F \int_0^t U_{\text{osc}} dt \quad (3.9)$$

Using this method we determined the calibration factor  $F \approx 2.8 \times 10^8 \text{ A/V s}$ . This value was applied for the estimation of the current in discharges initiated from a fibre.

---

<sup>4</sup> For instance, in the case of 18 kV charging voltage, we calculated the peak current of 90 kA.

### 3.5.3 Filtered PIN diodes

The temporal evolution of XUV and X-ray radiation was detected by two filtered PIN–Si diodes. These PIN diodes were produced by RNDr. Ivo Benc, CSc. in “VÚVET” institution. They were operating as current generators in the reverse bias mode. The equivalent circuit is displayed in Fig. 3.13.

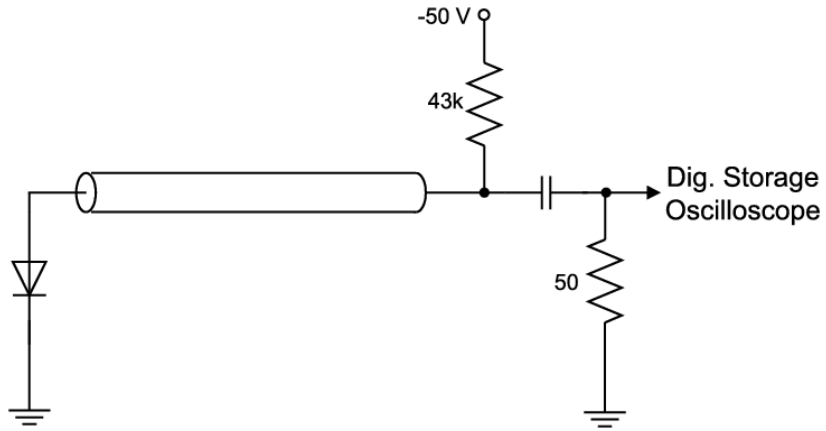


Fig. 3.13: Reverse bias connection of PIN diodes.

These two PIN diodes were differentially filtered by a 15  $\mu\text{m}$  thick Be filter and 0.8  $\mu\text{m}$  thick Al foil. The spectral responsivity  $\mathcal{R}_i$  of filtered PIN diodes was calculated as follows:

In order to create electron–hole pairs, photons have to be transmitted by a filter and a dead layer. At the same time, photons have to be absorbed in the sensitive (intrinsic) layer of a PIN diode. The energy needed for the creation of one electron–hole pair in silicon is  $w \approx 3.62 \text{ eV}$  at room temperature. The quantum efficiency<sup>5</sup>  $\eta$  can be thus estimated

$$\eta = \frac{h\nu}{w} e^{-(\mu_F d_F + \mu_D d_D)} (1 - e^{-\mu_S d_S}) \quad (3.10)$$

where  $\mu_F$ ,  $\mu_D$  and  $\mu_S$  represent absorption coefficients of a filter, dead layer and sensitive layer, respectively. Quantities  $d_F$ ,  $d_D$  and  $d_S$  are thicknesses of relevant layers.

Once the quantum efficiency is known, the spectral responsivity  $\mathcal{R}_i$  can be derived from the ratio of the photocurrent  $i_{\text{PIN}}$  and incident power  $\Phi$  as

$$\mathcal{R}_i = \frac{i_{\text{PIN}}}{\Phi} = \frac{\eta e}{h\nu} \quad (3.11)$$

<sup>5</sup> The ratio of number of incident photons to resulting photoelectrons in the output current.

Substituting  $\eta$  from Eq. 3.10 into Eq. 3.11 we obtain

$$\mathcal{R}_i = \frac{e}{w} e^{-(\mu_F d_F + \mu_D d_D)} (1 - e^{-\mu_S d_S}) \quad (3.12)$$

To calculate responsivities of our PIN diodes, we considered the thickness of a Si sensitive layer to be  $d_S = 10 \mu\text{m}$  and the thickness of a dead layer to be  $d_D = 0.1 \mu\text{m}$ . The spectral dependencies of transmission for filters, a sensitive layer and dead layer were calculated with Henke's data (Henke et al., 1993) provided by a Berkeley lab's website (CXRO, 2004). The transmissions of two Al foils and a 15  $\mu\text{m}$  thick Be filter are displayed in Fig. 3.14. The spectral responsivities of PIN diodes with these filters are shown in Fig. 3.15.

The sensitive area of our PIN diodes was 1  $\text{mm}^2$  and hence we expected the time-response of approximately  $t_{10\%-90\%} \approx 1 \text{ ns}$ . As far as the location is concerned, PIN diodes were placed approximately 20  $\div$  25 cm away from the plasma. Most often we employed uncollimated PIN diodes. However, collimators were used once or twice to avoid the radiation from electrodes. Finally we make a note that PIN diodes are sensitive to high energy particles, particularly the influence of electrons should be considered.

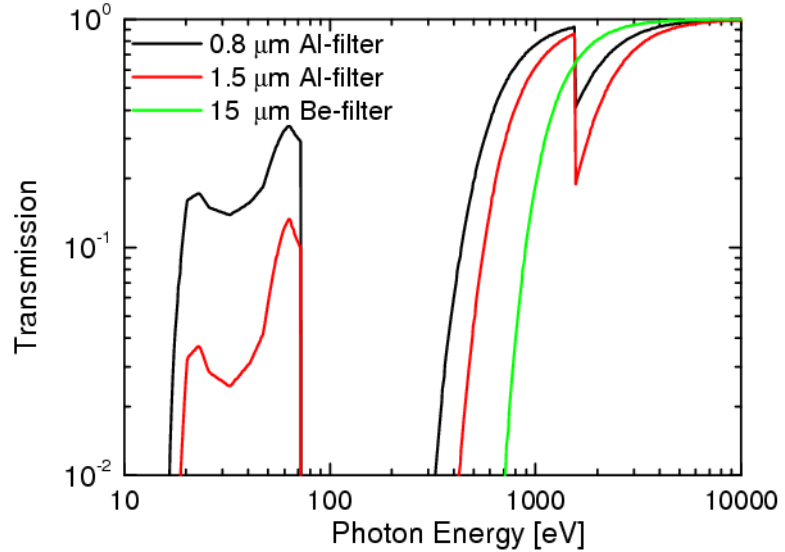


Fig. 3.14: Transmission of an Al and Be filter.

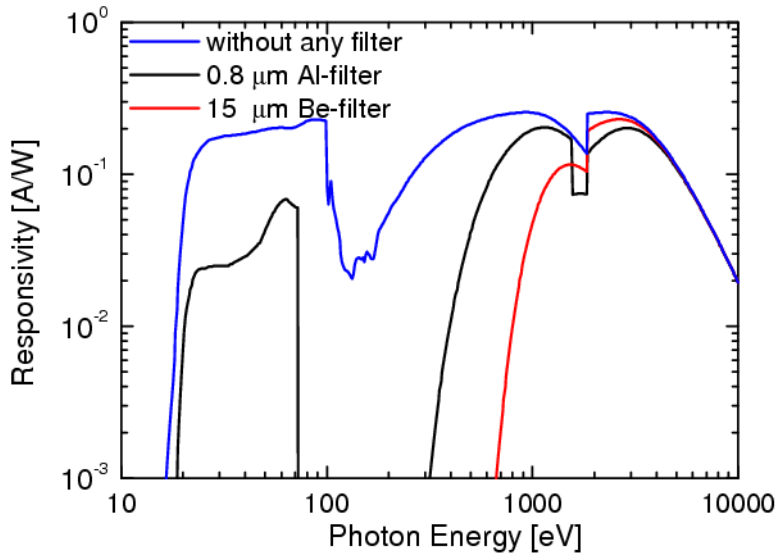


Fig. 3.15: Spectral responsivities of PIN diodes.

#### 3.5.4 Hard X-ray detector

The combination of a scintillator and photomultiplier was used to detect the time evolution of hard X-ray emission. To put it simply, the principle of the detection can be described as follows: an X-ray photon falls upon a scintillation material and produces higher number of visible photons which can be detected with a photomultiplier. In our case, the scintillating fibre Bicron BCF-12 (1 mm diameter and 4 cm length) was followed by the HAMAMATSU H1949-51 photomultiplier tube.

The Bicron fibre consists of a polystyrene-based core and a PMMA cladding (see table 3.6). Scintillation efficiency for the blue emitting BCF-12 is approximately 2.4%.

PMT's parameters are summarised in Tab. 3.7. The HV power supply (HVPS-4) for the PMT tube was developed in the Institute of Plasma Physics and Laser Microfusion (IPPLM) in Warsaw. The applied voltage determined the transit time of electrons. In the case of often used 1.8  $\div$  2.0 kV, the delay of the photomultiplier tube was 35  $\div$  30 ns.

In order to shield background radiation, the scintillation fibre was surrounded by a plastic cone of 6 cm diameter. As far as the energy of detected photons is concerned, it was predetermined by a filter placed in front of the scintillator. The transmission of used filters (100  $\mu$ m or 750  $\mu$ m thick Al filter) is displayed in Fig. 3.16. This figure clearly shows that a 100  $\mu$ m and 750  $\mu$ m Al filter transmits photons with energy higher than 5 keV and 10 keV, respectively.

Fibre	BCF-12
Emission colour	Blue
Emission peak	435 nm
Decay time	3.2 ns
1/e Length	2.7 m
No. of photons per MeV	8000
Core material	Polystyrene
Core refractive index	1.60
Density	1.05
Cladding material	Acrylic
Cladding refrac. index	1.49
Numerical aperture	0.58
No. of H atoms	$4.82 \times 10^{28} \text{ m}^{-3}$
No. of C atoms	$4.85 \times 10^{28} \text{ m}^{-3}$

Tab. 3.6: Basic parameters of the Bicron BCF-12 scintillating fibre (Saint-Gobain, Crystals & Detectors, 2005).

Part number	H1949-1
Gain	$2 \times 10^7$
Rise time	1.3 ns
Transit time	28 ns
Dark current	50 nA
Diameter	51 mm
Effective diameter	46 mm
Window material	Borosilicate glass
Cathode type	Bialkali
Number of stages	12
Peak wavelength	420 nm
Peak responsivity	85 mA/W
Min. wavelength	300 nm
Max. wavelength	650 nm
Output type	Current output

Tab. 3.7: Basic parameters of the HAMAMATSU PMT tube (Hamamatsu, 2005).

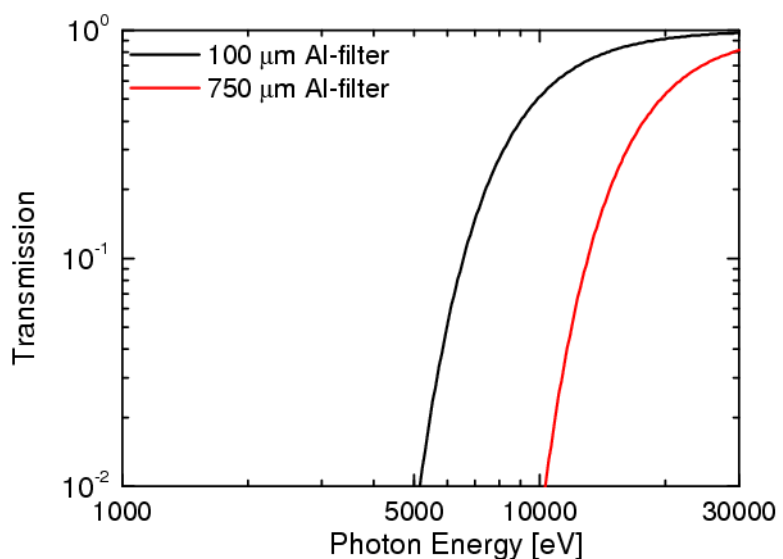


Fig. 3.16: Transmission of Al filters used together with a hard X-ray detector.

### 3.5.5 XUV spectrograph

In this subsection, let us present the spectrograph we used in our experiment. Since XUV spectroscopy was one of the most important contribution of the author to the experiment, the part below covers the subject in more detail. In addition to that, principles of spectroscopy and methods applied in the thesis can be found in appendix A.

#### XUV and X-ray spectral range

Due to the fact that the temperature of Z–pinches varies from several eVs up to tens of keV, a predominant fraction of the electromagnetic radiation is emitted in the XUV and X–ray spectral region. The boundaries of XUV and X–ray ranges are not rigid, but as such traditionally accepted in the fields of X–ray spectroscopy, plasma physics, astrophysics, X–ray laser etc. For the purpose of this paper, we use the wavelength ranges displayed in table 3.8.

Spectral region	Wavelength
hard X–ray	0.01 nm ÷ 0.2 nm
soft X–ray	0.2 nm ÷ 2.5 nm

Spectral region	Wavelength
XUV	2.5 nm ÷ 40 nm
VUV	40 nm ÷ 200 nm

Tab. 3.8: Definition of wavelength ranges used in our work (Pikuz, 2001).

#### Basic principles of XUV spectrographs

Our XUV spectrograph was used to give information about the spectral characteristics of radiation emitted from a fibre Z–pinch. Since we were interested in K– and L–shell emission of carbon ions in particular, we were limited mainly to the XUV spectral region from 2 to 50 nm, i.e. approximately from 20 to 600 eV. The construction of a spectrograph in this spectral region is determined by three important factors.

Firstly, a high resonance absorption in all materials must be considered. It means that spectrographs have to be evacuated and transmission through whatever materials should be restricted. In other words, reflecting elements are preferred.

Secondly, in order to obtain high dispersion and, by extension, high spectral resolution, it is necessary to have the characteristic period of a dispersing element of the order of the wavelength, i.e. several nanometres. Unfortunately, crystal spectrographs can be hardly used above 5 nm because the period of natural crystal lattice is of the order of Å,

i.e. 0.1 nm. The usage of grating spectrographs with the normal incidence is also limited since it is difficult to produce gratings with more than 10000 grooves per 1 mm. Nevertheless, it is possible to employ grazing incidence (the angle of incidence is close to 90°) to have the effective groove spacing higher than 10000 grooves per 1 mm. Moreover, the small grazing angle ensures higher reflectivity of a grating.

Thirdly, we must take into account that we cannot use lenses to focus spectral lines onto the detector. The common way of focusing is the usage of a concave grating with constant groove spacing. The disadvantage of such technique are image defects, astigmatism in particular. Some defects can be reduced in the case of a toroidal grating with varying groove spacing (Harada and Kita, 1980; Kita et al., 1983). In our project we employed “classical” and cheaper way of the detection: a concave spherical reflection grating in the Rowland circle grazing incidence LPS–UVV1 spectrograph.

#### Rowland mounting

In 1881 H. A. Rowland, professor of physics at the Johns Hopkins University, ruled the concave grating, a device of spectacular value in modern spectroscopy. A concave reflection grating can be considered as a concave mirror that disperses; it can be thought to reflect and focus light by virtue of its concavity, and to disperse light by virtue of its groove pattern (Palmer, 2001).

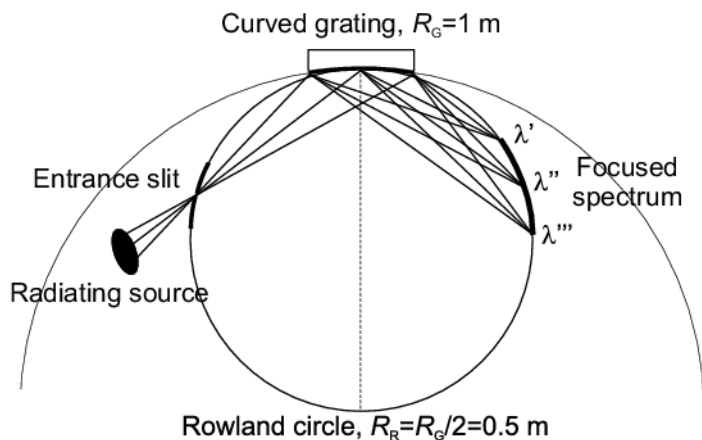


Fig. 3.17: Rowland circle spectrograph.

As regards the Rowland mounting, both the entrance slit and the focused spectrum lie on this circle (cf. Fig. 3.17). Light of three wavelengths  $\lambda'$ ,  $\lambda''$ ,  $\lambda'''$  is shown focused at different points on the Rowland circle. The diameter of the circle  $R_R$  equals to the

tangential radius of curvature of the grating  $R_G$  which passes through the grating centre.

#### LPS–VUV1-3S–M spectrograph

The LPS–VUV1 grazing incidence spectrograph was constructed by the Institute of Spectroscopy (Laboratory of Plasma Spectroscopy, Russian Academy of Science) in cooperation with Schulz Scientific Instruments and European Pulsed Power Research Association (Schulz, 2002). It is a very adaptable proximity–focused, 1-m grazing incidence spectrograph using an off Rowland circle registration scheme (see Fig. 3.19).

Fig. 3.18: LPS–VUV1-3S–M spectrograph.

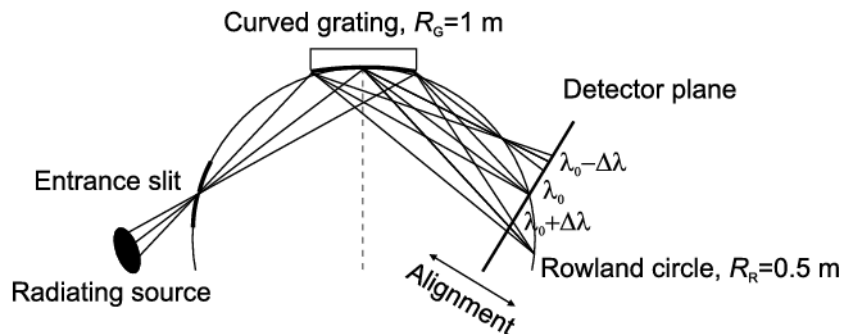


Fig. 3.19: Registration by a plane detector.

In this registration scheme, the exact focusing takes place only for one wavelength  $\lambda_0$ , which corresponds to the intersection point of the detector plane with the Rowland circle. But if the numerical aperture of the spectrograph is small<sup>6</sup>, then it is possible to record the spectrum with sufficient spectral resolution in a wide spectral range  $\lambda_0 \pm \Delta\lambda$ . The alignment to a different  $\lambda_0$  is enabled by changing the distance between the detector plane and the grating. The two main advantages of this scheme are its easy setup and low–cost.

<sup>6</sup> For instance, if the plasma source is localised.

The useful spectral ranges of the spectrograph  $2 \div 14$  nm,  $7 \div 25$  nm, and  $25 \div 60$  nm were achieved with the gratings of 1200, 600, and 300 gr./mm, respectively. The  $2 \div 14$  nm spectral range was significant because of the presence of carbon K-shell spectral lines and thus it was preferably used. The basic parameters of the spectrograph and gratings are summarised in Tab. 3.9 and 3.10.

Grazing angle $\phi_0$	$4^\circ$
Gratings	300, 600 and 1200 grooves / mm
Spectral range	$2 \div 80$ nm
Resolving power	$\lambda/\Delta\lambda > 100$
Angle of incidence on detector	$45^\circ$ or $90^\circ$
Angle between detector plane and spectrograph axis $\alpha$	$10^\circ$
Entrance slit	$30 \div 50$ $\mu\text{m}$
Dimension	$\varnothing 140$ mm $\times 170 \div 350$ mm (length can be adjusted)
Detector	Russian UV film UF-4 or MCP and CCD detector

Tab. 3.9: Basic parameters of the LPS–VUV1–3S–M spectrograph.

Grating no.	1	2	3	4
Radius of curvature	1000 mm	1000 mm	1000 mm	1000 mm
Dimensions [mm]	$30 \times 40 \times 10$	$30 \times 40 \times 10$	$30 \times 40 \times 10$	$30 \times 40 \times 10$
Ruled area [mm]	$28 \times 30$	$28 \times 30$	$28 \times 30$	$28 \times 30$
Grooves / mm	1200	1200	600	300
Groove shape	triangular	triangular	triangular	triangular
Blaze angle	$1^\circ$	$2^\circ$	$2^\circ$	$3^\circ$
Blaze wavelength	2.5 nm	6.2 nm	12.2 nm	42.5 nm
Coating	Au 60 nm	Au 60 nm	Au 60 nm	Au 60 nm
Recommended spectral range	$2 \div 7$ nm	$4 \div 14$ nm $2 \div 7$ nm (2 <sup>nd</sup> ord.)	$7 \div 24$ nm	$24 \div 80$ nm

Tab. 3.10: Basic parameters of gratings (Koshelev, 1999).

### Estimation of wavelengths

We can estimate wavelengths of spectral lines from the grating equation and from the geometry of the spectrograph.

The Rowland circle spectrograph follows the grating diffraction equation (Michette, 1986)

$$d(\cos \phi_0 - \cos \phi) = m\lambda \sqrt{1 + \frac{y^2}{s^2}} \quad (3.13)$$

where  $d$  is the groove spacing,  $\phi_0$  is the grazing angle of incidence,  $\phi$  is the grazing angle of diffraction,  $m$  is the order of diffraction,  $\lambda$  is the wavelength,  $y$  is the location of an imaged point on the entrance slit<sup>7</sup>, and  $s$  is the distance between the entrance slit and the grating centre. In the case of  $y \ll s$  we obtain the well-known equation for the plane grating

$$d(\cos \phi_0 - \cos \phi) = m\lambda \quad (3.14)$$

Fig. 3.20 shows the detection geometry of the spectrograph.

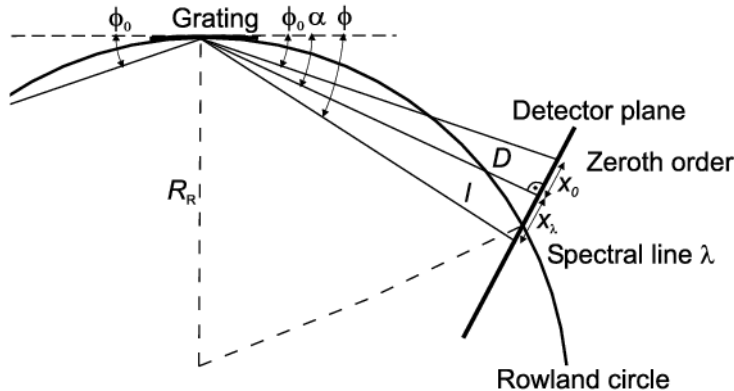


Fig. 3.20: LPS–VUV1 spectrograph geometry of detection.

The position of the spectral line  $\lambda$  can be derived by using the following symbols:

- $D$  – the distance between the grating centre and the detector plane
- $l$  – the distance between the grating centre and the spectral line
- $R_R$  – the radius of the Rowland circle
- $x_0$  – the distance between the zeroth order and the perpendicular from the grating centre upon the detector

<sup>7</sup> The value of  $y = 0$  belongs to the centre of the entrance slit.

- $x_\lambda$  – the distance between the spectral line  $\lambda$  and the perpendicular from the grating centre upon the detector
- $\alpha$  – the angle between the grating “plane” and the spectrograph axis
- $\phi_0$  – the grazing angle of incidence
- $\phi$  – the grazing angle of diffraction

From Fig. 3.20, the  $x$  distance between the spectral line  $\lambda$  and the zeroth order can be determined

$$x = x_0 + x_\lambda = D[\tan(\alpha - \phi_0) + \tan(\phi - \alpha)] \quad (3.15)$$

By expressing the angle  $\phi$  from equation (3.15) and substituting it in the grating equation (3.14), we obtain

$$\lambda = \frac{d}{m} \left[ \cos \phi_0 - \cos \left( \alpha + \arctan \left( \frac{x}{D} - \tan(\alpha - \phi_0) \right) \right) \right] \quad (3.16)$$

The construction parameters such as the angles  $\alpha = 10^\circ$ ,  $\phi_0 = 4^\circ$  and the groove spacing  $d$  are fixed and known with sufficient accuracy (Klír, 2002). Thus, if the distances  $x$  and  $D$  are known, we can easily estimate the spectral wavelength  $\lambda$ , or better to say  $m\lambda$ . However, the zeroth order is usually out of focus and therefore it is not possible to accurately determine the  $x$  distance (see Fig. 3.21). Also, the exact value of the distance  $D$  can be hardly measured. For that reason we determine wavelengths with respect to two reference lines<sup>8</sup> for which the wavelengths are known. It is clear then, that it is essential to surely identify several spectral lines in each spectrum.

The really certain identification was only practicable after gaining experience with several XUV sources, e.g. a carbon fibre Z–pinch, a plasma focus (Kubeš et al., 2003), a Z–pinch initiated from an aluminium wire–array (Klír et al., 2004a, 2005), etc. In the 7÷24 nm region, the reliable identification of lines was made easier when a 0.8  $\mu\text{m}$  thick aluminium filter was used. This technique was based on a sharp aluminium L–absorption edge<sup>9</sup> at approximately 17.1 nm, i.e. at 72.55 eV (cf. Fig. 3.14). One example of a spectrum when an Al filter was applied, is shown in Fig. 3.22. The most intensive spectral line in the spectrum was near the L–absorption edge at 17.1 nm and it was identified as

<sup>8</sup> When two wavelengths are known, we can choose  $x$  and  $D$  for which the dispersion curve Eq. 3.16 best fits the experimental data.

<sup>9</sup> To be more precise, it is L<sub>2,3</sub>–absorption edge, L<sub>2</sub> at 17.01 nm and L<sub>3</sub> at 17.1 nm (Henke et al., 1993).

the transition  $2p\ ^2P - 3d\ ^2D$  of Li-like oxygen ion O VI at 17.3 nm. Other observed spectral lines were identified with the aid of the dispersion curve Eq. 3.16.

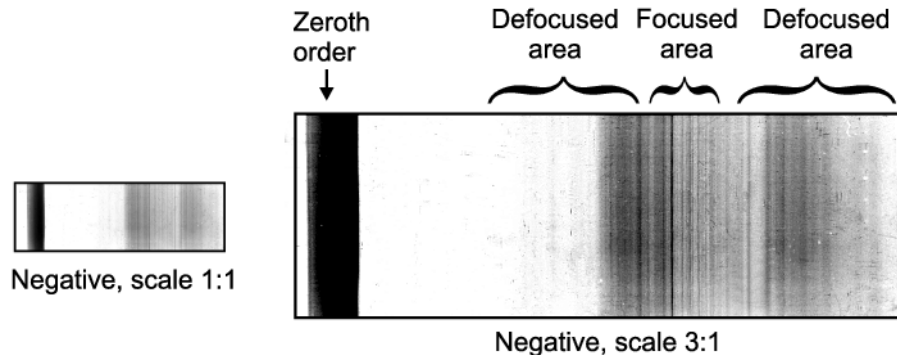
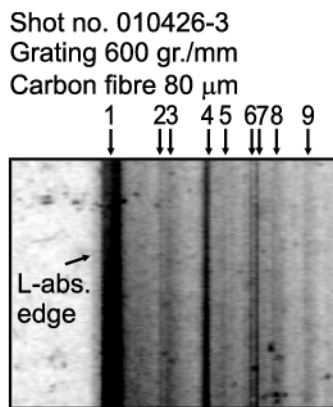


Fig. 3.21: Example of a spectrum recorded by the UV-film UF-4. Grating no. 3.



no.	ion	transition	wavelength $\lambda$ [nm]	
			estimated	tabulated
1	O VI	$1s^2 2p-1s^2 3d$	17.30	17.3
2	O VI	$1s^2 2p-1s^2 3s$	18.37	18.39-18.41
3	O V	$2s 2p-2p 3p$	18.54	18.57
4	O V	$2s 2p-2s 2d$	19.28	19.28-19.29
5	O IV	$2s^2 2p-2s^2 4d$	19.63	19.59-19.60
6	O V	$2p^2-2p 3d$	20.25	20.22-20.24
7	O V	$2p^2-2p 3d$	20.39	20.38-20.39
8	O V	$2p^2-2p 3d$	20.76	20.78
9	O V	$2s 2p-2s 3s$	21.52	21.50-21.52

Fig. 3.22: Calibration of wavelengths by an aluminium filter.

### Identification of transitions

Once wavelengths of observed spectral lines are determined, it is possible to assign them to transitions. For that purpose we use the following spectral databases available online:

- Kelly's Atomic and Ionic UV/VUV Linelist (Kelly, 1987) provided by Harvard–Smithsonian Center for Astrophysics,
- Atomic Spectra Database (NIST, 2005) provided by the National Institute of Standards and Technology (NIST),
- Atomic line database for Astrophysics compiled by Verner et al. (1996) and van Hoff (2005).

In our case, Kelly's compilation of experimental databases is preferred but when transition probabilities are needed, the NIST database is used.

### *Intensity of spectral lines*

Not only the wavelength but also the intensity of a spectral line is of great interest since it enables the estimation of plasma parameters. There are six points we would like to make in this connection.

First thing to be noted is that our spectrograph is not *absolutely* calibrated and we have to get along with *relative* intensities.

Second, the sensitivity of our spectrograph is wavelength dependent. In two separate paragraphs, which bring the following pages, we touch upon the spectral dependence of grating and detector efficiency in particular. Figures 3.23, 3.24, 3.27, and 3.28 will show that it is not accurate to compare spectral lines with substantially different wavelengths. Nevertheless, if the desired accuracy is not extremely high, we can compare spectral lines in the region where the grating and detector efficiency do not change substantially.

Third, the linearity of a detector is limited, especially in the case of a UV film (cf. Fig. 3.26). Consequently the comparison of spectral lines with *similar* intensities is highly appropriate.

The fourth fact we would like to mention is the saturation of spectral lines. In several cases it is possible to check whether a spectral line is near saturation (either by plasma opacity or by the saturation of a detector). Imagine, for instance, that we can find two spectral lines whose intensity ratio is not essentially influenced by plasma parameters and it is almost invariable. If the measured ratio is higher in favour of the weaker line, the stronger spectral line is most likely saturated.

The fifth note is related to the width of a spectral lines. As was already said above, the exact focusing of a spectral line takes place only for one wavelength  $\lambda_0$ . Other lines are defocused to various extents. Therefore, intensities cannot be estimated from the peak value but they have to be calculated by integrating the spectral line profile. In some cases, especially when a spectral line is not intensive, the integration is doubtful since the spectral line could not be separated from background and adjacent lines.

Finally, we make a remark about digitizing a UV film. Our UV films are digitised with a scanner Epson Perfectionist 2400 Photo (4800 dpi, 16 bit grey scale) which was calibrated by the wedge of known optical density.

### Grating efficiency

For a reflection grating, relative efficiency is defined as the energy flow of monochromatic light diffracted into the order (of our interest) *relative to* the energy flow of specular reflection from a polished mirror blank coated with the same material (Palmer, 2001). The determination of grating efficiency in the XUV region is obviously a tricky problem because a spectrograph needs to be calibrated by a suitable XUV source such as a synchrotron. Since such source has not been available and since the producer of our spectrograph has not provided information about grating efficiency we were left with approximate theoretical calculation. Below we present how we went about that.

For a grating with a very low blaze angle  $< 5^\circ$ , the efficiency behaviour is almost perfectly scalar; that is, polarization effects can be neglected. The diffraction efficiency is the highest for the so-called blaze wavelength  $\lambda_B$  that is diffracted by the grating in the same direction as it would be reflected by the groove facets. Above fifty-percent efficiency is obtained from roughly  $0.67\lambda_B$  to  $1.8\lambda_B$  (Palmer, 2001).

More detail dependence was calculated by the MATLAB programme provided by Václav Nemeček (Nemeček, 2002). The calculation was based on the thin grating approximation (Hutley, 1982). When we used the groove spacing, grazing angle of incidence, and blaze angle of our gratings, we obtained efficiency curves that are displayed in Fig. 3.23. Except the grating curvature, the MATLAB programme did not include X-ray interaction with matter. Therefore, the reflectivity of gold coating is discussed further.

The influence of gold coating on absolute efficiency in the  $1 \div 15$  nm region can be seen in Fig. 3.24. In this figure, the reflectivity of a gold layer was calculated for two grazing angles of incidence. It should be noted that the angle of incidence on the groove facets  $\phi_0 = 4^\circ$  is decreased by the blaze angle<sup>10</sup>. Therefore, the angle of  $2^\circ$  is relevant for gratings no. 2, 3, whereas the angle of  $3^\circ$  is relevant for grating no. 1.

Last but not least, we would like to emphasise that experimental calibration could not be fully replaced by theoretical calculations. The theoretical calculation was essential only to exclude possible (unwanted) edges in grating efficiency. Thus the graphs in figures 3.23 and 3.24 are displayed only for the illustration of how grating efficiencies could vary with wavelength.

---

<sup>10</sup> For blaze angles see Tab. 3.10.

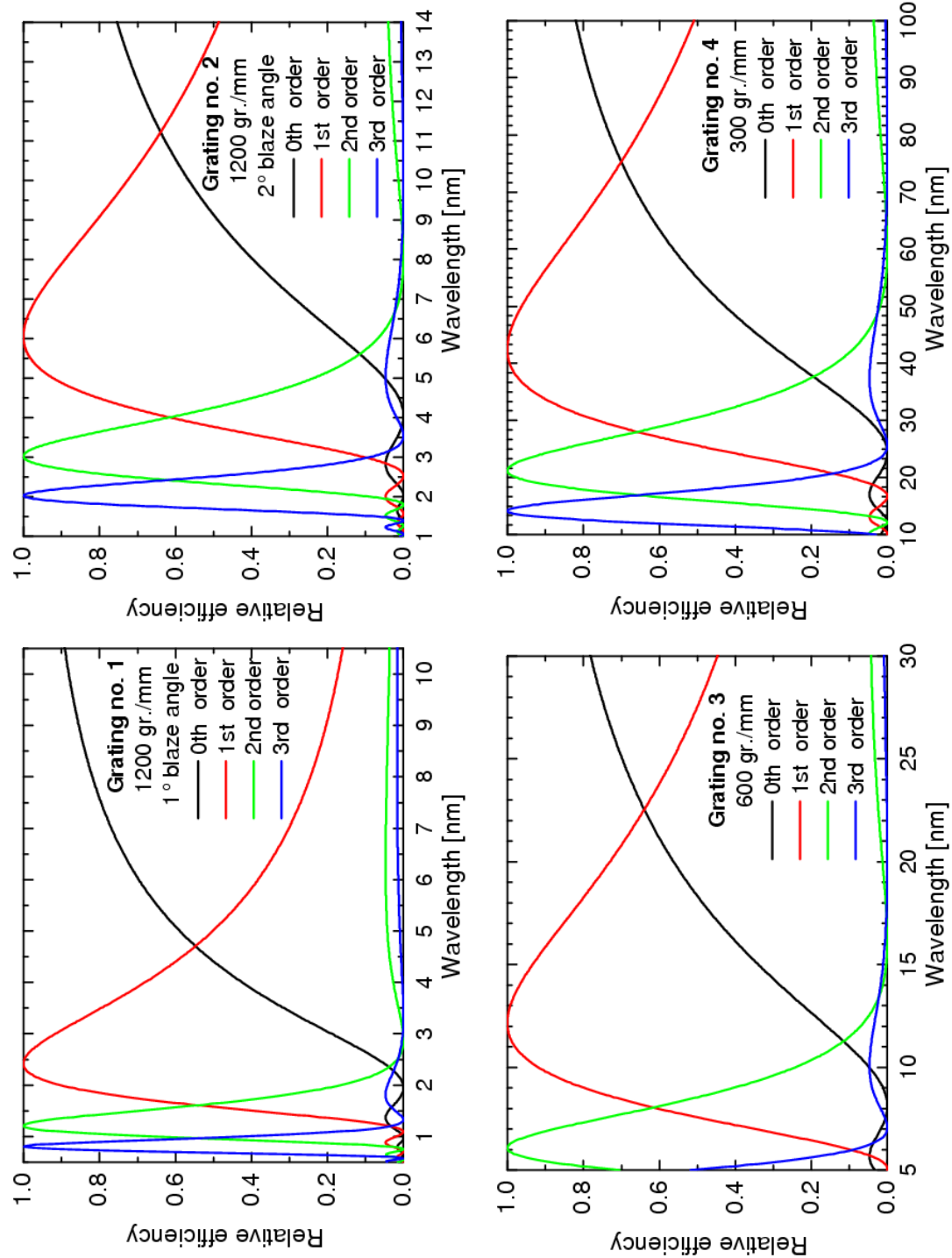


Fig. 3.23: Diffraction efficiency of gratings no. 1–4.

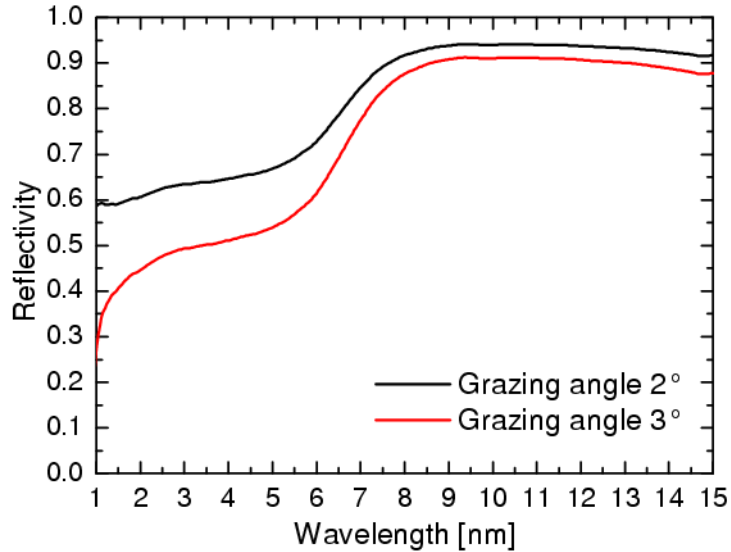


Fig. 3.24: Reflectivity of a gold thick layer for unpolarised light (CXRO, 2004).

### Detectors

The LPS–VUV1 spectrograph was designed for an easy operation in different plasma systems with options for both time–integrated detection using a film and time–resolved recording using active detectors, namely a microchannel plate (MCP, see Fig. 3.25) together with charge coupled device (CCD). The advantage of an ultraviolet film is its higher spectral resolution, whereas MCP detectors offer the nanosecond exposure time and linear response (provided detectors are not saturated). However, we should not forget that the gain of a microchannel plate is very sensitive to applied voltage. Moreover, the gain could vary even between two places in the same MCP section.

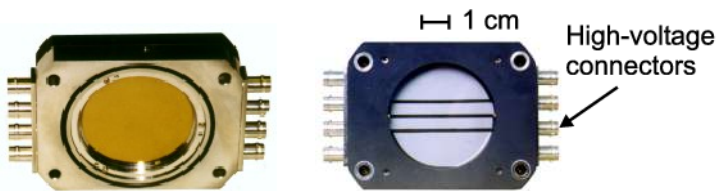


Fig. 3.25: Gold coated MCP detector with 4 stripes (Schulz, 2002).

As regards our experiment, gating pulses were produced by discharging 20 cm long cables via a laser spark gap. The high–voltage power supply was provided by the Institute of Plasma Physics and Laser Microfusion, Warsaw.

We summarised some important parameters of used detectors in tables 3.11, 3.12, 3.13 and figures 3.26, 3.27, 3.28.

Width	35 mm
Recommended spectral region	2 $\div$ 200 nm
Sensitivity $S_\lambda$	$4 \cdot 10^{-8}$ J/cm <sup>2</sup>
Gamma $\gamma_\lambda$	1.2
Thickness of sensitive layer	3 $\div$ 5 $\mu$ m
Fog density $D_0$	0.05
Resolution	> 150 lines per mm
Developer	D-19, dilution 1:5, 20°C, 7–8 min.
Fixer	Fomafix univ. BW, 20°C, more than 10 min.

Tab. 3.11: Properties of the UF-4 ultraviolet film.

MCP type	LPS-MCP/4S-D56
Photocathode	Au
Spectral region	0.1 $\div$ 200 nm
Number of channel plates	1
Usable diameter	52 mm
MCP channel diameter	12 $\mu$ m
MCP channel to channel distance	16 $\mu$ m
Pulse duration	2 $\div$ 3 ns
Gating voltage	4 $\div$ 6 kV
Gain of secondary electron emission	10 $\div$ 1000
Phosphor type	ZnS(Cu), $\lambda \approx$ 520 nm
Fibre optic channel diameter	6 $\mu$ m
Fibre optic channel to channel distance	8.5 $\mu$ m
Conversion efficiency of electrons to photons (energy)	$\approx$ 50%
Pressure	$< 10^{-2}$ Pa

Tab. 3.12: Parameters of the MCP used as an active detector in our spectrograph.

CCD type	digital camera Nikon D1X
Sensor size	23.7 x 15.5 mm
Pixels	5.3 million (4028x1324)
A/D converter	12 bit
ISO speed	125 ÷ 800
Objective	Nikkor (35 ÷ 70 mm/2.8D) & Extension tube

Tab. 3.13: Basic parameters of the CCD detector.

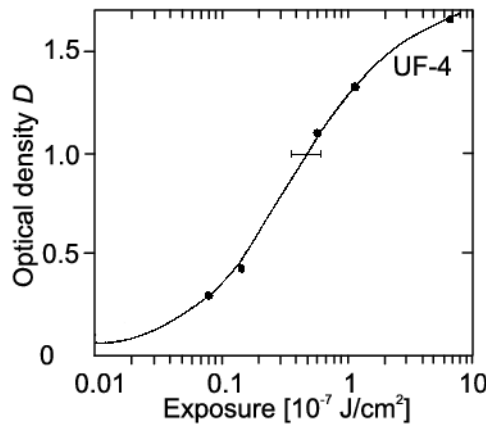
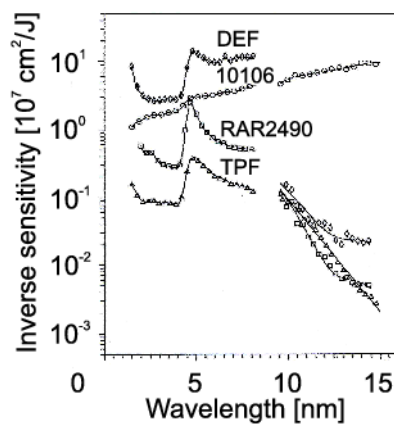
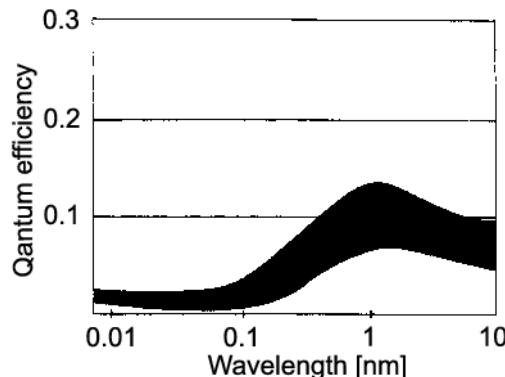
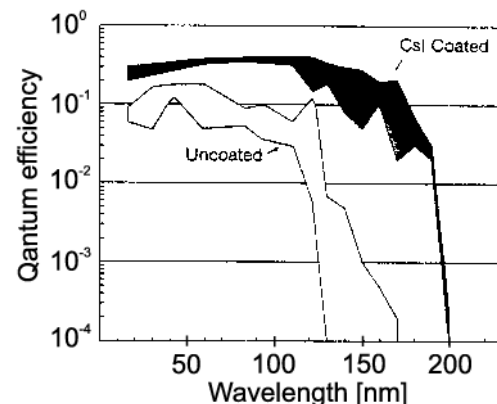
Fig. 3.26: Characteristic curve of the UF-4 film (Shevelko, 1996) ( $\lambda = 18 \text{ nm}$ ,  $20^\circ\text{C}$ , developer D-19 (1:1) – 3 min., fixer – 3 min.).

Fig. 3.27: Inverse sensitivity of films in the 2 ÷ 14 nm region.



(a) X-ray region



(b) VUV region

Fig. 3.28: Typical spectral dependence of quantum efficiency of MCPs.

For the time-integrated detection we applied the UF-4 film. The problem is that this film is not used on a mass scale and so there is not enough information available about its sensitivity. Its absolute calibration was made by Shevelko (1996). Unfortunately, the spectral variation of the sensitivity can be only guessed from the dependence of other films used in this spectral region. On the basis of Fig. 3.27 we can assume that the spectral sensitivity of the UF-4 film does not contain any significant edges in the  $2 \div 4$  nm region where K-shell lines of carbon ions occur.

As far as a microchannel plate is concerned, Fig. 3.28 shows typical photon detection efficiency (BURLE technologies, INC., 2005). In our calculations we considered the efficiency in the  $2 \div 7$  nm region unvarying. Regarding the vignetting of our CCD camera, its influence was not significant.

### Resolving power

The *resolving power*  $\mathcal{R}$  of a spectrograph can be expressed as the dimensionless quantity

$$\mathcal{R} = \frac{\lambda}{\delta\lambda} \quad (3.17)$$

where  $\delta\lambda = \lambda_1 - \lambda_2$  is the difference in wavelength between two adjacent monochromatic spectral lines  $\lambda \approx \lambda_1 \approx \lambda_2$  that can be separated and distinguished.

The maximum attainable resolving power for a grating is

$$\mathcal{R}_{\max} = \frac{2W}{\lambda} \quad (3.18)$$

where  $W$  is the width of the grating in the dispersion plane. Because of short wavelengths in the XUV and X-ray region, the theoretical  $\mathcal{R}_{\max}$  is extremely high. The resolving power is then limited by other factors than a grating itself. For instance in our grating spectrograph, among main limitations belong the dimension and location of the entrance slit and detector elements. The geometric width of the image of the entrance slit (at the plane of a detector) was approximately 30  $\mu\text{m}$ . In the case of the UF-4 film, this is the limiting factor since its grain is less than 7  $\mu\text{m}$ . In the case of MCP and CCD detectors, we must take into account the convolution of the width of an entrance slit (30  $\mu\text{m}$ ), MCP channel to channel distance (16  $\mu\text{m}$ ), fibre optic channel to channel distance (8.5  $\mu\text{m}$ ), and CCD pixel size (25  $\mu\text{m}$  in the plane of MCP). Apart from that, the blurring of a point source takes place also between the MCP and fibre optics and between fibre optics and

the CCD detector. Altogether, we measured the width of actual instrument function of  $100 \mu\text{m}$ . This width then determines the experimental resolving power.

The experimentally determined resolving powers for several wavelengths and gratings are shown in table 3.14. These resolving powers correspond to the focus area of a spectrum. In the defocused part of a spectrum, the resolving power is even smaller and is decreasing with the increasing distance of a focused line from the Rowland circle.

Wavelength	Grating	Film UF-4	MCP and CCD
$\lambda = 4 \text{ nm}$	no. 1	$\delta\lambda = 0.03 \text{ nm}, \mathcal{R} = 130$	$\delta\lambda = 0.15 \text{ nm}, \mathcal{R} = 30$
$\lambda = 8 \text{ nm}$	no. 2	$\delta\lambda = 0.03 \text{ nm}, \mathcal{R} = 250$	$\delta\lambda = 0.15 \text{ nm}, \mathcal{R} = 50$
$\lambda = 18 \text{ nm}$	no. 3	$\delta\lambda = 0.05 \text{ nm}, \mathcal{R} = 360$	$\delta\lambda = 0.15 \text{ nm}, \mathcal{R} = 120$

Tab. 3.14: Resolving power of our spectrograph for some wavelengths, gratings and detectors.

### *Spatial resolution*

The common way of obtaining the spatial resolution is to give an additional slit perpendicularly to the entrance slit of a grating spectrograph. Then the spectrum is dispersed in one direction, whereas the second direction could provide the spatial information of an emitting source. Unfortunately, this technique cannot be easily used in the case of a spherical grating. We are thus restricted to three other possibilities:

First, the spectrum from one locality could be obtained by collimating the radiation falling onto the entrance slit of a spectrograph. In that case, the recorded spectrum contains information from one locality only, to be more precise along the line of sight.

Second, we can take use of the fact that there is only one spectral line that is exactly focused. Other recorded spectral lines do not lie on the Rowland circle and are inherently defocused according to the spatial extensiveness of an emitting source (see Fig. 3.19 on page 54). One exemplary spectrum is displayed in Fig. 3.29. In that shot, the slit of the spectrograph was oriented perpendicularly to the fibre axis. The second diffraction order of carbon K-shell lines was in the focused area, whereas the first order of the Ly- $\alpha$  and He- $\alpha$  lines was visibly defocused. In accordance with this defocusing, it was possible to distinguish two regions radiating in carbon K-shell lines. One was located near the anode and the other was near the cathode. This result agrees also with the gated VUV pinhole image. The disadvantage of such procedure is that the spatial profile is combined with the spectrum and hence it cannot be applied to every case and to every spectral line.

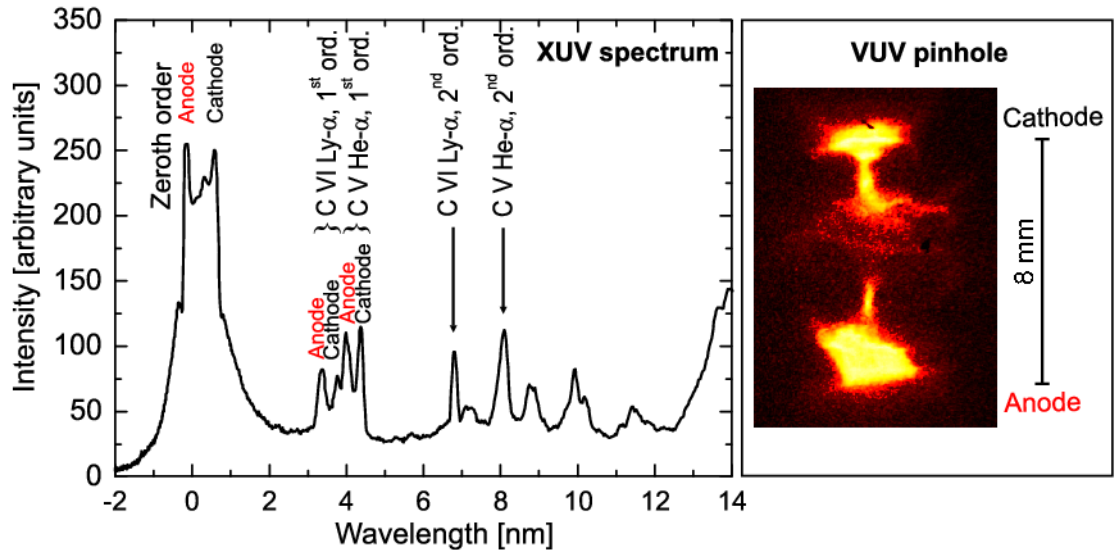


Fig. 3.29: XUV spectrum together with a pinhole image at 320 ns, shot no. 040225-2.

Third, the spatial information of soft X-ray emission can be also acquired by a pinhole camera. When using a proper choice of filters, a pinhole camera provides both spatial and spectral information of a radiating source. On the one hand, spectral information of a pinhole camera is not so in-depth as a spectrograph could give, but on the other hand, 2D spatial resolution is achieved.

In the following subsections, we describe two pinhole cameras, time-integrated X-ray camera and time-resolved VUV camera, that were employed in our experiments.

### 3.5.6 X-ray pinhole camera

The time-integrated pinhole camera was used to obtain X-ray images of an emitting plasma. Fig. 3.30 shows the cross-section of the pinhole camera construction and its position relative to the emitting plasma.

The camera consists of the diagnostic channel, pinhole mount, and film holder. The spatial resolution of the camera is given by

$$d_{\text{RES}} = \varnothing \left( 1 + \frac{1}{M} \right) \quad (3.19)$$

where  $\varnothing$  is the diameter of the pinhole and  $M$  is the magnification of the image. For  $\varnothing = 60 \mu\text{m}$  and  $M = 1.3$ , we obtained the spatial resolution of 105  $\mu\text{m}$ .

In order to gain more information about the emitting plasma we used two pinholes — in other words a two channel pinhole camera. These two channels were differentially filtered with a 15  $\mu\text{m}$  thick Be filter and a 1.5  $\mu\text{m}$  thick Al foil. The same filters were chosen to filter our PIN diodes (see Fig. 3.14 on page 49). The X-ray images were recorded on the Kodak Industrex CX film.

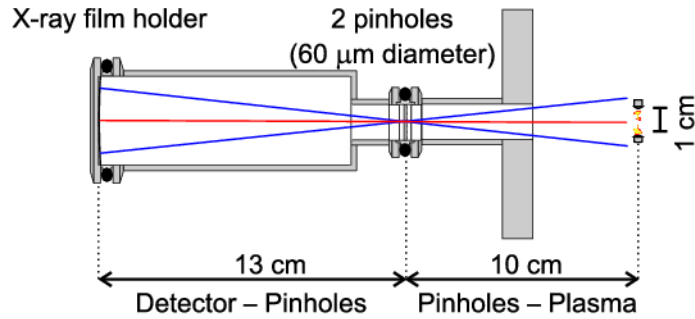


Fig. 3.30: X-ray pinhole camera for time-integrated imaging. Magnification 1.3, spatial resolution 105  $\mu\text{m}$ .

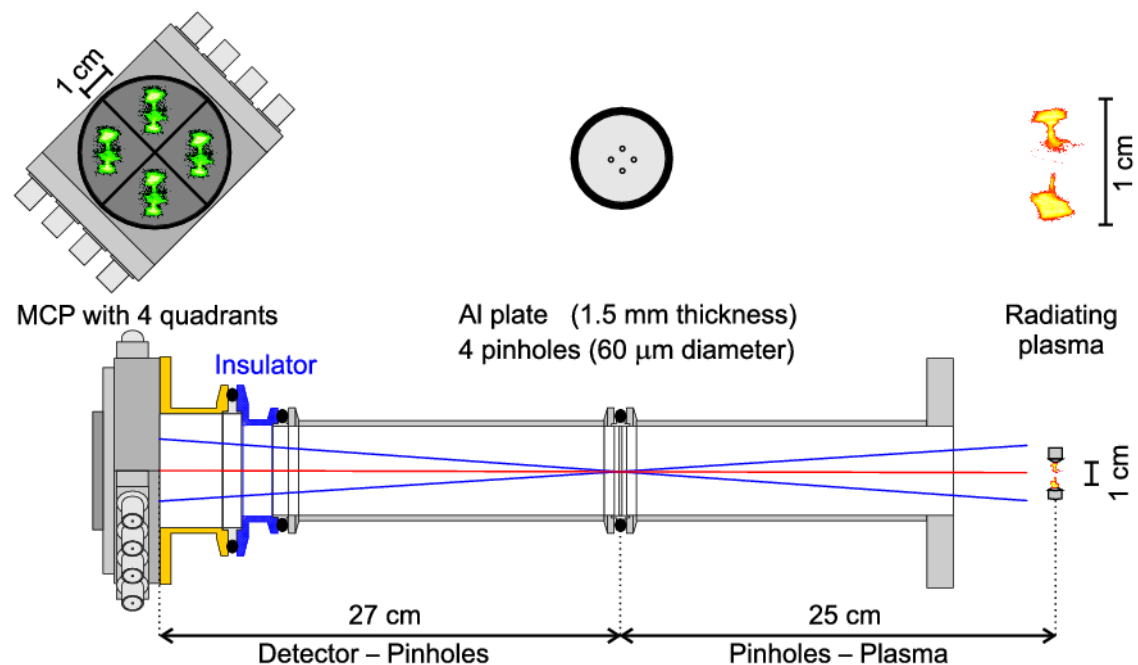


Fig. 3.31: VUV pinhole camera for time-resolved imaging. Magnification 1.1, spatial resolution 200  $\mu\text{m}$ .

### 3.5.7 Gated VUV pinhole camera

The time-resolved information about radiation from the plasma and electrodes was obtained with the gated pinhole camera. Its set-up can be seen in Fig. 3.31. The temporal resolution of the gated pinhole camera was carried out with a 4 frame MCP detector LPS–MCP/4F–D52. The exposure time was 2 ns. The parameters of this microchannel plate were the same as for the microchannel plate LPS–MCP/4S–D56 (see Table 3.12 on page 63). 4 quadrants instead of 4 stripes is the only difference. To record MCP images, the Nikon D1 digital camera was used. The spatial resolution (given by the pinhole diameter, magnification, and resolution of a CCD detector) approached 200  $\mu\text{m}$ . The gated pinhole camera was mostly used without any filter for the detection of VUV radiation ( $\lambda < 200 \text{ nm}$ , see Fig. 3.28 on page 64). Sometimes we used an aluminium filter for the detection of XUV emission.

### 3.5.8 Laser probing

The passive diagnostics described above gave some information about an electric current, voltage and radiation in a discharge. To image the *density* of a plasma, we used *active* probing by a frequency doubled Nd:YAG laser (530 nm wavelength, 3 ns pulse width<sup>11</sup>, 1 mJ energy). In most cases, the optical probing in the schlieren set-up was applied. This technique is sensitive to the refractive index and hence to the electron density gradient. The refractive index  $N(r, \theta, z)$  is dependent on the electron density  $n_e(r, \theta, z)$  by the equation

$$N(r, \theta, z) = \sqrt{1 - \frac{e^2 n_e(r, \theta, z)}{m_e \epsilon_0 \omega^2}} \quad (3.20)$$

$$N(r, \theta, z) \approx 1 - \frac{e^2 n_e(r, \theta, z)}{2 m_e \epsilon_0 \omega^2} \quad \text{for } N(r, \theta, z) \approx 1 \quad (3.21)$$

where  $\omega$  is the angular frequency of the laser beam,  $e$  is the electric charge and  $m_e$  is the mass of an electron.

Variations in the electron density deflect the light passing through a plasma. After the passage through a plasma, the light deviates by an angle  $\vartheta$  given by

$$\vartheta = \int \nabla_{\perp} N(r, \theta, z) dl \quad (3.22)$$

<sup>11</sup> The pulse duration was reduced to 3 ns using a Pockels cell.

where  $\nabla_{\perp}N(r, \theta, z)$  is the gradient of the refractive index transverse to the propagation of a laser beam and  $\int dl$  is the path length along the line of sight.

The layout of the schlieren system used most recently is displayed in Fig. 3.32. The diameters of lenses and stops determined the plasma density that was imaged. In our experiment we used two convex lenses (diameter  $\mathcal{D} = 8$  cm and focal length  $f = 0.75$  m) and stops (diameter  $a = 1.0 \div 3.0$  mm) in their focus. It means that we imaged the regions with deflections

$$\vartheta_{\text{MIN}} = \frac{a}{2f} \leq \vartheta \leq \frac{\mathcal{D}}{2f} = \vartheta_{\text{max}} \quad (3.23)$$

$$(7 \div 20) \times 10^{-4} \leq \vartheta \leq 5 \times 10^{-2} \quad (3.24)$$

Using the approximative equation 3.21 and the angular frequency of the Nd:YAG laser  $\omega = 3.6 \times 10^{15}$  rad s<sup>-1</sup>, we get for the electron density

$$(5 \div 15) \times 10^{24} \text{ m}^{-3} \leq \int \nabla_{\perp}n_{\text{e}}(r, \theta, z)dl \leq 4 \times 10^{26} \text{ m}^{-3} \quad (3.25)$$

To record the development of a plasma, the laser beam was split into two beams and one of them was delayed by 10 ns with respect to the other. The plasma was imaged on the charge coupled device (digital camera Nikon D100, active sensor area 23.4 × 15.6 mm, 6.0 million pixels 3000×2000) with a magnification of 0.6÷0.7. The visible light emitted from the plasma was reduced by polarising and grey filters. The spatial resolution of the schlieren system was less than 30 μm.

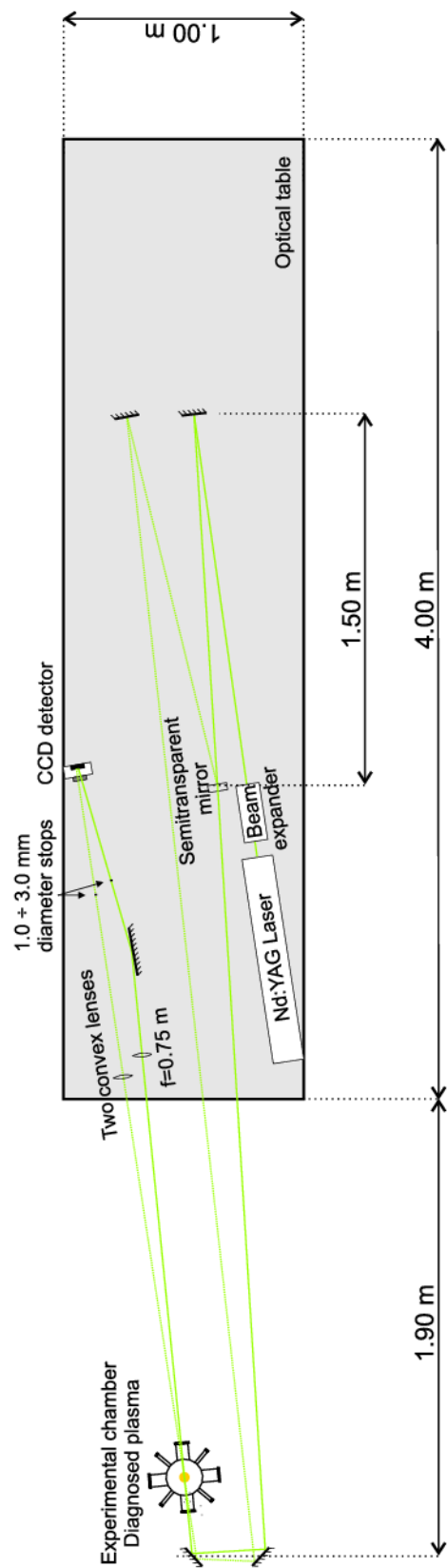


Fig. 3.32: Optical layout of the schlieren system, scale 1:30.

### 3.6 Control and Synchronising Units

In this section we would like to describe the controlling and synchronising a discharge and diagnostics (cf. Fig. 3.33).

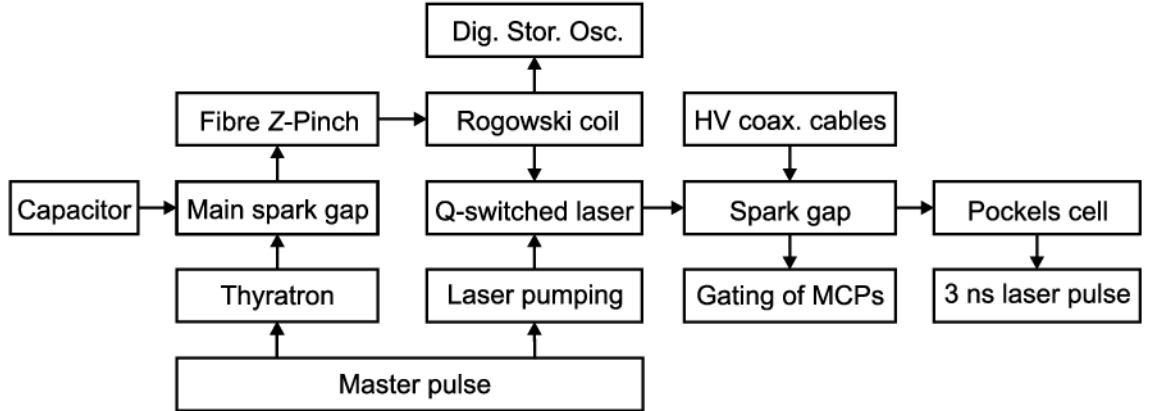


Fig. 3.33: Block diagram of synchronising a discharge and diagnostics.

#### Discharge

The charging of the capacitor was controlled by the digital electronic device C-30 constructed by Kozlík (2002). When the capacitor was charged, the master pulse triggered both the laser pumping and the thyatron. After that, 30 kV thyatron pulse triggered the main spark gap and hence the Z-pinch discharge.

#### Diagnostics

All the diagnostic tools were activated by the discharge breakdown. The signal from the Rogowski coil triggered both oscilloscopes and the Q-switched Nd:YAG laser. After the laser action, the laser beam triggered the spark gap that discharged high voltage cables. The high voltage pulses from these cables then triggered both microchannel plates and also the Pockels cell. The Pockels cell shortened the laser pulse width to 3 ns. The delay of 10 ns between the gating of adjacent MCP quadrants/stripes was carried out by 2 m long coaxial cables. There was also 10 ns time delay between two schlieren images. In order to take these two schlieren photographs simultaneously with two pinhole images and two gated XUV spectra, the laser beam pass length (from the laser output mirror to the Z-pinch plasma) was adjusted. The time delay between the current breakdown

and recording of images was controlled by the length of a coaxial cable between the Rogowski coil and the laser. The jitter approached the value of 5 ns.

### *3.7 Digital Storage Oscilloscopes*

Two digital phosphor oscilloscopes Tektronix TDS3054 and TDS654C were used to store data from the Rogowski coil, voltage monitor, PIN diodes, photomultiplier tube, and gating of microchannel plates. Both oscilloscopes have 4 channels, 500 MHz bandwidth and 5 GS/s maximum sample rate. More information can be found on the website (Tektronix, Inc., 2005).

## *Chapter 4*

### EXPERIMENTAL RESULTS

During the past four years, more than 500 shots have been observed with various diagnostic tools. As a result, we obtained a large number of experimental data and their interpretations. To present these results from each diagnostic tool separately would overburden this thesis. Instead of that, we decided to put results from various diagnostics together so as to delineate gross dynamics of our fibre Z–pinch. We shall illustrate this dynamics on carefully chosen individual shots that most evidently show general characteristics of the pinch.

To make reading easier, the chapter is divided according to different stages that were distinguished in the discharge, namely the breakdown, latent stage, plasma – on – fibre, fibre ablation, discharge in electrode vapour and Z–pinch disintegration (see the upper part of the graph displayed in Fig. 4.1). The time separation between neighbouring phases was chosen somewhat arbitrary since the transition from one stage of the discharge to another was not sharp and varied from shot to shot. All times described in this chapter refer to the start of the current when  $t = 0$ .

Typical waveforms recorded in our Z–pinch are shown in Fig. 4.1. In this particular shot, the Z–pinch discharge was initiated from a 15  $\mu\text{m}$  diameter carbon fibre with the charging voltage of 20 kV. The interesting and characteristic features that we observed were short pulses detected with filtered PIN diodes. The short XUV and X–ray pulses were emitted regardless of what charging voltage, material of electrodes and the diameter of a carbon fibre we tried. Therefore, in the following sections we would like to elucidate the origin of these pulses and to describe what happens in each stage of the discharge. The results of each stage will be also supported by a short interpretation and straightforward discussion, whereas the overall discussion of our Z–pinch is reserved for the next chapter.

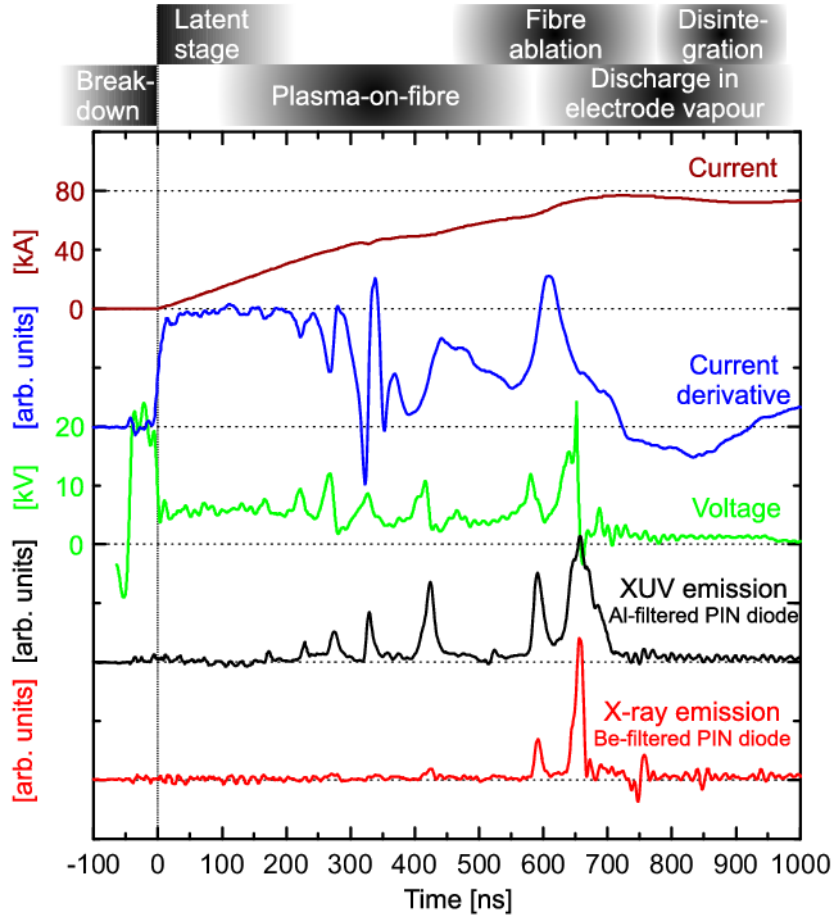


Fig. 4.1: Waveforms of current, current derivative, voltage and PIN diode signals recorded in discharge no. 050128-1. A carbon fibre of 15  $\mu\text{m}$  diameter and 8 mm length, conical electrodes made of bronze, charging voltage of 20 kV.

## 4.1 Breakdown

It is well known that the breakdown phase is very much influenced and determined by initial physical properties of a Z-pinch load. In the case of a carbon fibre, the characteristic initial property of the material is its high resistivity. The measured resistance of a 10 mm long, 15  $\mu\text{m}$  diameter fibre was about 7 k $\Omega$  at room temperature. It is so high resistance that a carbon fibre behaves almost as an insulator and it takes some time for the breakdown to occur. The delay between the applied voltage pulse and the start of the current, i.e. fibre breakdown, is given by the duration of avalanche ionization in strong electric field that is present in gases/vapours desorbed from the fibre surface. The voltage does not collapse until a lower resistance and low density plasma is formed around a fibre. The delay between voltage and current derivative can be seen in Fig. 4.2. In the case of a 20 kV charging voltage, we obtained the delay of  $50 \pm 10$  ns.

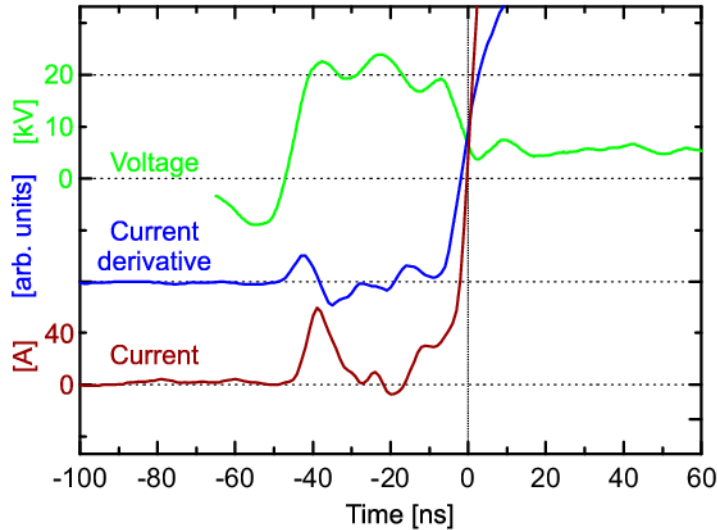


Fig. 4.2: Breakdown phase in discharge no. 050128-1. A 15  $\mu\text{m}$  diameter, 8 mm long carbon fibre, conical electrodes made of bronze, charging voltage of 20 kV.

However, the resistance is not the only fact that influences electrical breakdown. Sarkisov et al. (2002) reported the significant effect of the radial electric field and its polarity. Because of a small fibre diameter and its microroughness, the radial electric field could exceed the axial electric field by a few orders of magnitude. In our case<sup>1</sup>, the polarity of radial electric field was positive, i.e.  $E_r > 0$ . Since the electric field increased the potential barrier for electronic emission from the fibre surface, the breakdown started from the cathode when the electric field was the lowest. As a result, the deposited energy towards the cathode was lower because the direct heating was prevented by a current shunted from a fibre.

It is also interesting to note that breakdowns of 15  $\mu\text{m}$  diameter carbon fibres were quite reproducible, whereas we had serious problems with 5  $\mu\text{m}$  tungsten wires (initial resistance of about 25  $\Omega$ ) as well as with fibres from deuterated polyethylene (insulator). The reason for that lies neither in resistivity nor in the polarity of electric field, but most probably in the surface properties of a carbon fibre. In this connection we should perhaps add that we saw something like a “luminescing” column around a carbon fibre before the trigger pulse was applied to a spark-gap<sup>2</sup>. We attributed this phenomenon to a gas/vapour desorbed from the fibre surface. But whatever the explanation is, this phenomenon could effectively facilitate the breakdown process and also prevent higher energy deposition

<sup>1</sup> The part of a fibre near the anode is positive and chamber walls are negative. We expect the radial electric field near a fibre  $E_r \approx 10^8 \text{ V m}^{-1}$ .

<sup>2</sup> At that moment, there was a 40  $\mu\text{A}$  current flowing through a fibre (see the electric scheme in Fig. 3.3).

into a fibre core. We measured that the Joule heat produced before the voltage collapse was about 20 mJ. It is much lower than the energy required for atomization of a 15  $\mu\text{m}$  carbon fibre which is about 200 mJ. Moreover, the energy of 20 mJ was deposited rather to ambient vapour than to a fibre. Hence, the diameter of a carbon fibre remained almost unchanged after the breakdown.

## 4.2 Latent Stage

The “latent” stage of the discharge represents the time after the breakdown and before the appearance of XUV pulses, i.e. from 0 ns to about 150 ns for 15  $\mu\text{m}$  diameter fibres.

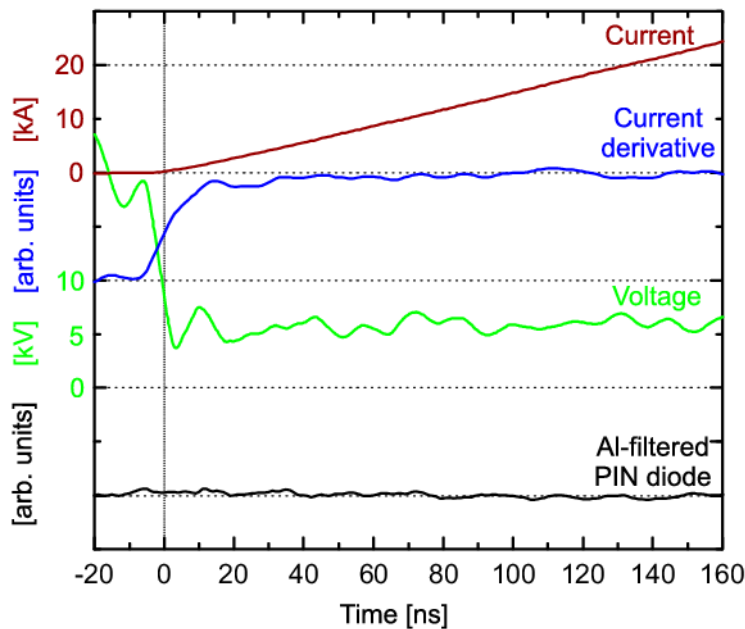


Fig. 4.3: Latent phase in discharge no. 050128-1. A 15  $\mu\text{m}$  diameter, 8 mm long carbon fibre, conical electrodes made of bronze, charging voltage of 20 kV.

This stage has not been explored in much detail. The main reason was the lack of serious interest in this stage. It was supported by the fact that this phase was difficult to detect. During the first 100 nanoseconds the plasma emitted a small amount of radiation and the electron density was too low to be detected by the schlieren system. Besides that, all the diagnostic tools were triggered mostly by the discharge breakdown and then we were not able to obtain gated images before 150 ns. Our knowledge of the latent stage came from the non-systematic investigation only. However few experimental data we obtained, we do have certain notion about the plasma development after the breakdown.

According to theoretical predictions<sup>3</sup> and experimental observations (Lorenz et al., 1998) we can assume that a low density plasma expanded to a radius of several millimetres. The expansion velocity was limited by the sound speed that is typically  $10^4 \text{ m s}^{-1}$ . The expansion was most likely slowed down by an increasing current. At which time this happened depended on the current rise and the properties of a plasma column.

Further information could be inferred from Fig. 4.3, especially from the voltage and  $dI/dt$  waveforms. It is evident that the plasma development was not so dramatic as in the “plasma–on–fibre” stage (cf. Fig. 4.1). Nevertheless, it is still possible that similar processes might occur in both stages, only less powerful in the latent stage due to smaller current. When we subtracted the inductive contribution, the voltage across the plasma was less than 1 kV. For 10 kA current we obtained  $< 0.1 \Omega$  resistance.

Unfortunately, first images were recorded late in the latent stage. Fig. 4.4 shows that at 100 ns most of the VUV radiation came from the vicinity of electrodes, especially the anode. This observation agrees with the XUV spectrum displayed in Fig. 4.5 where the spectral lines of oxygen, copper and zinc ions were identified. The electron temperature estimated from Li– and Be–like ions O VI was  $15 \div 25 \text{ eV}$ . The temperature measurement was done by the FLY code (see appendix B). On the one hand, the temperature was below 25 eV since the O VI spectral line at 11.6 nm (2s–4p and 2p–5d transitions) was too weak in comparison with the spectral line at 17.3 nm (2p–3d transition). But on the other hand, because the O VI spectral line at 17.3 nm was at least five times stronger than the transition 2s2p–2s3d of Be–like oxygen O V, the temperature was higher than 15 eV. The merging of spectral lines and continuum–like radiation caused that it was problematic to separate spectral lines. In addition, we do not know what the plasma density was. That was the reason why more accurate estimation of the temperature was not achieved.

<sup>3</sup> The line density of a plasma (see the line density of  $8 \times 10^{17} \text{ m}^{-1}$  on page 83) is of the order of the critical density  $N_c = 1.3 \times 10^{18} A(1+z)/z^3$  (Haines et al., 1996), where  $A$  stands for the atomic mass number and  $z$  for the ionic charge. Therefore, microinstabilities could be triggered (see page 33). Consequently, the plasma pressure exceeds the magnetic pressure and the plasma expands. But even if the Bennett relation holds, the current would have to follow the Haines–Hammel curve (Hammel et al., 1983) to prevent the expansion. As our current rise time of about  $10^{11} \text{ A s}^{-1}$  is slow, a plasma column has to expand early after the breakdown.

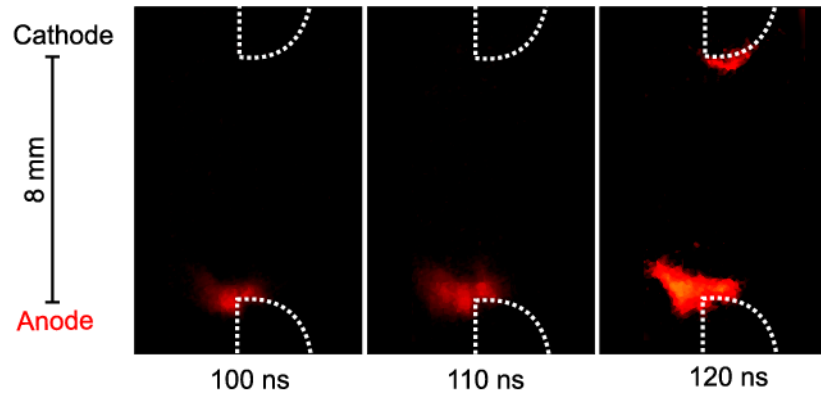


Fig. 4.4: VUV pinhole images recorded in discharge no. 020215-3. A carbon fibre of a  $15\text{ }\mu\text{m}$  diameter and 8 mm length, “bisectional” electrodes made of brass, charging voltage of 20 kV.

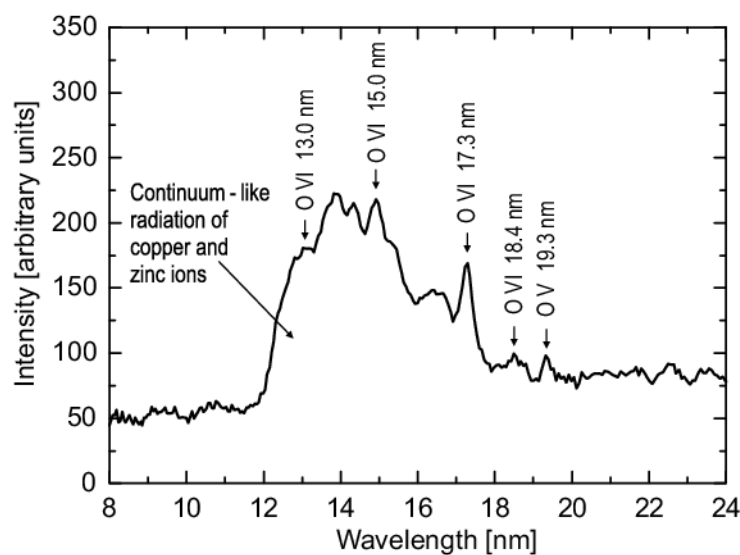


Fig. 4.5: XUV spectrum detected at 110 ns, shot no. 011016-1. A  $80\text{ }\mu\text{m}$  diameter, 8 mm long carbon fibre, “bisectional” electrodes made of brass, charging voltage of 23 kV.

### 4.3 Plasma-on-Fibre<sup>4</sup>

Fig. 4.6 shows typical waveforms of the current derivative  $dI/dt$ , voltage<sup>5</sup> and PIN diode signals between 100 and 500 ns.

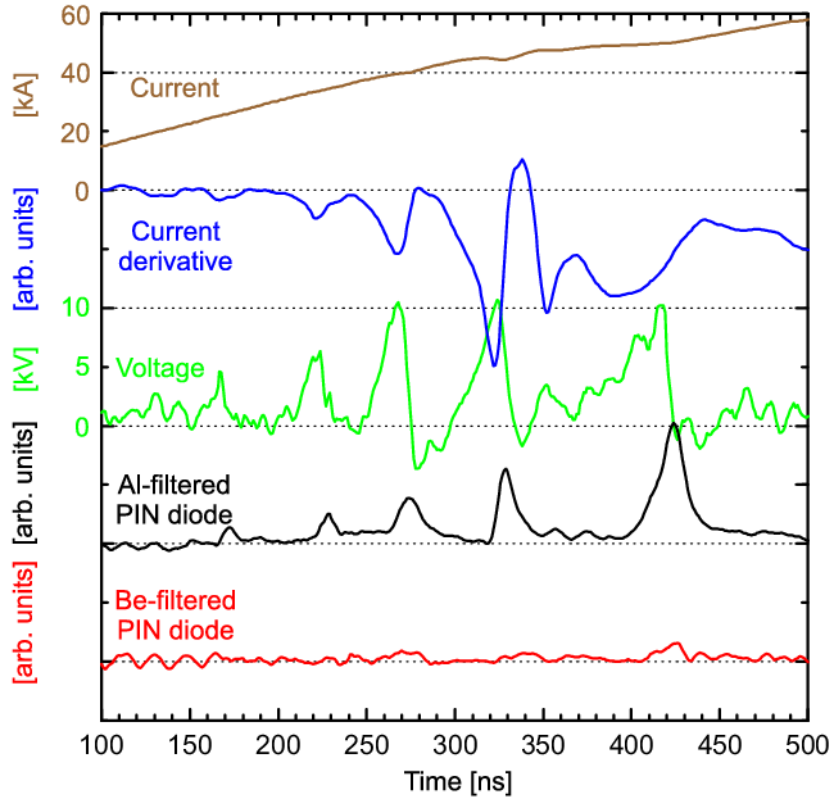


Fig. 4.6: Plasma – on – fibre phase in discharge no. 050128-1. A 15  $\mu\text{m}$  diameter and 8 mm long carbon fibre, conical electrodes made of bronze, charging voltage of 20 kV.

This phase was characterised by short XUV pulses of 10  $\div$  30 ns FWHMs<sup>6</sup>. When the collimated PIN diode was used, the pulse width was sometimes smaller than 3 ns. The first XUV pulses appeared at about 150 ns. The intensity of these XUV pulses was increasing with the growing time. Because the signal of the Be-filtered PIN-diode was very small, the energy of detected photons was mainly in the 20  $\div$  70 eV region

<sup>4</sup> This term was derived by analogy from the expression “plasma – on – wire” which was used by Wessel et al. (1992) to name the imploding aluminium-plasma jet onto a coaxial wire. However, the implosion onto a metal wire differs from the implosion onto a fibre with a very low conductivity, and so we decided to use the term “plasma – on – fibre” instead of “plasma – on – wire”.

<sup>5</sup> In this case, we subtracted the induction contribution of the voltage. It means  $U'_P = U_P - L_P \dot{I} = (R_P + \dot{L}_P)I$ . To be more precise, we had to subtract also the induction contribution of the electrodes and cable connected with the voltage probe.

<sup>6</sup> Despite the fact that the shot – to – shot variation resulted in a different number of pulses, their intensities, and widths, it was possible to identify characteristic features of our fibre Z – pinch.

(cf. spectral responsivity of Al-filtered PIN diode in Fig. 3.15 on page 50). For instance, the energy of  $20 \div 70$  eV photons emitted during the last XUV pulse in Fig. 4.6 was about 100 mJ, whereas the energy of  $> 1$  keV photons approached 1 mJ.

The notable feature of the radiation was the strong correlation with the voltage and the circuit  $dI/dt$ . The gradual fall of  $dI/dt$  as well as the growth of the voltage up to 10 kV can be clearly seen before each pulse in Fig. 4.6. These phenomena were typical for our fibre Z-pinch regardless of the diameter of fibre or the shape and material of electrodes that were used. Hence it was our primary interest to find out how it happened that short XUV pulses occurred.

#### 4.3.1 Implosion

The only diagnostic tool which provided images of what happened before XUV pulses was the gated VUV pinhole camera. For example, the behaviour before the first XUV pulse is displayed in Fig. 4.7. In this shot, during the gradual fall of  $dI/dt$ , VUV images show the relatively stable<sup>7</sup> implosion of the coronal plasma onto a fibre. The implosion velocity approached the value of  $2 \times 10^5$  m s<sup>-1</sup>. The compression ratio was about 10. Because the compression caused the increase of the plasma inductance and resistance, we observed the drop of  $dI/dt$ .

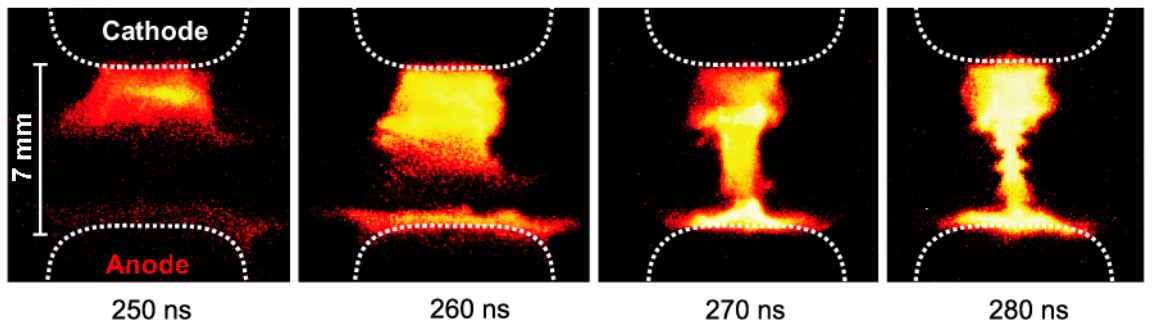


Fig. 4.7: VUV pinhole images detected in shot no. 030828-1. The collapse of a coronal plasma onto a fibre with the velocity of  $2 \times 10^5$  m s<sup>-1</sup>. The last image corresponded to the peak of the 20 ns XUV pulse. A 15  $\mu$ m diameter and 7 mm long carbon fibre, electrodes made of steel, charging voltage of 20 kV.

<sup>7</sup> The implosion seemed to be stable. The development of instabilities was observed first at the end of the implosion, during the stagnation. This stability could be ascribed to snowplough stabilization (see page 36). However, the skin-depth of several millimetres was comparable with the radius of the imploding plasma. Thus a diffuse Z-pinch was formed and “typical” snowplough did not occur.

### Zipper effect

In most cases the implosion was non-symmetric<sup>8</sup>. As a result, the radiation was “zippering” along the fibre with the velocity of up to  $1 \times 10^5 \text{ m s}^{-1}$ . This phenomenon could be seen in the images in Fig. 4.8. The zipper was spreading mainly from the cathode, however, zippering from the anode was also observed.

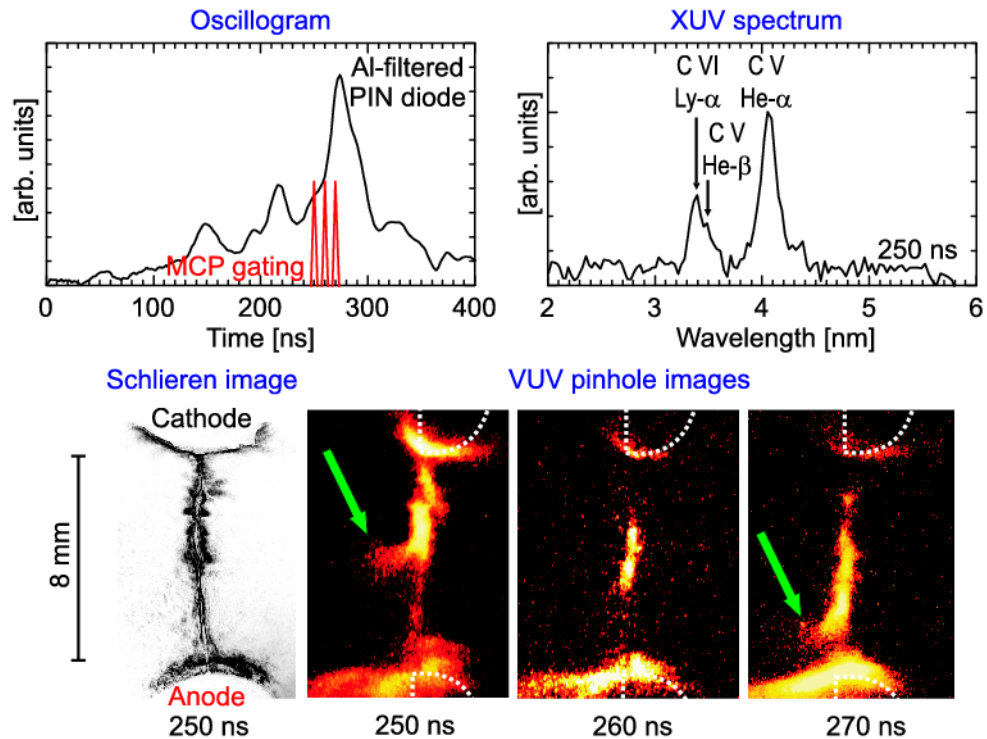


Fig. 4.8: Zippering from the cathode with the velocity of  $10^5 \text{ m s}^{-1}$ , shot no. 030321-1. A 15  $\mu\text{m}$  diameter and 8 mm long carbon fibre, bisectional electrodes made of steel, charging voltage of 20 kV, schlieren sensitivity  $n_e \approx 5 \times 10^{18} \text{ cm}^{-3}$ .

At this point we would like to point out that it was necessary to detect a low density corona in order to recognise the implosion. Therefore, we have never seen the implosion in schlieren images. As regards the pinhole camera, when an Al-foil was used to filter radiation (Fig. 4.9), we observed only the zipper effect without any evidence of the implosion. Also, we would like to draw the attention to the fact that in this shot the radiation from a fibre exceeded the emission from regions near electrodes. That was observed although an Al-filter did not permit K-shell spectral lines of carbon ions.

<sup>8</sup> It could be the consequence of the polarity effect during the breakdown. As it was mentioned above, the direction of the radial electric field influences the energy deposition (Sarkisov et al., 2002). According to this model, the implosion should stagnate first close to the cathode.

*Fig. 4.9:* Zippering with the velocity of  $10^5 \text{ m s}^{-1}$ . The last image corresponded to the peak of the 20 ns XUV pulse. XUV pinhole images (0.8  $\mu\text{m}$  thick Al filter was used) in shot no. 021031-1. A carbon fibre of 15  $\mu\text{m}$  diameter and 8 mm length, bisectional electrodes made of brass, 12  $\mu\text{F}$  capacitors, charging voltage of 20 kV.

### Plasma density

The plasma density during the implosion could be derived from the implosion velocity which approached  $2 \times 10^5 \text{ m s}^{-1}$ . This value should be of the order of the Alfvén velocity, i.e.  $v_{\text{imp}} \approx \sqrt{\mu I_0^2 / \pi N_i M_i}$  (see Eq. 2.43 on page 35). For the electric current  $I = 40 \text{ kA}$  and for the mass of carbon ion  $M_i \doteq 2 \times 10^{-26} \text{ kg}$ , we obtain the line density of ions in the coronal plasma  $N_i = 8 \times 10^{17} \text{ m}^{-1}$ . According to Tab. 3.3, we take the density of carbon atoms in a fibre  $n_a \approx 1.1 \times 10^{29} \text{ m}^{-3}$ . Then the line density of a 15  $\mu\text{m}$  diameter fibre is  $N_a \approx 2 \times 10^{19} \text{ m}^{-1}$ . From these values we may conclude that roughly<sup>9</sup> a few per cents of the total mass of a fibre were ablated at that time.

However, the line density of  $N_i = 8 \times 10^{17} \text{ m}^{-1}$  determines not only the mass of a fibre ablated but also the average plasma density. First, if we assume that the diameter of a plasma column at the beginning of the implosion is of the order of one centimetre (cf. Fig. 4.7), we obtain the ion density of about  $n_i = N_i / \pi r^2 \approx 10^{16} \text{ cm}^{-3}$ . Second, at the end of plasma implosion we observed the plasma diameter of the order of millimetre and hence the ion density was about  $10^{18} \text{ cm}^{-3}$ . This value corresponds to the plasma density estimated from schlieren diagnostics (see page 87).

<sup>9</sup> This is a rough estimation because on the one hand, atoms from electrodes were present in the coronal plasma and therefore the number of ablated carbon ions could be lower, but on the other hand, however, we could expect that not all the ablated carbon ions were participating in the implosion. By the way, we do not know whether 100% of the current followed the implosion to the axis.

### Plasma temperature

Before we present results of temperature measurement, it should be emphasised that the plasma column was inhomogeneous in temperature. It means that the determination of temperature depends on the choice of spectral lines which are used for calculation. In our case, the electron temperature could be estimated from (i) Li- and Be-like oxygen ions, (ii) Li-like carbon ions and (iii) K-shell spectral lines of carbon ions. The first two choices gave information mainly about colder regions<sup>10</sup> where Li-like ions occur in an abundance. That is why we decided to use mainly the lines of H- and He-like carbon ions.

In most cases, K-shell lines of carbon ions were not observed at the beginning of the implosion, i.e. before 150 ns. According to Fig. 4.10, it was a result of a low ion density and temperature. The electron temperature was likely below 40 eV.

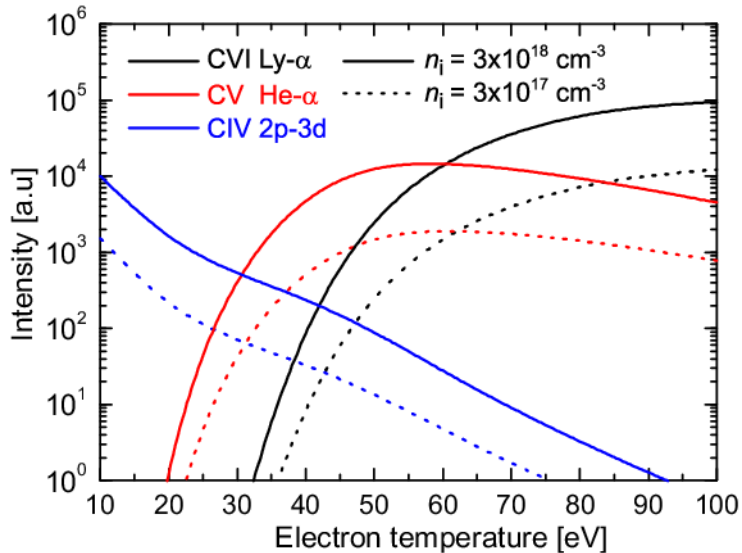


Fig. 4.10: Temperature dependence of intensities of selected lines calculated by the FLY code for  $n_i = 2 \times 10^{17} \text{ cm}^{-3}$  (dotted lines) and  $n_i = 2 \times 10^{18} \text{ cm}^{-3}$ .

The He- $\alpha$  line was observed first during the implosion, but especially shortly before the stagnation. The evolution of Ly- $\alpha$  and He- $\alpha$  lines before the stagnation is demonstrated in Fig. 4.11. If the plasma is optically thin, the Ly- $\alpha$  to He- $\alpha$  ratio is almost density independent and can serve as a convenient method for temperature measurement. It can be clearly seen in Fig. 4.11 that the Ly- $\alpha$  to He- $\alpha$  ratio was increasing during the implosion and thus the temperature was growing. This agrees with the increasing

<sup>10</sup> Using the ratio of C IV, O V and O VI lines, the electron temperature was about 20 eV regardless the phase of the discharge.

kinetic pressure that was inferred from the deceleration of the implosion velocity before the stagnation.

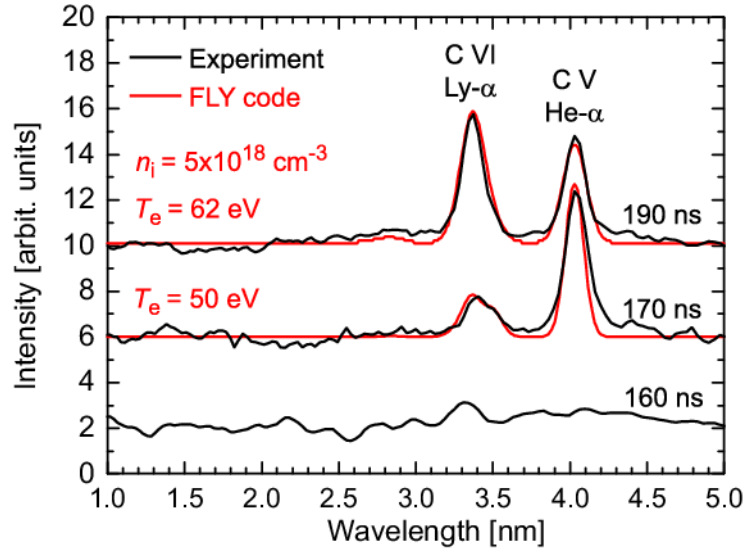


Fig. 4.11: XUV spectrum in shot no. 011031-3. Synthetic spectra simulated with the FLY code for optically thin plasma. The last spectrum was detected 10 ns prior to the peak of the XUV pulse of a 20 ns FWHM. A carbon fibre of 15  $\mu\text{m}$  diameter and 8 mm length, bisectional electrodes made of brass, 12  $\mu\text{F}$  capacitors, charging voltage of 23 kV.

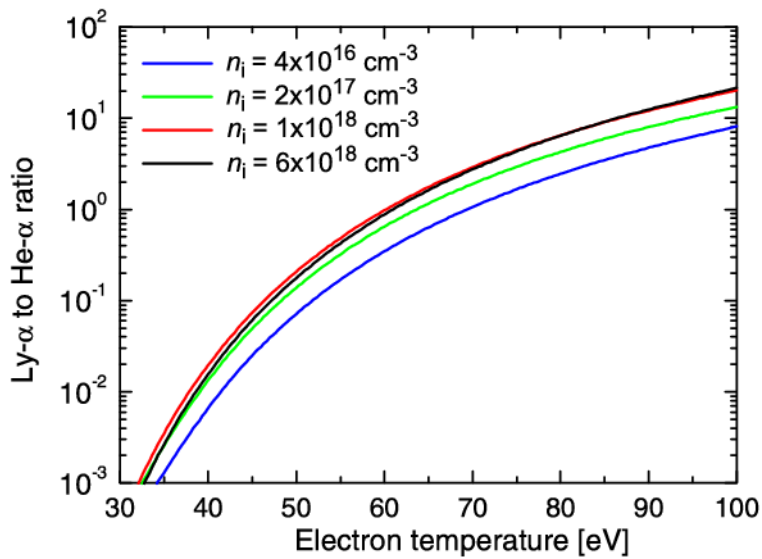


Fig. 4.12: Ratio of Ly- $\alpha$  and He- $\alpha$  lines of carbon ions for optically thin plasma, FLY.

### 4.3.2 Stagnation

At the end of the implosion, a coronal plasma reached a fibre and stagnated at the axis for a brief period of time. This time corresponded to the peak of the short intensive pulse of XUV radiation. This pulse originated predominantly from the corona around a fibre. Sometimes, however, we observed that the signal of Al-filtered PIN diode did not correspond to intensities of K-shell lines of carbon ions. This discrepancy could be explained by the fact that Al-foil absorbs carbon K-shell lines. Hence, the intensity of XUV pulse is determined by L-shell lines of carbon and/or by the amount of impurities.

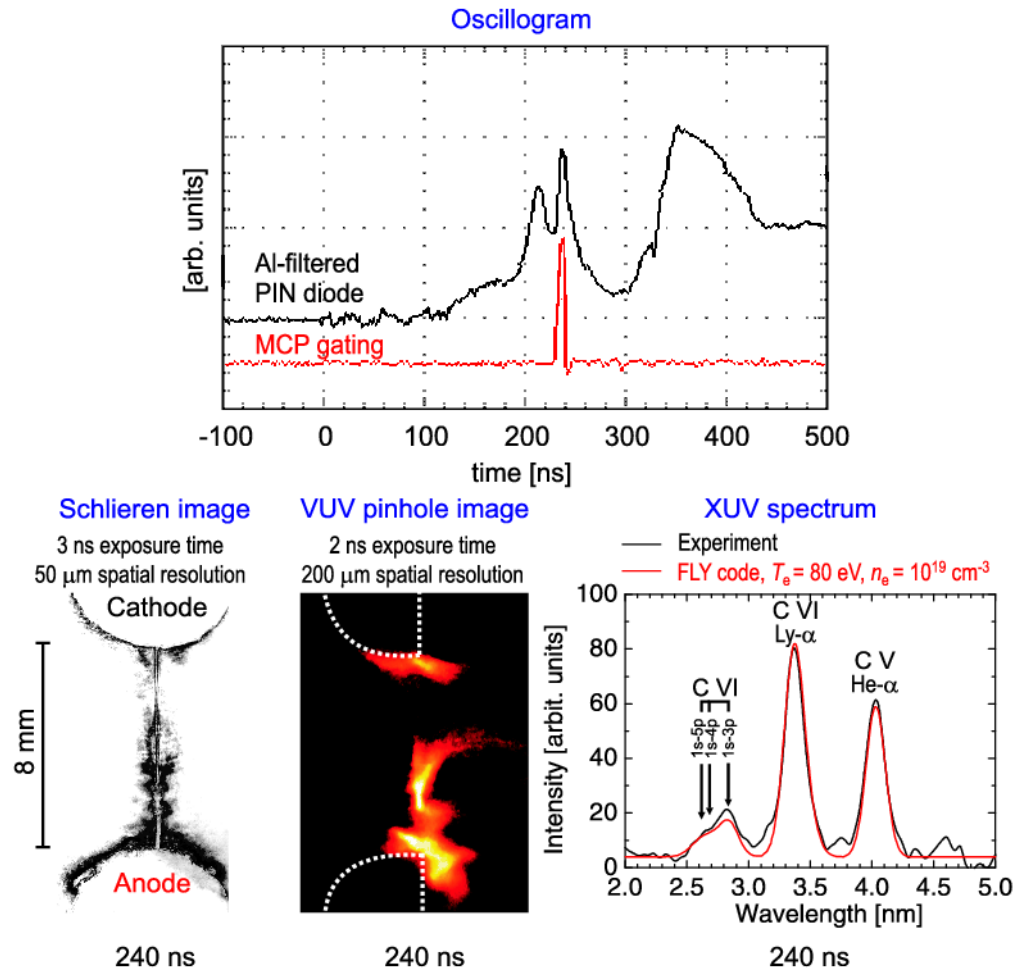


Fig. 4.13: Simultaneous XUV spectrum, schlieren and pinhole images exposed at the peak of the XUV pulse, shot no. 030219-4. A 15  $\mu\text{m}$  diameter and 8 mm long carbon fibre, bisectional electrodes made of brass, 12  $\mu\text{F}$  capacitors, charging voltage of 20 kV, schlieren sensitivity  $n_e \approx 5 \times 10^{18} \text{ cm}^{-3}$ .

The simultaneous diagnostics in Fig. 4.13 demonstrates that the radiation was emitted from that part of a fibre where MHD instabilities were developed. These perturbations

were usually axisymmetric indicating an  $m = 0$  instability. Schlieren images corresponded to pinhole images and thus the schlieren system and pinhole camera gave similar value of perturbation wavelengths  $\lambda$ . In the case of 15  $\mu\text{m}$  carbon fibres, the wavelength  $\lambda$  and pinch radius (or to be more precise, the diameter of instabilities)  $R$  varied from 0.3 to 1 mm and 0.5 to 1.5 mm, respectively. The  $kR$  product, where  $k = 2\pi/\lambda$  is the axial wave number, was  $2 \div 10$  and seemed to increase with the time. However, accurate evaluation was impossible since only a few lobes developed along the fibre. Moreover, the changing wavelength  $\lambda$  showed the presence of a mixture of instabilities (see the schlieren image in Fig. 4.8).

#### Plasma parameters

The graph in Fig. 4.13 shows the experimental and simulated spectrum. The simulated spectrum was calculated by the collisional–radiative code FLY. As far as the input parameters for the steady–state simulation are concerned, the electron temperature  $T_e$  and density  $n_e$  were 80 eV and  $10^{19} \text{ cm}^{-3}$ , respectively. Optical depth effects were taken into account. The estimation of the electron density  $n_e$  was ambiguous owing to its dependence on the choice of the optical path length.

Therefore, plasma density was obtained from schlieren images assuming a parabolic density profile. The highest sensitivity of our schlieren system determined the minimum electron density of  $5 \times 10^{18} \text{ cm}^{-3}$  (see page 70). When we used a larger stop in the schlieren system we observed plasmas with electron densities above  $10^{19} \text{ cm}^{-3}$ . On the basis of our measurements, we assumed that the average electron density during the stagnation was of the order of  $n_e \approx 10^{19} \text{ cm}^{-3}$ . For the average ion charge of 5, we get the ion density of  $n_i \approx 2 \times 10^{18} \text{ cm}^{-3}$  which is two times higher than the density estimated from the implosion velocity (see page 83). It is a reasonable agreement especially if we consider that both methods give only a rough estimation and that the density during the stagnation could be increased by the particles ablated from a fibre.

#### Bennett equilibrium

Assuming the steady–state equilibrium of a  $Z$ –pinch during the stagnation, it is possible to compare our experimental results with the Bennett equilibrium.

During the stagnation the current  $I$  flowing through the pinch was about 40 kA, the temperature  $T$  was about 70 eV. The ionization state was primarily H–like and He–like carbon thus the ion charge  $\bar{z}$  was about 5.5. Then the Bennett equation 2.15 on page 28

gives the ion line density  $N_i = 10^{18} \text{ m}^{-1}$ . This value is of the order of the density determined from the implosion velocity (see page 83).

### 4.3.3 Expansion

The stagnation lasted from a several nanoseconds to a few tens of nanoseconds. After the stagnation we observed the expansion of a plasma column. The rapid expansion was inferred from the schlieren images. For instance in Fig. 4.14, the density of a plasma column was below the sensitivity of the schlieren system already 20 ns after the peak of XUV radiation. To determine the expansion velocity was somewhat problematic because of the drop of plasma density and emitted power. However, it was clear that the expansion velocity was high enough to cause the rapid increase of  $dI/dt$ . The expansion was accompanied by the gradual cooling. In Fig. 4.14, the Ly- $\alpha$  to He- $\alpha$  ratio fell down during 10 ns. According to Fig. 4.12, the temperature dropped from 60 eV to less than 45 eV.

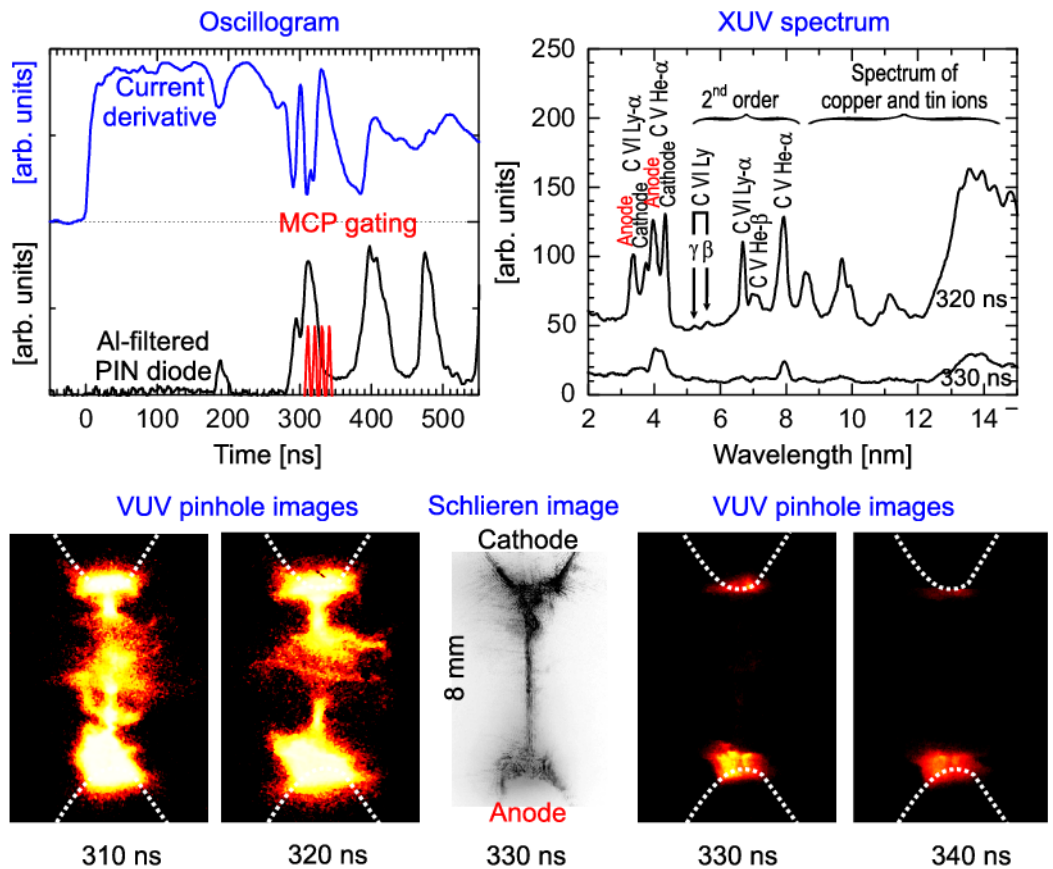


Fig. 4.14: Cooling after the stagnation in discharge no. 040225-2. A 15  $\mu\text{m}$  diameter and 8 mm long carbon fibre, conical electrodes made of bronze, 3  $\mu\text{F}$  capacitor, 20 kV charging voltage, schlieren sensitivity  $n_e \approx 10^{19} \text{ cm}^{-3}$ .

During or after the expansion, we sometimes observed cold and dense plasma regions. For example, Fig. 4.15(a) shows the expanded dense core of a fibre 10 ns after the series of short XUV pulses.

(a) Expanded dense core at 275 ns, it occurred 10 ns after the peak of 10 ns pulse in discharge no. 030409-4.

(b) Schlieren image of the helix observed at 300 ns, it occurred 50 ns after the peak of XUV pulse in the discharge no. 030410-2.

*Fig. 4.15:* A 15  $\mu\text{m}$  diameter and 8 mm long carbon fibre, bisectional electrodes made of steel, 3  $\mu\text{F}$  capacitor, 25 kV charging voltage, schlieren sensitivity  $n_e \approx 5 \times 10^{18} \text{ cm}^{-3}$ .

Once or twice we also observed the helix after the expansion. Fig. 4.15(b) was recorded 50 ns after the XUV pulse. At this time the plasma was expanded to a radius of several millimetres, whereas the diameter of helix was about 50  $\mu\text{m}$ . This begs the question of what kept this cold structure in existence.

#### 4.3.4 Multiple pulses

Fig. 4.6 shows a high number of pulses that were detected by a PIN diode. The intensity of pulses was increasing with the growing time most likely because of the rising current. It was necessary to decide whether pulses originated from various places along a fibre or from the whole length of a fibre at different moments.

We believe that both phenomena might occur. During the rise of the current it was possible that the multiple implosion of the corona onto a fibre took place. However, when there were more than two pulses, they did not originate from the whole length of a fibre. Especially in the case of conical electrodes, the non-symmetric implosion occurred separately at the anode, at the cathode, and at the centre (cf. Fig. 4.14). As a result, we observed higher number of pulses than in the case of flat electrodes.

### 4.3.5 Experimental data interpretation

#### Gradual fall of current derivative and rise of voltage

First observation which needs to be interpreted is the gradual fall of circuit  $dI/dt$  and the rise of voltage before each XUV pulse (see Fig. 4.6).

The starting point of our explanation is Fig. 3.6 on page 40. According to it we can express

$$U(t) = U_0 - \int_0^t \frac{I(t')}{C_0} dt' = \frac{d}{dt} \left( (L_0 + L_p)I \right) + (R_0 + R_p)I \quad (4.1)$$

$$\frac{dI}{dt} = \frac{U - (R_0 + R_p + \dot{L}_p)I}{L_0 + L_p} \quad (4.2)$$

where  $C_0$ ,  $L_0$ ,  $R_0$  are parameters of a short circuit and  $L_p$ ,  $R_p$  stand for the inductance and resistance of a pinch plasma, respectively. On the one hand, the inductance of the pinching plasma ( $L_p < 10$  nH) was lower than the inductance of the rest of circuit ( $L_0 \approx 100$  nH) and, in addition to that, the inductance depends on the pinch radius only logarithmically. Therefore, it did not affect the current derivative to an excessive degree. On the other hand, because of a low resistance of the current generator ( $R_0 = 25$  m $\Omega$ ), the current waveform was very sensitive to the plasma resistance  $R_p(t)$  and to the change of inductance  $\dot{L}_p(t)$ . That is why the observed fall of  $dI/dt$  can be attributed to the rise of the impedance  $(R_p + \dot{L}_p)$  during the implosion and stagnation. The increase of  $(R_p + \dot{L}_p)$  also caused the voltage growth since

$$U_p = \frac{d}{dt} (L_p I) + R_p I = L_p \frac{dI}{dt} + \left( \frac{dL_p}{dt} + R_p \right) I \quad (4.3)$$

In order to obtain quantitative results, we simulated the  $R-L-C$  circuit with a time-dependent  $R_p + \dot{L}_p$  term (see appendix D). An example of our simulation is shown in Fig. 4.16 where the experimentally observed waveforms are presented together with MATLAB simulation. Fig. 4.16 shows that the observed waveforms in the period between 250 ns and 300 ns could be explained by the rise of the  $R_p + \dot{L}_p$  term up to 0.25  $\Omega$  and by its subsequent drop to -0.05  $\Omega$ . An inevitable question is what part of this value could be attributed to the resistance  $R_p$  and what part belongs to the change of the inductance  $\dot{L}_p$ ?

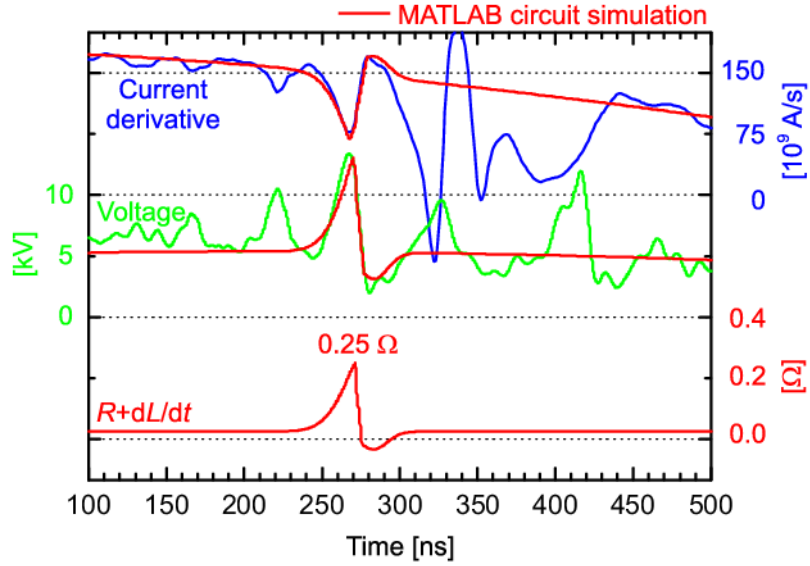


Fig. 4.16: Experiment vs. MATLAB simulation of the  $R$ – $L$ – $C$  circuit, shot no. 050128-1. A carbon fibre of 15  $\mu\text{m}$  diameter and 8 mm length, conical electrodes made of brass, 3  $\mu\text{F}$  capacitor, 20 kV charging voltage.

#### Resistance versus time–varying inductance

To solve this question we present the following calculation assuming the current flowing through a cylindrically symmetric  $Z$ –pinch<sup>11</sup>.

We can express  $R_P$  and  $L_P$  as

$$R_P = \frac{l}{\pi R^2 \sigma} \quad (4.4)$$

$$L_P = \frac{\mu l}{2\pi} \ln \frac{b}{R} \quad (4.5)$$

where  $l$ ,  $R$ ,  $\sigma$  stand for the length, radius, and conductivity of a plasma column, respectively. The quantity  $b$  represents the radius of the experimental chamber.

Calculating the derivative

$$|\dot{L}_P| = \frac{\mu l v_{\text{imp}}}{2\pi R} \quad (4.6)$$

we obtain the ratio

$$\frac{|\dot{L}_P|}{R_P} = \frac{1}{2} \mu \sigma R v_{\text{imp}} \quad (4.7)$$

<sup>11</sup> We assume the uniform current density since the skin depth is of the order of millimetres.

For quantities observed during the implosion

$$R = 2 \text{ mm}, \quad v_{\text{imp}} = 10^5 \text{ m s}^{-1}, \quad T_e = 40 \text{ eV}, \quad \bar{z} = 5, \quad \ln \Lambda \doteq 10$$

$$\sigma_{\text{Spitzer}} \doteq 7.7 \times 10^{-3} T^{3/2} / (\bar{z} \ln \Lambda) \doteq 5 \times 10^4 \text{ S m}^{-1} \quad (4.8)$$

the ratio in question is

$$\frac{\dot{L}_P}{R_P} \doteq 6 \quad (4.9)$$

This led us to conclusion that during the implosion the energy was coupled from the generator through a time-varying inductance. The electrical energy was mainly converted (i) into the radial motion of ions, (ii) into the (adiabatic) compression of a plasma column and (iii) into the increase of magnetic energy<sup>12</sup>. Shock heating of ions might also occur, however, we have not observed any shock-wave during the implosion of a coronal plasma onto a fibre.

Late in the implosion, as the radius  $R$  and velocity  $v_{\text{imp}}$  were decreasing, the influence of plasma resistance was growing and the resistive heating started to play an important role. Speaking quantitatively, for values in Eq. 4.8 and for  $l = 3 \text{ mm}$  (a part of a fibre participating in the implosion when conical electrodes were used), we obtain a time-varying inductance

$$\dot{L}_P = 0.03 \text{ } \Omega \quad (4.10)$$

which is lower than  $0.25 \text{ } \Omega$ .

As regards the plasma resistance, for reasonably estimated values during the stagnation

$$R = 0.5 \text{ mm}, \quad l = 3 \text{ mm}, \quad T_e = 70 \text{ eV}, \quad \bar{z} \ln \Lambda \doteq 60, \quad \sigma_{\text{Spitzer}} \doteq 10^5 \text{ S m}^{-1} \quad (4.11)$$

we get

$$R_P \doteq 0.04 \text{ } \Omega \quad (4.12)$$

Such value is also lower than  $0.25 \text{ } \Omega$ . In order to reach  $0.25 \text{ } \Omega$ , we can naturally reduce the radius of a plasma column. However, the effect of instabilities seems to be more sensible explanation.

<sup>12</sup> From  $\int_{t_0}^t U_P I dt = \int_{t_0}^t R_P I^2 dt + \int_{t_0}^t \dot{L}_P I^2 dt + \int_{t_0}^t L_P \dot{I} I dt = \int_{t_0}^t R_P I^2 dt + \frac{1}{2} \int_{t_0}^t \dot{L}_P I^2 dt + \frac{1}{2} \int_{t_0}^t \dot{L}_P I^2 dt + \frac{1}{2} \int_{t_0}^t L_P (dI^2/dt) dt = \int_{t_0}^t R_P I^2 dt + \frac{1}{2} \int_{t_0}^t \dot{L}_P I^2 dt + [L_P I^2]_{t_0}^t$  follows that the energy  $\int_{t_0}^t (R_P + \frac{1}{2} \dot{L}_P) I^2 dt$  is fed into the plasma and  $[L_P I^2]_{t_0}^t$  goes into the rise of magnetic field.

### Plasma instabilities

The substantial contribution to plasma column resistance during the stagnation could be ascribed to instabilities. The strong argument for that are voltage spikes which corresponded to XUV pulses. At the same time, these XUV pulses did not originate from the whole length of a fibre but from several bright spots. These bright spots corresponded to the interaction of the necks of an  $m = 0$  instability with the dense core (cf. Fig. 4.17).

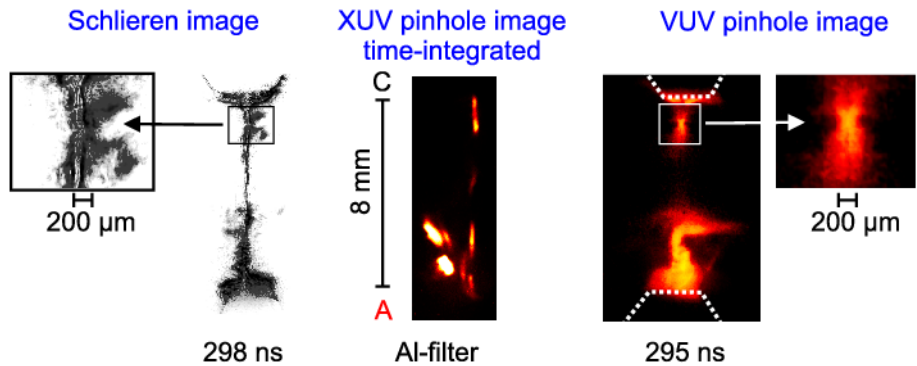


Fig. 4.17: Observed  $m = 0$  instability in shot no. 040421-1. Off-axis bright spots originated from the later stage of a discharge. A 15  $\mu\text{m}$  diameter and 8 mm long carbon fibre, conical electrodes made of brass, 20 kV charging voltage.

For values observed in Fig. 4.17

$$R = 0.1 \text{ mm}, \quad l = 0.3 \text{ mm}, \quad T_e = 70 \text{ eV}, \quad \bar{z} \ln \Lambda \doteq 60, \quad \sigma_{\text{Spitzer}} \doteq 10^5 \text{ S m}^{-1} \quad (4.13)$$

we obtain the plasma resistance

$$R_P \doteq 0.1 \text{ } \Omega \quad (4.14)$$

If we consider both the wide plasma column and several necks of  $m = 0$  instability, the total plasma resistance during the stagnation could achieve 0.25  $\Omega$ .

However, these values represent only rough estimations since the radius of a plasma channel was limited by the spatial resolution of the order of 100  $\mu\text{m}$ . Moreover, we do not know where exactly the current was flowing and what was the role of anomalous resistivity within instabilities.

We must not also forget that instabilities contribute not only to plasma resistance but also to the  $\dot{L}_P$  term. An  $m = 0$  instability develops with the Alfvén velocity of  $10^5 \text{ m s}^{-1}$  and thus according to values in Eq. 4.13

$$\dot{L}_P = \frac{\mu I v_A}{2\pi R} \doteq 0.05 \Omega \quad (4.15)$$

The power  $\frac{1}{2}\dot{L}_P I^2$  is then transferred to ions.

As regards an  $m = 1$  instability, its contribution to the  $\dot{L}_P$  term depends on the rate of how fast it develops. We often observed helical structures in pinhole images, whereas in schlieren images they were less apparent. Similar results were observed by Lorenz et al. (1998). The complex helical structures develop usually during an expansion phase after stagnation (cf. Fig. 4.15(b) and Spielman et al., 1994; Spielman and de Groot, 2001). Recently, the influence of an  $m = 1$  instability upon  $Z$ -pinch dynamics has been quantitatively discussed by Chittenden et al. (2004). He found that the plasma is going  $m = 1$  unstable when the Lorentz force starts to compress the stagnated plasma. Then the onset of an  $m = 1$  instability provides an efficient mechanism for dissipation of the magnetic energy surrounding the stagnated pinch. Not only does the formation of a helix allow the magnetic field to do work in driving an expansion but it also enhances the ohmic heating by elongating the current path length<sup>13</sup>.

On the basis of preceding paragraphs we can conclude that it is not easy to unambiguously determine what contributed to the  $R_P + \dot{L}_P$  term. Nevertheless, we can say that a time-varying inductance was important during the implosion, whereas at the stagnation the influence of plasma instabilities and resistive heating seemed to be the dominant one.

#### *Energetics during plasma - on - fibre stage*

The previous paragraphs clarified rises of voltage. During these spikes, the energy from the current generator was fed into a plasma. The excess of energy was almost immediately (within 5 ns) radiated and this is why we observed XUV pulses. Since we measured the current and voltage, it was possible to estimate the energetics of our  $Z$ -pinch. We could calculate the ohmic heating and the kinetic energy delivered to ions in the period

<sup>13</sup> The energy conservation in wire-array  $Z$ -pinches has become a debated issue because radiated energies could be more than 3÷4 times greater than the ion kinetic energy from the implosion. Already 20 years ago, however, Riordan et al. (1981) pointed out that the observed radiation yield was significantly higher than the kinetic energy input. Besides anomalous resistivity in the trailing mass (Peterson et al., 1998), the obvious extra energy source available is the magnetic energy that is much greater than the kinetic energy of implosion. The magnetic energy could be dissipated by instabilities through the  $\dot{L}_P$  term. Rudakov and Sudan (1997); Rudakov et al. (2000) and Velikovich et al. (2000) proposed the model of current reconnections around an  $m = 0$  instability and subsequent collapse of toroidal magnetic flux tubes. Haines et al. (2004) considered fine-scale instabilities and viscous heating of ions to play the major role. Nevertheless, a lot of plasma physicists see  $m = 1$  behaviour in the current flow to be the most likely explanation of a “paradox” heating in question (cf. Kubeš et al., 2002; Chittenden et al., 2004).

between 250 ns and 300 ns (cf. Fig. 4.16). We shall start with the kinetic energy first.

The total kinetic energy delivered to the axis could be estimated from a time-varying inductance as follows:

$$W_{\text{imp}} = \int_{t_0}^t \frac{1}{2} \dot{L}_P I^2 dt \approx \frac{1}{2} I^2 \int_{t_0}^t \dot{L}_P dt = \frac{1}{2} [L_P(t) - L_P(t_0)] I^2 \quad (4.16)$$

According to Eq. 4.5 we have

$$W_{\text{imp}} = \frac{\mu l}{4\pi} \ln\left(\frac{R(t_0)}{R(t)}\right) I^2 \quad (4.17)$$

Using

$$I = 35 \text{ kA}, \quad l = 3 \text{ mm}, \quad \frac{R(t_0)}{R(t)} \doteq 10 \quad (4.18)$$

the result is

$$W_{\text{imp}} = 1.5 \text{ J} \quad (4.19)$$

Even more energy seemed to be delivered by collisional processes during the stagnation phase. Moving to the ohmic heating, using values discussed above, it can be estimated as

$$\int_0^t R_P I^2 dt \approx R_P|_{\text{max}} I^2 \cdot t_{\text{FWHM}} \doteq 0.2 \cdot (35 \times 10^3)^2 \cdot 15 \times 10^{-9} \text{ J} \doteq 3.5 \text{ J} \quad (4.20)$$

The overall energy deposited to the plasma during one XUV pulse was thus about 5 J. This energy was used for ablating of a central fibre, ionization<sup>14</sup> and heating of a plasma. Another part of the input energy was spent by advection, thermal diffusion of a plasma, plasma expansion, etc. The radiated energy (100 mJ in the XUV region, see page 81) represented only a small fraction of the overall deposited energy.

### Expansion velocity

Another value that can be evaluated from Fig. 4.16 is the expansion velocity. Because the  $R_P + \dot{L}_P$  term fell to  $-0.05 \Omega$ , the change of inductance was higher than  $0.05 \Omega$ . From Eq. 4.6 and for  $l = 3 \text{ mm}$ ,  $R = 500 \mu\text{m}$  (cf. Fig. 4.14), we obtain the expansion velocity  $v_{\text{exp}}$  above  $4 \times 10^4 \text{ m s}^{-1}$ .

<sup>14</sup> The energy of 4.5 J is needed for the whole fibre ionised to the He-like stage, whereas 30 J are necessary for the ionization to bare nuclei.

#### 4.4 Fibre Ablation

Approximately 500 ns after the breakdown, gaps in the fibre indicated that several parts of a fibre had been already ablated, especially the part near the anode. In Fig. 4.18, one can see the  $m = 0$  behaviour which most likely increased the ablation rate. In the case of conical electrodes, the central part of a fibre persisted up to 700 ns and then formed a dense and cold plasma “island”. The entire length of a fibre was seen totally ablated 750 ns after the current breakdown. After that, the radiation was still detected with the Al- and Be-filtered PIN diodes.

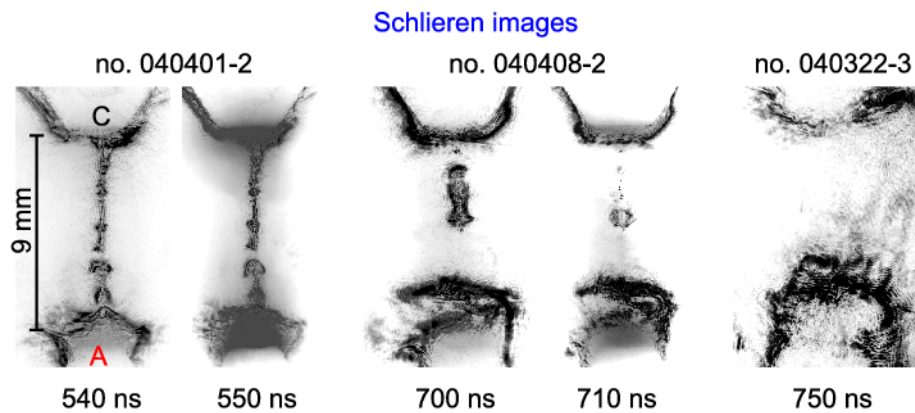


Fig. 4.18: Schlieren images that recorded the ablation of a fibre. A 15  $\mu\text{m}$  diameter and 9 mm long carbon fibre, conical electrodes made of brass, 20 kV charging voltage.

Something like a shock-wave was seen near the anode in shot no. 040408-2 in figure 4.18. The following figure 4.19 shows a radiating, sharp density gradient that was propagating from the cathode.

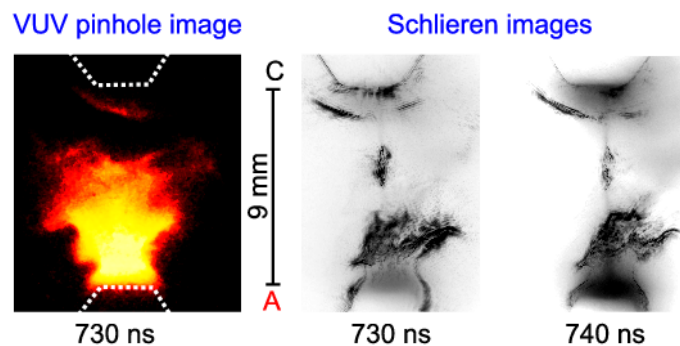


Fig. 4.19: Sharp density gradient near the cathode in shot no. 040408-1. A 15  $\mu\text{m}$  diameter and 9 mm long carbon fibre, conical electrodes made of brass, 20 kV charging voltage.

## 4.5 Discharge in Electrode Vapour

Fig. 4.20 shows typical waveforms of the current derivative  $dI/dt$ , voltage, PIN diode signals and PMT signal between 400 and 1000 ns.

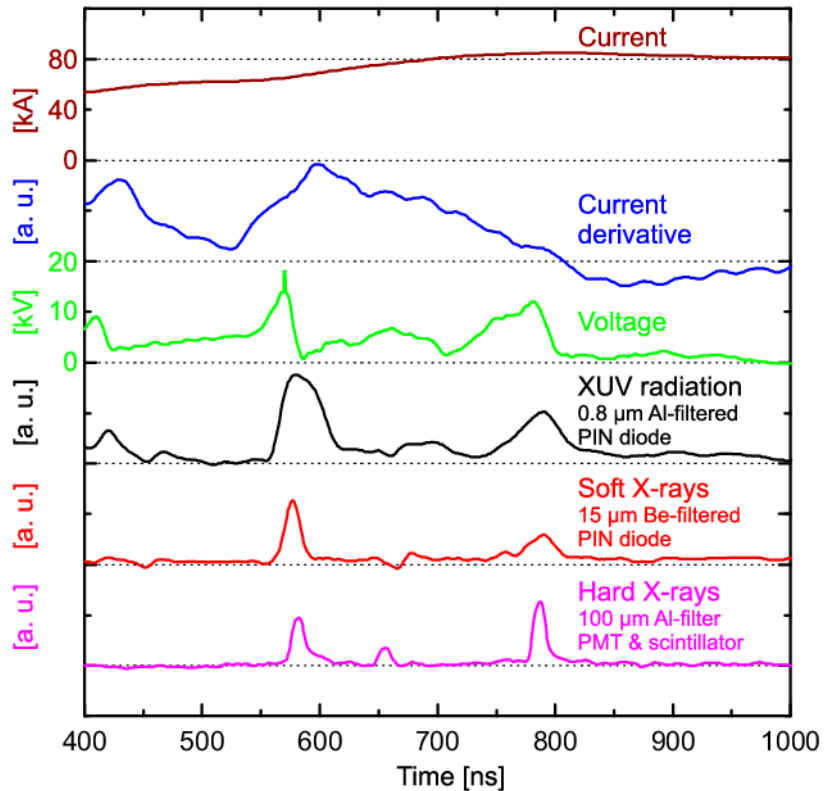


Fig. 4.20: Discharge in electrode vapour, shot no. 050201-3. A 15  $\mu\text{m}$  diameter and 8 mm long carbon fibre, conical electrodes made of brass, 20 kV charging voltage.

In this phase, emitted pulses with various FWHMs were accompanied with rises of voltage<sup>15</sup> up to 30 kV (similarly to the plasma – on – fibre phase). However, in comparison with the first 500 ns of the discharge, these pulses were more energetic. The energy of  $> 1$  keV photons exceeded 10 mJ in one pulse and the abundance of  $> 6$  keV photons was detected behind a 100  $\mu\text{m}$  thick Al filter<sup>16</sup>. This fact brought us naturally to the question of what led to the emission of X-ray pulses. It was evident that the important role was played by the material of electrodes. The following subsections shall add to the

<sup>15</sup> We expect that the electrode vapour spread over a significant part of the chamber. This could reduce the current flowing through the Rogowski coil and consequently stop the sensitive detection of fast changes of a plasma impedance. As a result, the coincidence between an X-ray pulse and a dip in  $dI/dt$  disappeared after 400 ns.

<sup>16</sup> We detected radiation filtered also with a 750  $\mu\text{m}$  thick Al foil. Thus the energy of several photons was higher than 10 keV (see Fig. 3.16).

explanation of that.

#### 4.5.1 Evaporation of material from electrodes

The emission from the electrodes as well as the expansion of the electrode vapour were apparent early in the discharge (see Fig. 4.4 and 4.21). With the growing time the influence of material from electrodes was increasing. The observed velocity of evaporated materials from electrodes approached  $10^4 \text{ m s}^{-1}$ , therefore the discharge occurred more or less in the vapour of electrodes later than 400 ns after the current breakdown. This expectation was proven experimentally when we observed that spectral lines of copper and tin ions started to dominate in XUV spectra after 500 ns (cf. Fig. 4.22). By the way, the peak of tin ions at 13.5 nm has become important for EUV lithography.

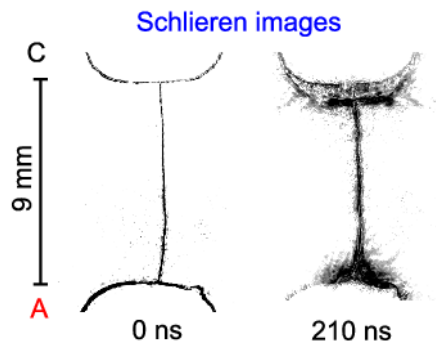


Fig. 4.21: Material evaporated from electrodes, shot no. 021024-2. A 15  $\mu\text{m}$  diameter and 9 mm long carbon fibre, bisectional electrodes made of brass, 20 kV charging voltage.

#### 4.5.2 Magnetic pinching of evaporated material

Fig. 4.22 displays the off-axis implosion of electrode material near the anode. The implosion velocity was about  $3 \times 10^4 \text{ m s}^{-1}$ . At about 560 ns, i.e. at the time when we could expect the end of the implosion, an X-ray pulse was generated. Schlieren images indicated that more mass participated in the implosion. The electron line density above  $10^{20} \text{ m}^{-1}$  was two orders of magnitude higher than in the plasma – on – fibre phase.

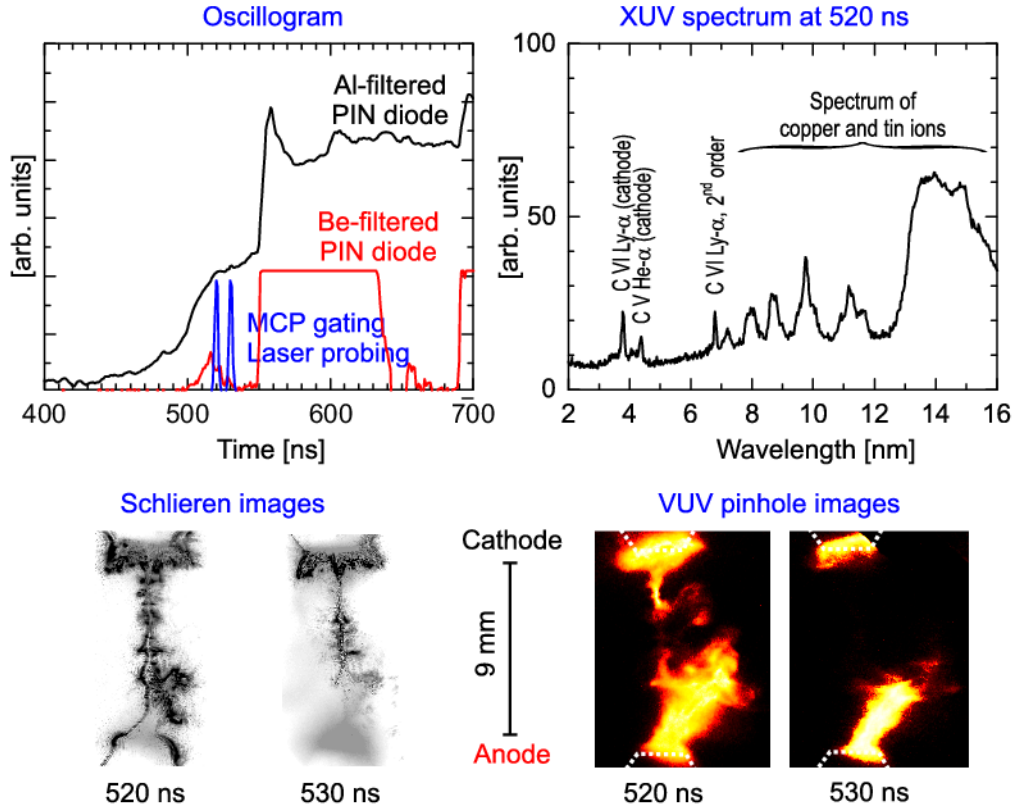


Fig. 4.22: Implosion of material evaporated from electrodes, shot no. 040402-1. A 15  $\mu\text{m}$  diameter and 9 mm long carbon fibre, conical electrodes made of bronze, 20 kV charging voltage.

#### 4.5.3 Development of plasma instabilities

The final stage of the implosion was detected in shot no. 040414-2 (see Fig. 4.23). In this particular shot, images were obtained just before and during the X-ray pulse of a 2 ns rise time. The schlieren and pinhole images caught the development of the  $m = 0$  instability with three “blobs”. Furthermore, the most intensive radiation (as could be seen in the time-integrated pinhole images) came from one off-axis elongated bright spot which corresponded to the constriction of one  $m = 0$  neck. These bright spots occurred mainly near the anode and their number was shot-to-shot dependent.

At this point we shall turn to the plasma-on-fibre stage. In Fig. 4.23, the entire length of a carbon fibre is displayed in the time-integrated Al-filtered pinhole image. The radiation from a fibre was absorbed by the Be-filter. Such result agrees with the observation of XUV pulses (and no X-ray pulses) during the plasma-on-fibre phase. Next, the spatially non-uniform exposure along the fibre gave another evidence that the radiation came from that part of a fibre where an  $m = 0$  instability developed (cf. page 93).

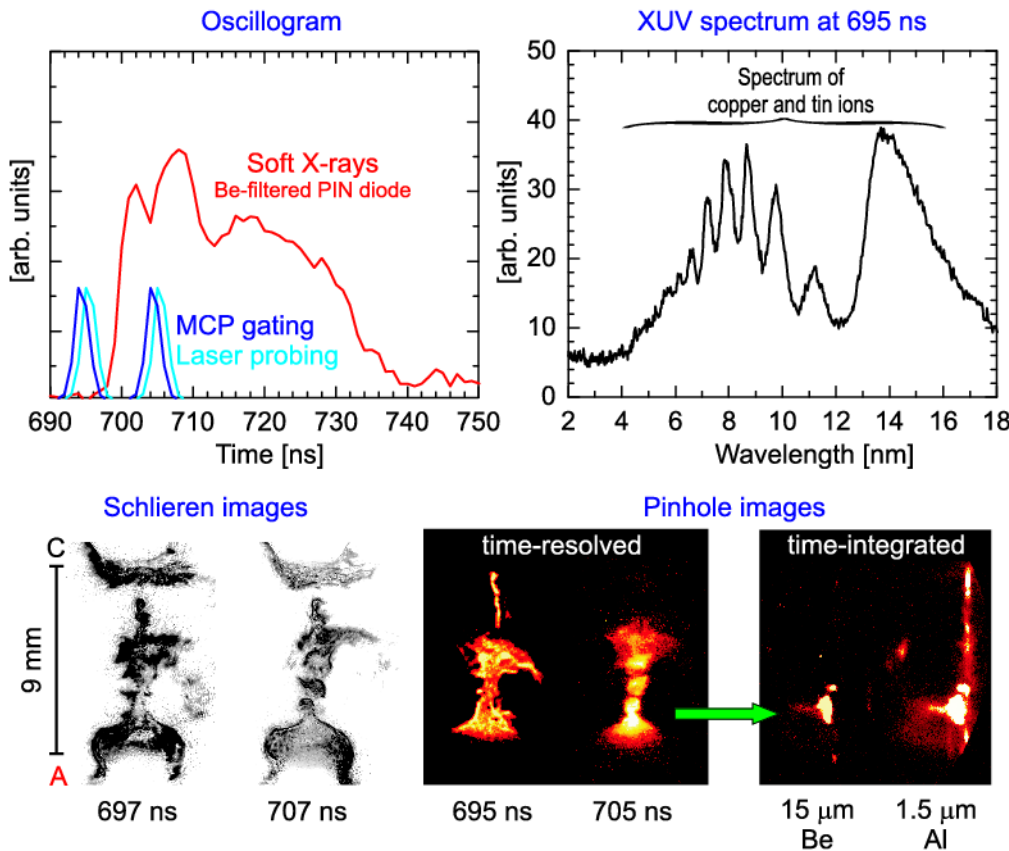


Fig. 4.23: Z-pinch plasma during the onset of an intensive X-ray pulse, shot no. 040414-3. A carbon fibre of 15  $\mu\text{m}$  diameter and 9 mm length, conical electrodes made of bronze, 20 kV charging voltage.

#### Temperature of bright spots

The plasma parameters within bright spots has not been explored in detail. The density of the bright spot displayed in Fig. 4.23 can be only guessed. As far as the temperature is concerned, the X-ray pinhole camera and photomultiplier signal evidently demonstrated that more energetic photons were emitted whenever bright spots were observed. Nevertheless, these photons could be produced by “non-Maxwellian” electrons accelerated in high electric field<sup>17</sup>, whereas the plasma temperature could be low. The only thing which can be used is the temperature estimated from an XUV spectrum.

Fig. 4.24 presents the time-integrated spectrum in the 2 – 15 nm region. In this spectrum, the first order of carbon K-shell lines did not lie on the Rowland circle and therefore the Ly- $\alpha$  and He- $\alpha$  lines of carbon ions were defocused. This large defocusing indicates that these K-shell lines originated from an extensive source. To be more specific, al-

<sup>17</sup> The plasma voltage was up to 30 kV. The peak voltage could exceed the charging voltage of 20 kV because the large inductance of the driver  $L_0$  kept current flowing through a plasma when the plasma resistance rapidly increased.

though the spectral lines in question were emitted from the entire length of a fibre, it is particularly true for the region near the anode. Contrary to these spectral lines, the line at about 4.7 nm was relatively narrow and therefore it must have originated from a smaller region. This spectral line was identified as the transition  $3d\ ^2D - 4f\ ^2F$  of a Na-like copper ion Cu IXX at 4.74 nm. It means that the Na-like stage of copper occurred in a plasma and thus<sup>18</sup> the temperature was well above 100 eV. The peak temperature could be of course even higher.

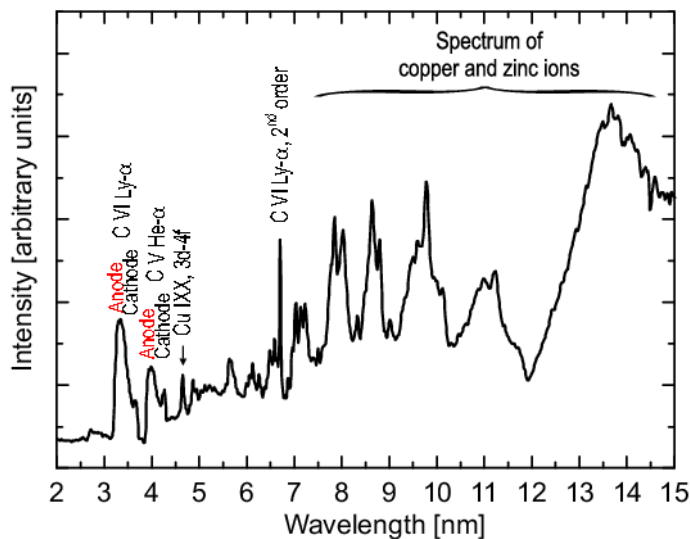


Fig. 4.24: Time-integrated XUV spectrum, shot no. 050427-2. A carbon fibre of 15  $\mu\text{m}$  diameter and 9 mm length, conical electrodes made of brass, 20 kV charging voltage.

#### 4.5.4 Experimental data interpretation

Now, we shall discuss occurrence of X-ray pulses accompanied with rises of voltage. It could be done similarly to the interpretation of the plasma – on – fibre stage.

The peak current at this phase was about 80 kA, therefore the increase of voltage above 20 kV leads to the  $R_p + \dot{L}_p$  term of about  $0.3 \Omega$ . We believe that such value was achieved within plasma instabilities that were also presumably sources of energetic photons. These X-ray photons were generated for several reasons. Firstly, instabilities could develop substantially because the fibre had been already ablated<sup>19</sup>. Secondly, the current at this phase was higher than in the plasma – on – fibre stage. Thirdly, the plasma contained ions with higher atomic number  $Z$  than carbon has. As a result, not only continuum emission but also line radiation occurred in the X-ray region.

<sup>18</sup> According to Eq. A.29 on page 147 the temperature was estimated from Cu XVIII ionization energy of about 650 eV (Attwood, 1999).

<sup>19</sup> This was also the reason for off-axis implosion.

## 4.6 *Z*–pinch Disintegration

The disintegration of the *Z*–pinch occurred at about 1  $\mu$ s. At that time, discharge chamber walls were most likely reached by ejecta of a plasma. Also, X–ray and UV flux emitted from a *Z*–pinch could envelop the surface of the insulator with a plasma. Due to that, the significant part of the current was flowing outside the “*Z*–pinch region” and the decreasing amount of radiation was detected (see Fig. 4.25).

## 4.7 *Energetics of Z*–pinch

The previous sections have described individual phases of our *Z*–pinch, from the breakdown to its disintegration. In this section we shall deal with the overall energetics of our fibre *Z*–pinch. After that we will discuss the influence of the electrodes and finally we will conclude this chapter by saying a few words about differences between fibres of various diameters.

The measurement of plasma voltage and current enabled us to estimate the energy deposited into our *Z*–pinch. The deposited energy was spent on the ablation/evaporation of a fibre/electrodes, ionization and heating of a plasma, thermal diffusion, advection, etc. Only a small part of the deposited energy was radiated from the plasma. The overall energetics of our fibre *Z*–pinch is summarised in Tab. 4.1.

Physical quantity	Energy
Energy stored in a capacitor bank $\frac{1}{2}C_0U_0^2$	600 J ( $U_0 = 20$ kV)
Energy deposited into a plasma $\int_0^\infty (U_P - L_P \dot{I})I dt$	50 $\div$ 100 J
Energy required for the atomization of a fibre	200 mJ
Energy required for the fibre ionization to the He–like stage	4.5 J
Energy required for the fibre ionization to bare nuclei	30 J
Emitted energy	$\approx 5$ J
Energy emitted in the XUV region (30–70 eV)	$\approx 300$ mJ
Energy emitted in soft X–rays ( $> 1$ keV)	$\approx 20$ mJ

Tab. 4.1: Energetics of our fibre *Z*–pinch.

The total emitted energy was estimated from the PIN diode used with a 200  $\mu$ m pinhole, which was this time used instead of a filter (see the blue line in Fig. 3.15). The results from shot no. 050512-1 are presented in Fig. 4.25.

It shows that most of the energy was radiated in less energetic photons during the long-lasting emission. This emission was increasing with the rising current and was not so sensitive to the fast changes in Z-pinch dynamics as XUV pulses were. Surprisingly, this long-lasting emission overlapped XUV and X-ray pulses which one could expect to be more apparent.

As regards places of the long-lasting emission origin<sup>20</sup>, they are displayed in the Fig. 4.26. Clearly, low energy photons were emitted mainly from regions near electrodes, whereas XUV photons originated from a fibre.

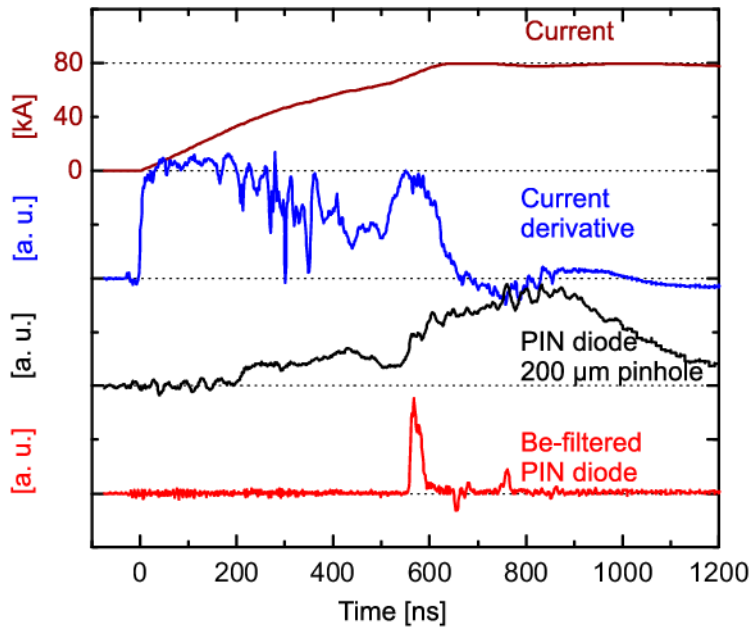


Fig. 4.25: PIN diode signal (200  $\mu\text{m}$  pinhole used instead of a filter) together with the current waveform and signal of a Be-filtered PIN diode, shot no. 050512-1. A 15  $\mu\text{m}$  diameter and 9 mm long carbon fibre, conical electrodes made of brass, 20 kV charging voltage.

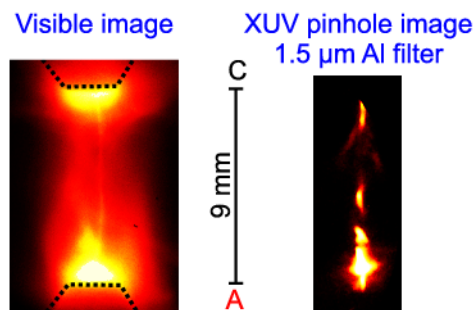


Fig. 4.26: Time-integrated visible and X-ray images, shot no. 040422-1. A 15  $\mu\text{m}$  diameter and 9 mm long carbon fibre, conical electrodes made of bronze, 20 kV charging voltage.

<sup>20</sup> Time-integrated visible images were recorded by the schlieren system when the Nd:YAG laser did not start up.

## 4.8 Influence of Electrodes

Describing our fibre Z-pinch, it is impossible to leave out the influence of electrodes on the plasma dynamics. For instance, Fig. 4.27 shows PIN diode signals for various electrodes. One can see how the number, intensities, and widths of XUV pulses changed with the choice of electrodes. In this section we present the influence of material and shape of electrodes.

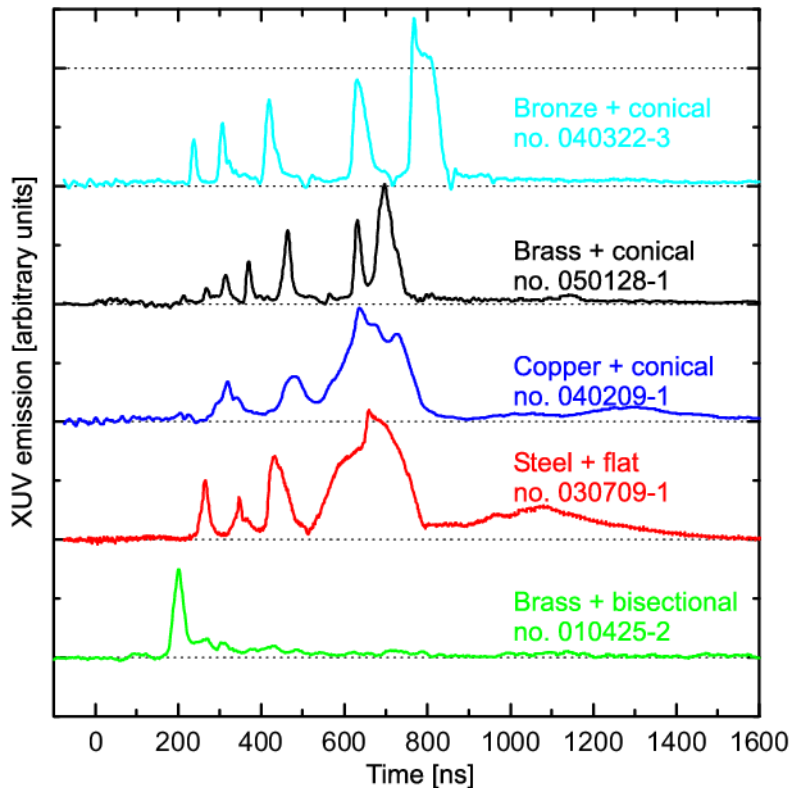


Fig. 4.27: Al filtered PIN diode signals for different materials and shapes of electrodes.

As far as the choice of the electrode material is concerned, it influenced mainly emission spectra. The difference between two XUV spectra in the case of brass and stainless steel electrodes is shown in Fig. 4.28. In the 10–24 nm spectral region the spectral lines of Li- and Be-like oxygen ions were dominant. The intensities of O VI lines corresponded to the Boltzmann distribution of excited states. The appropriate “integral” electron temperature was 15 eV (cf. Fig. 4.28 and Eq. A.30 on page 148). The lines of H- and He-like carbon ions were also present. Some of the lines corresponded to higher-Z ions. In the case of brass electrodes, the characteristic feature was continuum-like radiation between 12 and 18 nm. After replacing brass electrodes by stainless steel ones, the continuum in

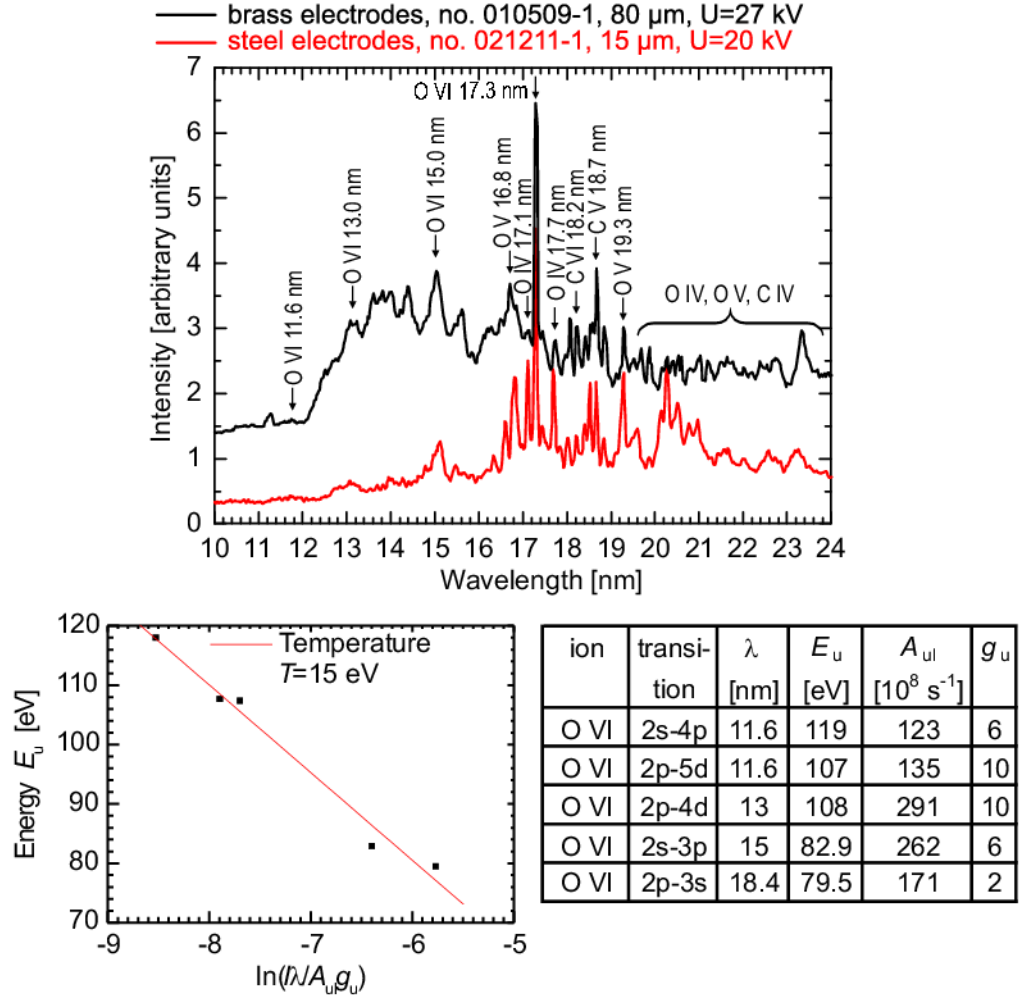


Fig. 4.28: Comparison of two time-integrated XUV spectra when brass and steel electrodes were used. Temperature estimated from spectral lines of O VI ions in shot. no 021211-1.

question disappeared. Hence, the material of electrodes determined (i) the spectral region where the emission occurred and consequently (ii) intensities and widths of XUV pulses. We did not, however, observed any significant change of gross Z-pinch dynamics with the choice of electrode material. It was rather the shape of electrodes what seemed to affect deeply the discharge.

The shape of electrodes determined not only intensities, widths and number of XUV pulses but it also influenced the zipper effect, fibre ablation, X-ray emission, etc. We found out, for example, that a fibre was not fully ablated and there were no X-ray pulses observed in the case of “bisectional” electrodes. The reason for that could be the non-symmetry of the electrodes that caused the early deflection of a coronal plasma from a fibre to chamber walls (cf. Fig. 4.29).

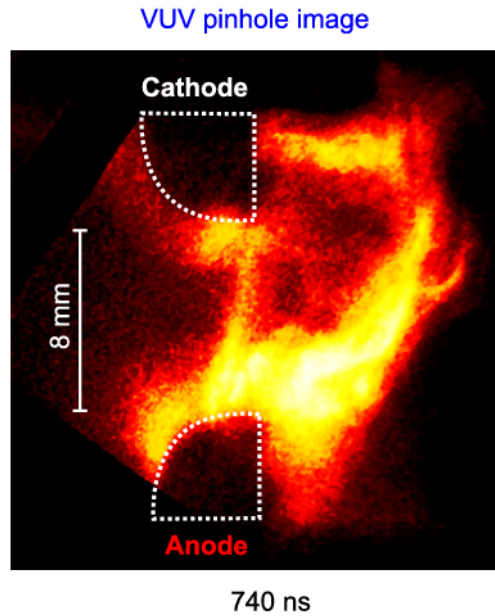


Fig. 4.29: VUV pinhole image in the discharge with bisectional electrodes made of stainless steel, shot no. 030331-3. A 15  $\mu\text{m}$  diameter and 8 mm long carbon fibre, 25 kV charging voltage.

In the case of conical electrodes, a fibre was ablated and X-ray pulses were observed. Nevertheless, as it has been mentioned above, the non-symmetric implosion occurred separately at the anode, at the cathode, and at the centre, and thus a higher number of pulses was observed.

#### 4.9 Various Fibre Diameters

Most of our results presented above came from experiments that were carried out with carbon fibres of a 15  $\mu\text{m}$  diameter. Similar results<sup>21</sup> were observed also with 6  $\mu\text{m}$  and 80  $\mu\text{m}$  diameter fibres. As regards differences between fibres, the discharge with a 6  $\mu\text{m}$  diameter fibre was quite irreproducible, K-shell emission of carbon ions was less intensive and the influence of electrode material seemed to be more apparent than with a 15  $\mu\text{m}$  diameter fibre. In the case of a 80  $\mu\text{m}$  diameter fibre, XUV pulses lasted longer and the fibre was probably not fully ablated. However, the comparison between different fibre diameters was dependent on the shape of electrodes. In addition, shot-to-shot variation prevented us from detail quantitative comparison. The discussion of this shot-to-shot variation goes beyond the scope of our experiment because we were mainly focused on the basic description of Z-pinch dynamics and it was not our ambition at that time to study and, by extension, to increase the discharge reproducibility.

<sup>21</sup> As examples, we could mention the occurrence of XUV pulses, dips in  $dI/dt$ , and plasma-on-fibre.

## Chapter 5

### DISCUSSION

In this chapter we compare our results with other Z–pinch experiments. First, we shall summarise the most important results of other fibre experiments. Then, we will point out results which are similar or different to ours. The particularity of our fibre Z–pinch is the implosion of a coronal plasma onto a fibre and thus it will be treated of in more detail. Finally, we will deal with the most energetic phase of our discharge which occurred in electrode vapour.

#### 5.1 *Fibre Z–pinch Experiments*

Fibre Z–pinch experiments were carried out on modern high–voltage pulsed–power generators at Los Alamos National Laboratory, Naval Research Laboratory, Imperial College in London, Kernforschungszentrum Karlsruhe, and Kurchatov Institute in Moscow (see section 1.3 and appendix C). Even though each experimental group observed somewhat different behaviour of a fibre Z–pinch, the gross dynamics of a fibre pinch was described. We shall sum up the most important findings of these research groups in the following text.

We start with the global expansion of a coronal plasma surrounding the solid core. The expansion was observed although the Pease–Braginskii current was reached and the current rise was fast enough to cause the radiative collapse. This rapid expansion could happen for several reasons and we touch upon them briefly. One of the reasons might be anomalous resistivity in a low density coronal plasma which, if it occurs, causes the plasma kinetic pressure to exceed the magnetic pressure (Chittenden, 1995). As a result, the Bennett equilibrium does not hold and the pinch expands. Another reason for the expansion may lie in MHD instabilities. During the development of an  $m = 0$  instability, the bulges of the instability expand and the constricted regions cause enhanced

non-uniform heating of the core (Sheehey et al., 1992; Riley et al., 1996). An  $m = 0$  instability was apparent very early in the discharge in shadowgrams and schlieren images. These instabilities exhibited highly dynamic behaviour (Chittenden et al., 1997), but they were not disruptive (most likely because of the dense core which lasted for a relative long time). During the interaction of the coronal plasma with the remaining dense core, bright spots occurred. After the dynamic bright-spot phase, the disruption accompanied with the neutron production and X-ray emission was observed as soon as the fibre was completely ablated.

All these results, but mainly the rapid expansion and the early development of plasma instabilities, effectively decrease the plasma density and eliminate the possibility of using a fibre Z-pinch as a fusion reactor.

## 5.2 *Implosion of Coronal Plasma onto Central Fibre*

Our work with a carbon fibre Z-pinch brought some results that were to a certain extent similar to those of above mentioned experiments despite the fact that peak currents and rise times were substantially different. Similarly to these experiments, we made the following observations:

- A low density coronal plasma carried almost all the current, a cold dense core persisted for a long time. The interaction of a coronal plasma with this dense core then substantially influenced the plasma dynamics.
- The XUV emission came mainly from bright spots which were produced by instabilities that developed in a low density corona. However, these instabilities were not disruptive as long as the dense core survived unionised.
- After the fibre ablation, the intense X-ray radiation was produced.

Nevertheless, our Z-pinch differed in several issues of a great importance too. Fibre Z-pinches driven by fast pulsed power generators are usually considered to be in pressure balance because the current rises rapidly and the plasma pressure could be balanced against the magnetic forces in every moment. Contrary to that, our fibre Z-pinch driven by microsecond capacitive discharge expanded first to the diameter of about one centimetre. When the current built up, the implosion of a coronal plasma onto a central fibre occurred. This means that our fibre Z-pinch behaved as a dynamic pinch for a lapse of

time. Even though the current was about 40 kA, the implosion velocity approached the value of  $2 \times 10^5 \text{ m s}^{-1}$  which implies the kinetic energy of carbon ions of about 2.5 keV.

It is true that noticeable implosion could be observed also on pulsed power generators, however, the current prepulse<sup>1</sup> must be applied. Such experiment was carried out on a pulsed power generator IMP ( $I_{\max} = 200 \text{ kA}$ ,  $t_{10\%-90\%} = 60 \text{ ns}$ , Imperial College, London, Lorenz et al., 1998). In this experiment, the prepulse delivered 10 kA current with a 50 ns quarter period into a 7  $\mu\text{m}$  diameter carbon fibre. The breakdown of the fibre occurred when the voltage reached about 20 kV. The prepulse generated a low density coronal plasma of  $N_i = 3 \times 10^{17} \text{ m}^{-1}$  (cf. with our value of  $8 \times 10^{17} \text{ m}^{-1}$ , page 83) which expanded to a radius of the order of a millimetre. After the switch of the main discharge current, they observed, similarly as we did, implosion of a low density plasma onto a fibre<sup>2</sup>, the zipper from the cathode towards the anode, the soft X-ray pulse, and subsequent rapid expansion.

Another similar feature between Lorenz's and our experiment was the observation of  $m = 0$  and  $m = 1$  instabilities during the stagnation of the corona at the fibre. For Alfvén velocity of  $2 \times 10^5 \text{ ms}^{-1}$ , the pinch diameter of about 1 mm, and the conductivity of  $10^5 \text{ S m}^{-1}$ , the ideal MHD model predicts the characteristic time of instability growth  $\tau = R/v_A = 2.5 \text{ ns}$ . Despite a low Lundquist number  $S = \mu\sigma v_A R \approx 10$ , enhanced stability was not confirmed and the presence of a fibre did not seem to significantly suppress MHD instabilities. However, these were not excessively disruptive.

The development of instabilities caused the generation of XUV pulses from several bright spots. Because of a low current and, by extension, a relative high resistivity, the main heating mechanism was most likely Joule heating. Nevertheless, the  $\dot{L}_P$  term cannot be ruled out. In that case, plasma instabilities could provide an effective mechanism for dissipating the magnetic energy adjacent to the pinch.

The coronal plasma in our experiment and in the experiment of Lorenz et al. (1998) was formed from a fibre. Another possibility would be to create a plasma from a wire–array or gas–puff which subsequently implodes onto a central fibre. We shall look at these two approaches in the following sections. As regards the difference between the coronal plasma created from a fibre and the plasma formed from a wire–array or gas–puff, the

<sup>1</sup> Recently, a current prepulse applied before the main pulse has been suggested to evaporate a wire and to allow it to expand. The reason for that is to create a homogenous plasma for subsequent implosion (Choi and Zakharov, 2005).

<sup>2</sup> In Lorenz's experiment, the faster current rise–time implied lower skin depth and thus the *snowplough* implosion occurred.

higher mass was imploded onto a fibre in experiments with wire–arrays or gas–puffs. Clearly, the energetics of these Z–pinches is dominated by the implosion energy. In our fibre experiment, the implosion energy was relatively low. Much more important phenomena was probably the transfer of the current in the vicinity of a fibre when the corona imploded.

### 5.3 Wire–Array and Gas–Puff Implosion onto Central Fibre

The implosion of a wire–array Z–pinch onto a deuterated fibre was studied on the S–300 device (4 MA, 700 kV and 100 ns; RRC Kurchatov Institute, Moscow). These experiments were performed at a peak current of about 2 MA with a rise time of about 100 ns (Klír et al., 2004a, 2005). An aluminium wire–array of 1 cm in diameter was used as a load. Each wire–array consisted of 30  $\div$  60 aluminium wires of 15  $\mu\text{m}$  in diameter and 1 cm in length. The deuterated polyethylene  $(\text{CD}_2)_n$  fibres with diameters between 80 and 120  $\mu\text{m}$  were placed on the axis of the array. The purpose of these experiments on the S–300 generator was to study the generation of XUV and X–ray radiation together with the neutron production. It was found out that the implosion of a wire–array had the positive influence on the neutron yield. The neutron yield was one order in magnitude higher in the case of an imploding wire–array onto a fibre than without a wire–array (cf. Klír et al., 2004a, 2005 and appendix C).

Two shots with 240 aluminium wires imploding onto a  $(\text{CD}_2)_n$  fibre were also carried out on Z–machine in 1998. However, more neutrons of  $(2.8 \pm 0.2) \times 10^{12}$  were generated on Saturn during the implosion of a hollow deuterium gas–puff<sup>3</sup> onto a 250  $\mu\text{m}$  deuterated polyethylene fibre located on the pinch axis (Spielman et al., 1991). Recently, the highest neutron yield from the D–D reaction of  $6 \times 10^{13}$  has been achieved with double–shell deuterium gas–puff, i.e. without any fibre (Velikovich et al., 2005).

On the basis of our results and observations of other research groups, we believe that the implosion onto a fibre offers the possibility of current transfer near the fibre. However, when one considers higher neutron yield, solid fibres are probably less suitable than deuterium gas–puffs.

---

<sup>3</sup> This configuration was very similar to the deuterium plasma–sheath imploding onto a  $(\text{CD}_2)_n$  fibre on the PF–1000 plasma focus (Kubeš et al., 2004).

#### 5.4 Plasma – on – Wire

The peculiarity of a solid fibre is its initial non-conductivity that causes the transfer of the current from a fibre and thus makes the energy coupling into a fibre difficult. Different situation occurs when a conducting wire is used instead of a fibre. The implosion of an aluminium jet onto a coaxial aluminium wire was first studied by Wessel et al. (1992). They found the resultant plasma to be more uniform and hotter than a wire-only and jet-only pinch. The pinch also demonstrated that an imploding plasma could couple the energy from a current generator to a micron-sized wire.

Our experiments on the PF-1000 plasma focus in Warsaw showed similar behaviour. In some shots with deuterium filling, we placed an Al wire at the axis and top of the anode having no galvanic connection to the anode. Fig. 5.1 shows the spatially resolved spectrum recorded with the time-integrated X-ray spectrograph, which detected resonance, intercombination and satellite lines of He-like aluminium ions. Clearly, the whole length of an Al wire did not manifest typical large-scale instabilities which are characteristic for wire Z-pinches. If we realise that the length of a wire was 8 cm, it was quite an impressive result for a pinch plasma, which may lead to reconsideration of a wire Z-pinch as an X-ray laser medium.

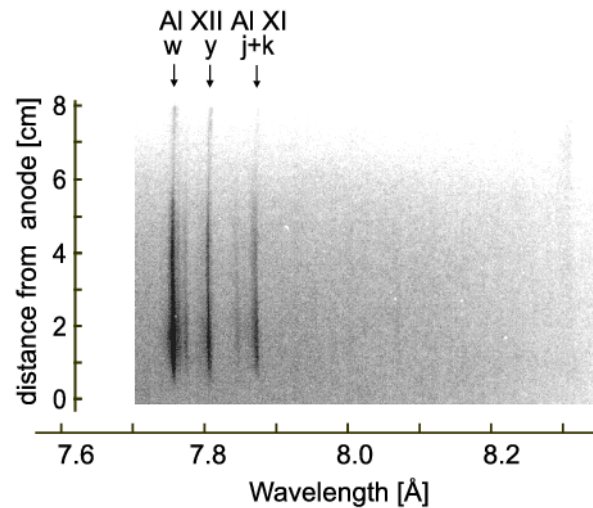


Fig. 5.1: Spatially resolved X-ray spectrum recorded by V. M. Romanova during the implosion of the deuterium plasma-sheath onto an Al wire (80  $\mu\text{m}$  diameter and 8 cm length), PF-1000 plasma focus (IPPLM, Warsaw), shot no. 2564, 1.5 MA peak current, deuterium filled up to 3 Torr.

Having dealt with the plasma – on – fibre phase of our discharge, we shall now turn to the phase in which electrode vapour determined plasma dynamics.

### 5.5 Discharge in Electrode Vapour and Bright Spots

The influence of electrode vapour on Z–pinch dynamics was visibly increasing with the growing time. The dominant role of the material evaporated from the electrodes was apparent after the fibre ablation. After that we observed bright spots and hard X–ray emission together with sharp voltage spikes and dips in  $dI/dt$ . As far as the gradual rise of plasma voltage is concerned, it could be explained by the implosion of a plasma column. However, the implosion could not cause the observed sharp increase of voltage which was related to the development of plasma instabilities near the maximum compression.

Much alike results were also obtained in plasma foci, vacuum sparks and higher–Z gas–puffs driven by low impedance generators. This phase of the discharge produces the most energetic electrons, ions, and photons, therefore a large number of mechanisms were suggested to explain the production of fast particles (see, for instance, Anderson et al., 1958; Haines, 1983; Trubnikov, 1986; Vikhrev, 1986; Deutsch and Kies, 1988; Herold et al., 1988, a recent review given by Haines, 2001 and Ryutov et al., 2000). Basically, we can distinguish three mechanisms that exist in various modifications (Ryutov et al., 2000):

- The first explanation from the 1950s suggests that charged particles are accelerated by a high inductive voltage in the neck during the development of an  $m = 0$  instability.
- In another mechanism, the production of fast particles is ascribed to an adiabatic compression of plasma in the neck of an instability.
- The third explanation is based on microinstabilities that could be triggered in a low density plasma with high current density, for instance within  $m = 0$  instabilities. Microinstabilities then result both in strong anomalous heating and in the formation of a non–Maxwellian tail of the ion velocity distribution.

If the charged particles are not of thermal origin, they have to be accelerated by the voltage across the plasma  $U_P = (R_P + \dot{L}_P)I + L_P \dot{I}$ . In high current fibre Z–pinches, there was no evidence of pinching or expansion of a dense plasma at the time of disruption

(see Robledo et al., 1997; Mitchell et al., 1998). The rise of plasma voltage could be therefore explained by microinstabilities triggered in a low density plasma. At this point we would like to draw the attention to the long duration of energetic particle emission. Such long pulses (several tens of ns) can be hardly explained by  $\dot{L}_P$  and  $\dot{I}$  because the inductance and current would have to be changing for a very long time. The rise of plasma resistance  $R_P$  seems to be much more feasible.

In our experiment, we also observed the rapid rise-time of X-rays and relatively long (several tens of nanoseconds) duration of X-ray pulse (cf. Fig. 4.23 on page 100). However, we do not have any experimental evidence of electron and ion beams and thus we do not discuss the mechanisms of charged particle acceleration in greater detail. Instead of that, we shall conclude this chapter by a report on bright spots that were observed in our experiment.

### *Bright spots*

Bright spots are localised plasma regions intensively radiating in visible, XUV and X-ray spectral ranges. They were thoroughly studied first in a vacuum spark (Cohen et al., 1968). Since then they have been often observed in all types of Z-pinchers. The temperature, density and life-time of bright spots varied over several orders of magnitude and different kinds of bright spots have been reported. Even though the origin of bright spots is still being discussed, it is clear that the nonlinear phase of the sausage instability, radiative collapse and anomalous resistivity play a very important role (Vikhrev et al., 1982; Erber et al., 2000).

In our experiment, we have to distinguish two types of bright spots. The first group of bright spots was produced during the plasma – on – fibre phase. These bright spots emitted less energetic photons than bright spots created in electrode vapour. To avoid confusion, we call the latter ones “hot” spots. These hot spots arose from  $m = 0$  instabilities. Because the discharge occurred in electrode vapour, higher-Z ions (copper, tin, etc.) increased radiation losses through line emission. After the fibre ablation,  $m = 0$  instabilities could develop significantly according to the radiative collapse model (see 2.1.2 on page 28). As far as the position of hot spots occurrence is concerned, they appeared predominantly near the anode similarly to vacuum sparks (Koshelev and Pereira, 1991).

## SUMMARY, CONCLUSIONS AND PROSPECTS

The following pages first summarise the results obtained in our experiment. After that, conclusions from these results are presented. Finally, prospects for the future are proposed.

### *Summary*

The primary aim of this thesis has been the study of the evolution and gross dynamics of a fibre Z–pinch. Our experiments were driven by a slow capacitive discharge of about 1 kJ energy. The current generator delivered 80 kA with 850 ns quarter period into a load. Most of the experiments were performed in vacuum with carbon fibres of 15  $\mu\text{m}$  diameter and about 1 cm length. The plasma was observed with a large number of diagnostic tools. Particularly, simultaneous diagnostics (XUV spectra, VUV pinhole images and schlieren images) were very helpful.

The characteristic feature of our experiments were XUV and X–ray pulses accompanied with rises of voltage and with dips in  $dI/dt$ . In order to find the origin of these pulses, an in–depth experimental study was performed. During this study, we distinguished several phases of our Z–pinch, namely the breakdown, latent phase, plasma – on – fibre, fibre ablation, implosion of material evaporated from electrodes, development of  $m = 0$  instabilities and bright spots. We found out that XUV pulses were first emitted during the development of instabilities in the plasma – on – fibre stage. After the ablation of a fibre, both XUV and X–ray pulses were generated from hot spots which developed in higher–Z material evaporated from electrodes. The energetics of the Z–pinch and basic plasma parameters were estimated in each phase. We also made an attempt to discuss relevant heating mechanisms.

## Conclusions

In conclusion it should be stressed that the dynamics of a fibre Z–pinch substantially differs from Z–pinches initiated from a metal wire. Even though ICF purposes caused a carbon fibre Z–pinch to be of a modest interest now, we believe that unique properties of carbon could provide valuable data not only for Z–pinch physics but also for material science in which carbon is often used. Our experiment with a carbon fibre proved that it is possible to study a lot of Z–pinch phenomena on a small device provided that a plasma is thoroughly diagnosed. As an example we could mention the study of *Z–pinch implosion* with the velocity above  $10^5$  m s $^{-1}$  on the current level of 50 kA. Another interesting phenomenon is the implosion *onto a fibre or wire*. First, it offers a new possibility of how to transfer the current with a sharp rise–time in the vicinity of a fibre or how to modify the shape of an X–ray pulse. Next, the fibre in the centre of an imploding plasma introduces homogeneity to Z–pinch discharges. Last but not least, a fibre can be used as a target for an imploding plasma and can serve as a diagnostic tool.

Our results also showed that dynamics of a fibre Z–pinch significantly varies depending on a current generator used. In the case of a slow current rise–time, the implosion of a coronal plasma onto a fibre might occur late in the time. This way, more energy stored in a capacitor bank could be transferred into a plasma.

Furthermore, the current waveform of a low impedance and low voltage capacitor is quite sensitive to Z–pinch behaviour, especially to the change of the  $R_P + \dot{L}_P$  term. Although this fact is considered to be a disadvantage, it can serve well some diagnostic purposes. Since the voltage and current can be quite easily measured on a low voltage generator, we can calculate a plasma resistance and energetics of a Z–pinch. Moreover, if we assume cylindrical symmetry and Spitzer resistivity, the resistance and spectroscopically measured temperature determine the diameter of a plasma column in which the current is flowing. Then this diameter can be compared with the one estimated from schlieren or pinhole images. Thus, we are coming to one of the main problem of Z–pinches: what does the distribution of a current flowing through a plasma look like? Of course, it is necessary to measure the current distribution locally. However, the above mentioned technique gives at least a rough estimation of a diameter.

### *Future prospects*

Present investigation describes only the gross dynamics of our fibre Z–pinch. All of observed phenomena could be studied in greater extent. Further experimental work depends on the subject of interest, i.e. which of the observed phenomena we want to study in detail. According to this interest, the diagnostics should be improved. One may attempt to increase the current, to increase the length of a fibre, to use more fibres in one shot, to detect a low density corona in the latent phase, to detect charged particles, to perform X–ray spectroscopic measurement of hot spots, etc. But what should be improved in any case, is the modelling without which it is almost impossible to get deeper insight into Z–pinch phenomena.

It is well known that a fibre Z–pinch does not belong to the main stream of Z–pinch research because it is not such efficient radiation source as high-Z wires. That is why experiments with carbon fibres are limited to basic research, i.e. to the study of general phenomena such as plasma implosion, instabilities, bright spots, resistance, current distribution, etc. However, the future work is not restricted to a carbon fibre. The contribution of our experiments lies also in the development of a comprehensive set of diagnostics, which could be used for various Z–pinch loads and configurations.

## BIBLIOGRAPHY

Aliaga-Rossel, R., Lebedev, S., Chittenden, J., et al. (1998). Optical measurements of plasma dynamics in carbon fiber Z–pinches. *IEEE Transactions on Plasma Science*, 26:1101–1107.

Anderson, O., Baker, W., Stirling, A., Ise, J., and Pyle, R. (1958). Neutron production in linear deuterium pinches. *Physical Review*, 110(6):1375–1383.

Aschke, L. (1999). *Untersuchung der Wechselwirkungszone kollidierender Plasmen*. PhD thesis, Fakultät für Physik und Astronomie, Ruhr–Universität Bochum.

Attwood, D. (1999). *Soft X–rays and extreme ultraviolet radiation: Principles and Applications*. Cambridge University Press, New York, USA. ISBN 0-521-65214-6.

Bailey, J., Chandler, G., Cohen, D., et al. (2002a). Radiation science using Z–pinch X-rays. *Physics of Plasmas*, 9:2186–2194.

Bailey, J., Chandler, G., Slutz, S., et al. (2002b). X–ray imaging measurements of capsule implosions driven by a Z–pinch dynamic hohlraum. *Physical Review Letters*, 89:095004.

Bailey, J., Chandler, G., Slutz, S., et al. (2004). Hot dense capsule–implosion cores produced by Z–pinch dynamic hohlraum radiation. *Physical Review Letters*, 92:085002.

Bailey, J., Ettinger, Y., Fisher, A., and Feder, R. (1982). Evaluation of the gas puff Z–pinch as an X–ray lithography and microscopy source. *Applied Physics Letters*, 40:33–35.

Batyunin, A. (1990). Study of an ultrafast Z–pinch on the Angara 5-1 device. *Soviet Journal of Plasma Physics*, 16(9):597–601.

Beg, F., Dangor, A., Lee, P., Tatarakis, M., Niffikeer, S., and Haines, M. (1997). Optical and X-ray observations of carbon and aluminium fibre Z-pinch plasmas. *Plasma Physics and Controlled Fusion*, 39:1–25.

Bennett, W. (1934). Magnetically self-focusing streams. *Physical Review*, 45:890–897.

BURLE technologies, INC. (2005). Channeltron electron multiplier handbook for mass spectroscopy applications. <http://www.burle.com/cgi-bin/byteserver.pl/pdf/ChannelBook.pdf>.

Carruthers, R. and Davenport, P. (1957). Observation of the instability of constricted gaseous discharge. *Proc. Phys. Soc. B*, 70:49–50.

Chace, W. and Moore, H., editors (1968). *Exploding Wires*, volume 4, New York, USA. Plenum Press.

Chemical cool (2005). Chemical cool periodic table. <http://www.chemicalcool.com>.

Chernenko, A., Kalinin, Y., and Kingsep, A. (1996). S-300, New pulsed power installation in Kurchatov Institute, Investigation of stable liner implosion. In Jungwirth, K. and Ullschmied, J., editors, *BEAMS 1996*, pages 154–157, Prague, Czech Republic.

Chittenden, J. (1995). The effect of lower hybrid instabilities on plasma confinement in fiber Z-pinches. *Physics of Plasmas*, 2:1242–1249.

Chittenden, J., Lebedev, S., Jennings, C., Bland, S., and Ciardi, A. (2004). X-ray generation mechanisms in three-dimensional simulations of wire array Z-pinches. *Plasma Physics and Controlled Fusion*, 46:B457–B476.

Chittenden, J., Mitchell, I., Aliaga-Rossel, R., et al. (1997). The dynamics of bifurcation bright-spots in fiber Z-pinch plasmas. *Physics of Plasmas*, 4(8):2967–2966.

Chittenden, J., Vincent, P., Jennings, C., and Ciardi, A. (2005). Hotspot ignition using a Z-pinch precursor plasma in a magneto-inertial ICF scheme. In *6<sup>th</sup> International Conference on Dense Z-Pinches, AIP conference proceedings*. To be published.

Choi, P. and Zakharov, S. (2005). A Two Step Plasma Conditioning Scheme for High Current Plasma Implosions. In *6<sup>th</sup> International Conference on Dense Z-Pinches, AIP conference proceedings*. To be published.

Chung, H., Morgan, W., and Lee, R. (2003). FLYCHK: an extension to the K-shell spectroscopy kinetics model FLY. *J. Quant. Spectrosc. Radiat. Transfer*, 81:107–115.

Cochran, F. and Robson, A. (1990a). Non ideal MHD effects on the evolution of DZP plasmas. In Ortolani, S. and Sindoni, E., editors, *Proceedings of the Workshop on Physics of Alternative Magnetic Confinement Schemes*, page 395, Bologna, Italy. Editrice Compositori.

Cochran, F. and Robson, A. (1990b). Stability of a Z–pinch with rising current. *Physics of Fluids B*, 2:123–128.

Cohen, L., Feldman, U., Swartz, M., and Underwood, J. (1968). Study of the X–rays produced by a vacuum ultraviolet spark. *Journal of Optical Society of America*, 58:843–846.

Coppins, M. (1989). Ideal magnetohydrodynamic linear instabilities in the Z–pinch. *Plasma Physics and Controlled Fusion*, 30:201–216.

Coppins, M. (1997). A review of the stability of the Z–pinch. In Pereira, N., Davis, J., and Pulsifer, P., editors, *Fourth International Conference on Dense Z–Pinches*, pages 533–548, Woodbury, New York. American Institute of Physics.

Coppins, M., Bond, D., and Haines, M. (1984). A study of the stability of the Z–pinch under fusion conditions using the hall fluid model. *Physics of Fluids*, 27:2886–2889.

Coppins, M. and Culverwell, I. (1997). Resistive stability of the Z–pinch revisited. In Pereira, N., Davis, J., and Pulsifer, P., editors, *Fourth International Conference on Dense Z–Pinches*, pages 589–592, Woodbury, New York. American Institute of Physics.

Coppins, M. and Scheffel, J. (1992). Anisotropic Z–pinch equilibria and their stability. *Physics of Fluids B*, 4:3251–3260.

Culverwell, I. and Coppins, M. (1990). Resistive Z–pinch stability theory. *Physics of Fluids B*, 2:129–132.

Cuneo, M., Vesey, R., Porter, J., et al. (2002). Double Z–pinch hohlraum drive with excellent temperature balance for symmetric inertial confinement fusion capsule implosions. *Physical Review Letters*, 88:215004.

CXRO (2004). X-ray interaction with matter. <http://www-cxro.lbl.gov>.

Davies, H., Lorenz, A., Kravárik, J., and Kubeš, P. (1997). Diagnostics of the thick carbon fibre Z–pinch. In Pereira, N., Davis, J., and Pulsifer, P., editors, *Fourth International Conference on Dense Z–Pinches*, pages 507–511, Woodbury, New York. American Institute of Physics.

De Michelis, C. and Mattioli, M. (1981). Soft–X–ray spectroscopic diagnostics of laboratory plasmas. *Nuclear Fusion*, 21(6):677–754.

Decker, G. and Kies, W. (1989). Pinch experiments performed with SPEED 2 and KALIF. In Pereira, N. R., Davis, J., and Rostoker, N., editors, *Second International Conference on Dense Z–Pinches*, pages 315–319, New York. American Institute of Physics.

Deeney, C., Coverdale, C., and Douglas, M. (2001). A review of long–implosion–time Z–pinches as efficient and high–power radiation sources. *Laser and Particle Beams*, 19:497–506.

Deeney, C., Douglas, M., Spielman, R., et al. (1998). Enhancement of X–ray power from a Z–pinch using nested wire arrays. *Physical Review Letters*, 81(22):4883–4886.

Deeney, C. et al. (1999). Radiative properties of high wire number tungsten arrays with implosion times up to 250 ns. *Physics of Plasmas*, 6:3576–3586.

Deeney, C., Nash, T., Spielman, R., et al. (1997). Power enhancement by increasing the initial array radius and wire number of tungsten Z–pinches. *Physical Review E*, 56:5945–5958.

Degnan, J. (1995). Electromagnetic implosion of spherical liner. *Physical Review Letters*, 74:98–101.

Deutsch, R. and Kies, W. (1988). Manifestation of an ion acceleration mechanism in computer simulations and plasma focus experiments. *Plasma Physics and Controlled Fusion*, 30:921.

Duselis, P., Vaughan, J., and Kusse, B. (2004). Factors affecting energy deposition and expansion in single wire low current experiments. *Physics of Plasmas*, 11:4025–4031.

Eberl, E., Jelinek, S., Latteyer, Y., Tauschwitz, A., and Hoffmann, D. (1998). Amplification in an argon Z–pinch plasma. *Nuclear Instruments and Methods in Physics Research A*, 415:628–631.

Ellwi, S., Andreic, Z., Pleslic, S., and Kunze, H. (2001). Probing of the active layers in a capillary discharge soft X–ray laser at 18.22 nm. *Physics Letters A*, 292:125–128.

Ellwi, S., Juschkin, L., Ferri, S., Kunze, H., and Louis, E. (2000). Investigation of X–ray lasing in a capillary discharge. *Journal de Physique IV*, 11(PR2):1376–1384.

Elton, R. (1990). *X–ray Lasers*. Academic Press, New York, USA. ISBN 0-12-238080-0.

Erber, C., Koshelev, K., and Kunze, H. (2000). Time development of Mg micropinchers in a low-inductance vacuum spark discharge. *J. Quant. Spectrosc. Radiat. Transfer*, 65:195–206.

Felber, F., Liberman, M., and Velikovich, A. (1985). Methods for producing ultrahigh magnetic fields. *Applied Physics Letters*, 46:1042–1044.

Figura, E., McCall, G., and Dangor, A. (1991). Characteristics of a Z–pinch produced from a glass optical fiber. *Physics of Fluids B*, 3:2835–2843.

Garasi, S., Bliss, D., Mehlhorn, T., Oliver, B., Robinson, A., and Sarkisov, G. (2004). Multi–dimensional high energy density physics modelling and simulation of wire array Z–pinch physics. *Physics of Plasmas*, 11:2729–2737.

Grabovsky E. (2001). Wire array implosion study on Angara-5-1. 3<sup>rd</sup> international workshop on the physics of wire array Z–pinches. <http://www.pp.ph.ic.ac.uk/~magpie/workshop/agenda.htm>.

Griem, H. R. (1964). *Plasma Spectroscopy*. McGraw–Hill, New York, USA.

Griem, H. R. (1974). *Spectral Line Broadening by Plasmas*. Academic Press, New York, USA.

Griem, H. R. (1997). *Principles of Plasma Spectroscopy*. Cambridge University Press, Great Britain.

Haines, M. (1983). Ion beam formation in an  $m = 0$  unstable Z–pinch. *Nuclear Instruments and Methods in Physics Research*, 207:179–185.

Haines, M. (1996). Fifty years of controlled fusion research. *Plasma Physics and Controlled Fusion*, 38:643–656.

Haines, M. (1997). An overview of the DZP project at Imperial College. In Pereira, N., Davis, J., and Pulsifer, P., editors, *Fourth International Conference on Dense Z-Pinches*, pages 27–38, Woodbury, New York. American Institute of Physics.

Haines, M. (2001). Kinetic effects in Z-pinch. *Laser and Particle Beams*, 19:345–353.

Haines, M. and Coppins, M. (1991). Universal diagram for regimes of Z-pinch stability. *Physical Review Letters*, 66:1462.

Haines, M., Dangor, A., Coppins, M., et al. (1996). Fiber Z-pinch experiments and calculations in the finite larmor radius regime. *Laser and Particle Beams*, 14:261–271.

Haines, M., Lebedev, S., Chittenden, J., Beg, F., Bland, S., and Dangor, A. (2000). The past, present, and future of Z pinches. *Physics of Plasmas*, 7(5):1672–1680.

Haines, M., LePell, P., Coverdale, C., Jones, B., and Deeney, C. (2004). Ion viscous heating in a wire-array Z-pinch. In *31<sup>st</sup> EPS Conference on Plasma Physics*, pages 0–2.20.

Hamamatsu (2005). Photomultiplier modules. <http://sales.hamamatsu.com/en/products/electron-tube-division/detectors/pmt-modules/h1949-51.php>.

Hammel, J. and Scudder, D. (1987). High density Z-pinch formed from a solid deuterium fiber. In *Proceedings of 14<sup>th</sup> European Conference on Controlled Fusion and Plasma Physics.*, page 450, Madrid, Spain.

Hammel, J., Scudder, D., and Schlachter, J. (1983). Recent results on dense Z-pinch. *Nuclear Instruments and Methods*, 107:161–168.

Hammer, D. and Sinars, D. (2001). Single-wire explosion experiments relevant to the initial stages of wire array Z-pinch. *Laser and Particle Beams*, 19:377–391.

Harada, T. and Kita, T. (1980). Mechanically ruled aberration-corrected concave grating. *Applied Optics*, 23:3987.

Hauer, A., Delamater, N., and Koenig, Z. (1991). High-resolution X-ray spectroscopic diagnostics of laser-heated and ICF plasmas. *Laser and Particle Beams*, 9(1):3–48.

Haun, J. (2001). *Leitfähigkeitsmessungen an stark gekoppelten Kohlenstoff- und Zinkplasmen*. PhD thesis, Fakultät für Physik und Astronomie, Ruhr–Universität Bochum.

Haun, J., Kunze, H., Kosse, S., Schlanges, M., and Redmer, R. (2002). Electrical conductivity of nonideal carbon and zinc plasmas: Experimental and theoretical results. *Physical Review E*, 64:no. 046407.

Henke, B., Gullikson, E., and Davis, J. (1993). X–ray interactions: Photoabsorption, scattering, transmission, and reflection at  $E = 50\text{--}30000$  eV,  $Z = 1\text{--}92$ . *Atomic Data and Nucl. Data Tables*, 54:181–342.

Herold, H., Kaeppler, H., Schmidt, H., et al. (1988). Progress in plasma focus operation up to 500 kJ bank energy. In *Proc. 12<sup>th</sup> Intern. Conference on Plasma Physics and Controlled Nuclear Fusion Research, Nice, 1988*, pages CN–50/C–4–5–3.

Horák, Z. and Krupka, F. (1981). *Fyzika*. SNTL, Prague, Czech Republic. 04-017-81.

Hosokai, T., Kando, M., Dewa, H., et al. (2000). Optical guidance of terrawatt laser pulses by the implosion phase of a fast Z–pinch discharge in a gas–filled capillary. *Optics Letters*, 25:10–12.

Hutley, M. (1982). *Diffraction Gratings*. Academic Press, London.

Ishii, S., Fukuta, M., Shimizu, K., et al. (1989). Dense Z–pinches by carbon fiber pinch and by conductive thin film liner compression. In Pereira, N. R., Davis, J., and Rostoker, N., editors, *Second International Conference on Dense Z–Pinches*, pages 320–326, New York. American Institute of Physics.

Ishii, S., Hoshina, Y., Furuya, S., et al. (1993). Dense Z–pinch of solid material with high atomic number. In *1993 IEEE International Conference on Plasma Science.*, page 2P26, Piscataway, NJ, USA. IEEE.

Johnston, M., Lau, Y., Gilgenbach, R., et al. (2003). Caterpillar structures in single-wire Z–pinch experiments. *Applied Physics Letters*, 83:4915–4917.

Kadomtsev, B. (1963). Гидромагнитная истойчивость плазмы. In Вопросы Теории Плазмы, volume 2, pages 132–176. Госатомиздат, Москва.

Kalantar, D. and Hammer, D. (1993). Observation of a stable dense core within an unstable coronal plasma in wire-initiated dense Z-pinch experiments. *Physical Review Letters*, 71:3806–309.

Kelly, R. (1987). Atomic and ionic spectrum lines below 2000 Angstroms: Hydrogen through krypton. *J. Phys. Chem. Ref. Data*, 16:Suppl. 1. Also available online: <http://cfa-www.harvard.edu/amdata/ampdata/kelly/kelly.html>.

Kies, W., Decker, G., Malzig, M., et al. (1991). Terawatt fiber pinch experiments. *Journal of Applied Physics*, 70(12):7261–7272.

Kita, T., Harada, T., Nakano, N., and Kuroda, H. (1983). Mechanically ruled, aberation corrected, concave grating for a flat field grazing incidence spectrograph. *Applied Optics*, 22:512.

Klír, D. (2002). *Studium XUV a měkkého rentgenového záření v magnetických pinčích*. Diploma thesis. Czech Technical University, Prague.

Klír, D., Kravárik, J., Kubeš, P., et al. (2004a). XUV and soft X-ray emission from fast Z-pinch discharge. In Hammel, B., Meyerhofer, D., Meyer-ter Vehn, J., and Azechi, H., editors, *Inertial Fusion Sciences and Applications 2003*, pages 735–738, La Grange Park, Illinois, USA. American Nuclear Society, Inc.

Klír, D., Kravárik, J., Kubeš, P., et al. (2005). Wire-array implosion onto a deuterated fibre at the S-300 facility. *Plasma Devices and Operations*, 13:39–43.

Klír, D., Kubeš, P., and Kravárik, J. (2004b). Carbon fiber Z-pinch driven by microsecondlong capacitive discharge. *Czechoslovak Journal of Physics*, 54:C264–C273.

Koshelev, K. (1999). *LPS Grazing Incidence VUV Spectrometer LPS-VUVI-3S-M*. Technical Description and Manual. Unpublished.

Koshelev, K. and Kunze, H. (1997). Population inversion in a discharge plasma with neck-type instabilities. *Quantum Electronics*, 27:164–167.

Koshelev, K. and Pereira, N. (1991). Plasma points and radiative collapse in vacuum sparks. *Journal of Applied Physics*, 69:R21–R44.

Koshelev, K., Sidelnikov, Y., Churilov, S., and Dorokhin, L. (1994). Charge–exchange of plasma beams from instabilities in axial discharges and population inversion in highly charged ions. *Physics Letters A*, 193:149–154.

Kozlík, V. (2002). *VN napájení Z–pinčové aparatury a jeho regulace*. Diploma Thesis. Czech Technical University, Prague.

Kruskal, M. and Schwarzschild, M. (1954). Some instabilities of a completely ionized gas. *Proc. R. Soc. London A*, 223:348.

Kubeš, P., Kravárik, J., Klír, D., et al. (2003). Influence of carbon fiber on megaamper plasma focus radiation. In *E–Book Int. Conf. Plasma 2003*, page P3.8, Warsaw, Poland.

Kubeš, P., Kravárik, J., Klír, D., et al. (2004). Influence of  $CD_2$  fiber on the compression in the PF-1000 facility. *Czechoslovak Journal of Physics*, 54:C285–C290.

Kubeš, P., Renner, O., Kravárik, J., et al. (2002). Dynamics of an Al wire corona of a megaampere Z–pinch. *Plasma Physics Report*, 28:296–302.

Kunze, H. (1994). Lasing mechanism in a capillary discharge. *Physics Letters A*, 193:183–187.

Kunze, H. J. (1989). Spectroscopy of Z–pinches. In Pereira, N. R., Davis, J., and Roskoker, N., editors, *Second International Conference on Dense Z–Pinches.*, pages 96–107, New York.

Kurchatov, I. (1957). On the possibility of producing thermonuclear reactions in a gas discharge. *Journal of Nuclear Energy*, 4:193.

Lash, J., Chandler, G., Cooper, G., et al. (2000). The prospects for high yield ICF with a Z–pinch driven dynamic hohlraum. *C. R. Acad. Sci. Paris*, Ser. IV:759–765.

Lebedev, S., Aliaga-Rossel, R., Chittenden, J., et al. (1998). Coronal plasma behavior of the Z–pinch produced from carbon and cryogenic deuterium fibers. *Physics of Plasmas*, 5(9):3366–3372.

Lebedev, S., Beg, F., Bland, S., et al. (2000). Effect of core–corona plasma structure on seeding of instabilities in wire array Z–pinches. *Physical Review Letters*, 85:98–101.

Lebedev, S., Beg, F., Bland, S., et al. (2001). Effect of discrete wires on the implosion dynamics of wire array Z–pinches. *Physics of Plasmas*, 8:3734–3747.

Lebedev, S., Chittenden, J., Beg, F., et al. (2002). Laboratory astrophysics and collimated stellar outflows: The production of radiatively cooled hypersonic plasma jets. *Astrophysical Journal*, 564:113–119.

Lee, R. W. (1995). *The How to for FLY*. Manual for computer programme. Unpublished.

Lee, R. W. (1996). A time-dependent model for plasma spectroscopy of K–shell emitters. *J. Quant. Spectrosc. Radiat. Transfer*, 56(4):535–566.

Liberman, M. A., De Groot, J. S., Toor, A., and Spielman, R. B. (1999). *Physics of High–Density Z–pinch Plasmas*. Springer–Verlag, New York, USA. ISBN 0-387-98568-9.

Lide, D., editor (1999). *CRC Handbook of Chemistry and Physics*. CRC Press, Boca Raton, Florida, 80th edition. ISBN 0849304806.

Lindemuth, I. (1990). Two-dimensional fiber ablation in the solid-deuterium Z–pinch. *Physical Review Letters*, 65(2):179–182.

Lindemuth, I., McCall, G., and Nebel, R. (1989). Fiber ablation in the solid-deuterium Z–pinch. *Physical Review Letters*, 62:264–267.

Lindemuth, I., Reinovsky, R., Chrien, R., et al. (1995). Target plasma formation for magnetic compression/magnetized target fusion (MAGO/MTF). *Physical Review Letters*, 75:1953–1956.

Linhart, J. (1961). Dynamic stability of a conducting cylindrical shell in a magnetic field. *Journal of Applied Physics*, 32:500.

Linhart, J. (1994). Z–pinch trigger an axial nuclear detonation. In Haines, M. and Knight, A., editors, *Third International Conference on Dense Z–Pinches 1993*, pages 664–674, New York. American Institute of Physics.

Lorenz, A., Beg, F., Ruiz-Camacho, J., Worley, J., and Dangor, A. (1998). Influence of a prepulse current on a fiber Z–pinch. *Physical Review Letters*, 81:361–364.

Lorenz, A., Peacock, N., O'Mullane, M., and Neely, D. (1999). Diagnostic characterization of a prepulsed carbon fiber Z-pinch using spectral line intensity analyses. *Review of Scientific Instruments*, 70:1425–1429.

Matzen, M. (1997). Z-pinchers as intense X-ray sources for high-energy density physics applications. *Physics of Plasmas*, 4(5):1519–1527.

Matzen, M. (1999). Z-pinchers as intense X-ray sources for inertial confinement fusion applications. *Fusion Engineering and Design*, 44:287–293.

Matzen, M., Deeney, C., Leeper, R., et al. (1999). Fast Z-pinchers as dense plasma, intense X-ray sources for plasma physics and fusion applications. *Plasma Physics and Controlled Fusion*, 41:A175–a185.

McGeoch, M. (1998). Radio-frequency preionized xenon Z-pinch source for extreme ultraviolet lithography. *Applied Optics*, 37:1651.

Metzner, J., Bos, T., Wolf, J., and Langhoff, H. (1996). Search for optical amplification of the Balmer  $\alpha$  transition in C VI using a dynamical Z-pinch discharge. *Journal of Physics D: Applied Physics*, 29:1532–1539.

Michette, A. (1986). *Optical Systems for Soft X-Rays*. Plenum, London, 1st edition.

Mitchell, I., Aliaga-Rosset, R., Chittenden, J., Robledo, A., Schmidt, H., and Haines, M. (1998). Investigation of electron and ion beams in mega-ampere fiber pinch plasmas. *IEEE Transactions on Plasma Science*, 26:1267–1273.

Mitchell, I., Bayley, J. M., Chittenden, J. P., et al. (1996). A high impedance mega-ampere generator for fiber Z-pinch experiments. *Review of Scientific Instruments*, 67(4):1533–1541.

Nemeček, V. (2002). *Vlnovodné difraktivní struktury*. Diploma Thesis. Czech Technical University, Prague.

NIST (2005). NIST atomic spectra database. <http://physics.nist.gov/PhysRefData/ASD/index.html>.

NTF (2005). Dense Z-pinch program. [http://physics.unr.edu/facility/ntf/article/\\$Z\\$--pinch.html](http://physics.unr.edu/facility/ntf/article/$Z$--pinch.html).

Olson, R., Porter, J., Chandler, G., et al. (1997). Inertial confinement fusion ablator physics experiments on Saturn and Nova. *Physics of Plasmas*, 4:1818–1824.

Palmer, C. (2001). Diffraction grating handbook. <http://www.gratinglab.com/library/handbook4/>.

Pereira, N. and Davis, J. (1988). X-rays from Z–pinches on relativistic electron–beam generator. *Journal of Applied Physics*, 64:R1–R27.

Peterson, D., Bowers, R., McLenithan, K., et al. (1998). Characterization of energy flow and instability development in two-dimensional simulations of hollow Z pinches. *Physics of Plasmas*, 5:3302–3310.

Pikuz, S., Shelkovenko, T., Mingaleev, A., Hammer, D., and Neves, H. (1999a). Density measurements in exploding wire–initiated plasmas using tungsten wires. *Physics of Plasmas*, 6:4272–4283.

Pikuz, S., Shelkovenko, T., Sinars, D., Greenly, J., Dimant, Y., and Hammer, D. (1999b). Multiphase foamlike structure of exploding wire cores. *Physical Review Letters*, 83:4313–4316.

Pikuz, S. A. (2001). *X-ray radiography*. Summer school on High Current Plasma Experiment and Diagnostics, Kudowa Zdroj, Poland, 2001.

Plasmas International (2005). Perspectives on plasmas. <http://www.plasmas.org/fusion-icf.htm>.

Porter, J., Spielman, R., Matzen, M., et al. (1992). Resonant photopumping in a neon gas cell irradiated by a sodium Z–pinch. *Physical Review Letters*, 68(6):796–799.

Rahman, H., Wessel, F., and Rostoker, N. (1995). Staged Z–pinch. *Physical Review Letters*, 74:714–717.

Riley, R., Scudder, D., Shlachter, J., and Lovberg, R. (1996). Instability heating of a solid fiber Z–pinch. *Physics of Plasmas*, 3(4):1314–1323.

Riordan, J., Pearlman, J., Gersten, M., and Rauch, J. (1981). Sub-kilovolt X–ray emission from imploding wire plasmas. In Attwood, D. and Henke, B., editors, *Proceedings of the Topical Conference on Low Energy X-Ray Diagnostics, AIP conference proceedings*, vol. 75, pages 35–43, APS, New York. American Institute of Physics.

Robledo, A., Mitchell, I., Aliaga-Rossel, R., Chittenden, J., Dangor, A., and Haines, M. (1997). Time-resolved energy measurement of electron beams in fiber Z–pinch discharges. *Physics of Plasmas*, 4:490–492.

Rocca, J., Beethe, D., and Marconi, M. (1988). Proposal for soft X–ray and XUV lasers in capillary discharges. *Optics Letters*, 13:565.

Rocca, J., Shlyaptsev, V., Tomasel, F., Cortazar, O., Hartshorn, D., and Chilla, J. (1994). Demonstration of a discharge pumped table–top soft X–ray laser. *Physical Review Letters*, 73:2192–2195.

Rochau, G., Morrow, C., and Pankuch, P. (2003). A concept for containing inertial fusion energy pulses in a Z–pinch–driven power plant. *Fusion Science and Technology*, 43:447–455.

Rudakov, L. and Sudan, R. (1997). MHD turbulence in radiating intense Z–pinches. *Physics Reports*, 283:253–263.

Rudakov, L., Velikovich, A., Davis, J., Thornhill, J., Giuliani, J., and Deeney, C. (2000). Buoyant magnetic flux tubes enhance radiation in Z–pinches. *Physical Review Letters*, 84:3326–3329.

Ruiz, C., Cooper, G., Slutz, S., et al. (2004). Production of thermonuclear neutrons from deuterium–filled capsule implosions driven by Z–pinch dynamic hohlraums. *Physical Review Letters*, 93:015001.

Ryutov, D., Derzon, M., and Matzen, M. (2000). The physics of fast Z–pinches. *Reviews of Modern Physics*, 72(1):167–223.

Ryutov, D. and Remington, B. (2002). Scaling astrophysical phenomena to high–energy–density laboratory experiments. *Plasma Physics and Controlled Fusion*, 44:B407B423.

Ryutov, D. and Siemon, R. (2001). Magnetized plasma configurations for fast liner implosions: A variety of possibilities. *Comments on Modern Physics*, 2:C185–C201.

Saint–Gobain, Crystals & Detectors (2005). Saint–Gobain, Crystals & Detectors. <http://www.bicron.com>.

Sanford, T., Allshouse, G., Marder, B., et al. (1996). Improved symmetry greatly increases X-ray power from wire–array Z–pinches. *Physical Review Letters*, 77:5063–5066.

Sarkisov, G., Sasorov, P., Struve, K., et al. (2002). Polarity effect for exploding wires in a vacuum. *Physical Review E*, 66:046413.

Sarkisov, G., Struve, K., and McDaniel, D. (2004). Effect of current rate on energy deposition into exploding metal wires in vacuum. *Physics of Plasmas*, 11:4573–4081.

Scheffel, J., Arber, T., Coppins, M., and Russell, P. (1997). Kinetic stability of the finite electron temperature Z–pinch. *Plasma Physics Controlled Fusion*, 39:559–568.

Schulz (2002). Schulz scientific instruments. <http://www.schulz-si.com/si/index.html>.

Scudder, D. (1985). Experiments on high-density Z–pinches formed from solid deuterium fibers. *BAPS*, 30:1408.

Scudder, D., Shlachter, J., Forman, P., Riley, R., and Lovberg, R. (1994). Fiber Z–pinch instabilities. In Haines, M. and Knight, A., editors, *Third International Conference on Dense Z–Pinches 1993*, pages 503–508, New York. American Institute of Physics.

Scudder, D., Shlachter, J., Hammel, J., et al. (1990). The Los Alamos megamp fiber Z–pinch experiment. In Ortolani, S. and Sindoni, E., editors, *Proceedings of the Workshop on Physics of Alternative Magnetic Confinement Schemes*, pages 519–525, Bologna, Italy. Editrice Compositori.

Sethian, J. (1997). The quest for a Z–pinch based fusion energy source – a historical perspective. In Pereira, N., Davis, J., and Pulsifer, P., editors, *Fourth International Conference on Dense Z–Pinches*, pages 3–10, Woodbury, New York. American Institute of Physics.

Sethian, J., Robson, A., Gerber, K., and DeSilva, A. (1987). Enhanced stability and neutron production in a dense Z–pinch plasma formed from a frozen deuterium fiber. *Physical Review Letters*, 59(8):892–899.

Sethian, J., Robson, A., Gerber, K., and DeSilva, A. (1989). The NRL frozen deuterium fiber Z–pinch experiment. In Pereira, N. R., Davis, J., and Rostoker, N., editors, *Second*

*International Conference on Dense Z–Pinches*, pages 308–314, New York. American Institute of Physics.

Sethian, J., Robson, A., Gerber, K., and DeSilva, A. (1990a). Dense Z–pinches from D<sub>2</sub>, CD<sub>2</sub> and C fibers. In *1990 IEEE International Conference on Plasma Science*, page 105, New York, NY, USA. IEEE.

Sethian, J., Robson, A., Gerber, K., and DeSilva, A. (1990b). Evolution of a deuterium fiber Z–pinch driven by a long current pulse. In Ortolani, S. and Sindoni, E., editors, *Proceedings of the Workshop on Physics of Alternative Magnetic Confinement Schemes*, pages 511–518, Bologna, Italy. Editrice Compositori.

Sheehey, P., Hammel, J., Lindemuth, I., et al. (1992). Two-dimensional direct simulation of deuterium–fiber–initiated Z–pinch with detailed comparison to experiment. *Physics of Fluids B*, 4(11):3698–3706.

Shevelko, A. (1996). Absolute measurements in the VUV spectral range with a luminescent detector. *Quantum Electronics*, 26:729–731.

Shin, H., Kim, D., and Lee, T. (1996). Soft–X–ray amplification in a capillary discharge. *Physical Review E*, 50:1376–1384.

Shlachter, J. (1990). Solid D<sub>2</sub> fiber experiments on HDZP–II. *Plasma Physics Controlled Fusion*, 32:1073–1081.

Siemon, R., Lindemuth, I., and Schoenberg, K. F. (1999). Why magnetized target fusion offers a low-cost development path for fusion energy. *Comments Plasma Physics and Controlled Fusion*, 18:363.

Sinars, D., Shelkovenko, T., Pikuz, S., et al. (2000a). The effect of insulating coatings on exploding wire plasma formation. *Physics of Plasmas*, 7:429–432.

Sinars, D., Shelkovenko, T., Pikuz, S., Greenly, J., and Hammer, D. (2000b). Exploding aluminum wire expansion rate with 1–4.5 kA per wire. *Physics of Plasmas*, 7:1555–1563.

Sincerny, P., Strachan, D., Frazier, G., et al. (1985). Performance of Double–Eagle. In *5<sup>th</sup> IEEE Pulsed Power Conference, Arlington, VA, USA*, pages 151–154, New York, NY, USA. IEEE.

Slutz, S., Bailey, J., Chandler, G., et al. (2003a). Dynamic hohlraum driven inertial fusion capsules. *Physics of Plasmas*, 10:1875–1882.

Slutz, S., Olson, C., and Peterson, P. (2003b). Low mass recyclable transmission lines for Z–pinch driven inertial fusion. *Physics of Plasmas*, 10:429–437.

Slutz, S., Olson, C., Rochau, G., et al. (2003c). Z–pinch driven fusion energy. In van Dam, H. and Kuijper, J., editors, *Proceedings of 10<sup>th</sup> International Conference on Emerging Nuclear Energy Systems*, pages 515–524. NRG, Petten, Netherlands.

Smirnov, V. (1991). Fast liners for inertial fusion. *Plasma Physics and Controlled Fusion*, 33:1697–1714.

Sorokin, S. and Chaikovsky, S. (2002). Soft X–ray production and spectrum measurements in imploded krypton liners. In Davis, J., Deeney, C., and Pereira, N., editors, *Fifth International Conference on Dense Z–Pinches*, pages 127–130, Melville, New York. American Institute of Physics.

Spielman, J., Deeney, C., Chandler, G., et al. (1997). PBFA–Z: a 60 TW/5 MJ Z–pinch driver. In Pereira, N., Davis, J., and Pulsifer, P., editors, *Fourth International Conference on Dense Z–Pinches*, page 101, Woodbury, New York. American Institute of Physics.

Spielman, R. and de Groot, J. (2001). Z pinches — A historical view. *Laser and Particle Beams*, 19:509–525.

Spielman, R., Deeney, C., Chandler, G., et al. (1998). Tungsten wire–array Z–pinch experiments at 200 TW and 2 MJ. *Physics of Plasmas*, 5:2105–2111.

Spielman, R., DeGroot, J., Nash, T., et al. (1994). Stagnation dynamics and heating mechanisms for wire array Z–pinch implosions. In Haines, M. and Knight, A., editors, *Third International Conference on Dense Z–Pinches 1993*, pages 404–420, New York. American Institute of Physics.

Spielman, R., Dukart, R., Hanson, D., et al. (1989). Z–pinch experiments on Saturn at 30 TW. In Pereira, N. R., Davis, J., and Rostoker, N., editors, *Second International Conference on Dense Z–Pinches*, pages 3–16, New York. American Institute of Physics.

Spielman, R. B., Baldwin, G. T., Leeper, R. J., Ruiz, C. L., and Cooper, G. (1991). Deuterium gas puff and  $\text{CD}_2$  fiber array Z–pinch experiments on Saturn. In *1991 IEEE International Conference on Plasma Science, IEEE cat. no. 91CH3037-9.*, pages 203–204.

Spitzer, L. (1962). *Physics of fully ionized gases*. Interscience Publishers, New York, USA. ISBN 0470817232.

Stallings, C., Nielsen, K., and Schneider, R. (1976). Multiple wire array load for high-power pulsed generators. *Applied Physics Letters*, 29:404.

Stamm, U. (2004). Extreme ultraviolet light sources for use in semiconductor lithography – state of the art and future development. *Journal of Physics D: Applied Physics*, 40:32443253.

Steden, C. and Kunze, H. (1990). Observation of gain at 18.22 nm in the carbon plasma of a capillary discharge. *Physics Letters A*, 151:534–537.

Stephanakis, S., Levine, L., Mosher, D., Vitkovitsky, I., and Young, F. (1972). Neutron production in exploding–wire discharges. *Physical Review Letters*, 29(9):568–569.

Stygar, W., Ives, H., Fehl, D., et al. (2004). X–ray emission from Z–pinches at  $10^7$  A: current scaling, gap closure, and shot–to–shot fluctuations. *Physical Review E*, 69:46403–1–20.

Sweeney, M. (2002). History of Z–pinch research in the U.S. In Davis, J., Deeney, C., and Pereira, N., editors, *Fifth International Conference on Dense Z–Pinches*, pages 9–14, Melville, New York. American Institute of Physics.

Sze, H., Coleman, P., Banister, J., et al. (2001). Efficient argon K–shell radiation from a Z–pinch at currents  $> 15$  MA. *Physics of Plasmas*, 8:3135–3138.

Tektronix (1987). *P6015 Probe*. TEK instruction material.

Tektronix, Inc. (2005). Oscilloscopes. <http://www.tek.com/Measurement/scopes/home.html>.

Teylers Museum (2005). Teylers museum. <http://www.teylersmuseum.nl>.

Thorne, A., Litzén, U., and Johansson, S. (1999). *Spectrophysics: Principles and Applications*. Springer–Verlag, Berlin, Germany.

Trubnikov, B. (1986). Particle acceleration and neutron production at the neck of plasma pinches. *Soviet Journal of Plasma Physics*, 12:271–283.

Turchi, P. and Baker, W. (1973). Generation of high–energy plasmas by electromagnetic implosion. *Journal of Applied Physics*, 44:4936.

van Hoff, P. (2005). Atomic line list. <http://www.pa.uky.edu/~peter/atomic/index.html>.

Velikovich, A., Clark, R., Davis, J., et al. (2005). Thermonuclear and Beam Fusion in Deuterium Z–Pinch Implosions: Theory and Modeling. In *6<sup>th</sup> International Conference on Dense Z–Pinches, AIP conference proceedings*.

Velikovich, A., Davis, J., Thornhill, J., Giuliani, J., Rudakov, L., and Deeney, C. (2000). Model of enhanced energy deposition in a Z–pinch plasma. *Physics of Plasmas*, 7:3265–3277.

Verner, D., Verner, E., and Ferland, G. (1996). Atomic data for permitted resonance lines of atoms and ions from H to Si, and S, Ar, Ca and Fe. *Atomic Data Nucl. Data Tables*, 64:1. Also available online: <http://www.pa.uky.edu/~verner/lines.html>.

Vikhrev, V. (1986). Mechanism for neutron production in Z–pinches. *Soviet Journal of Plasma Physics*, 12:262–270.

Vikhrev, V., Ivanov, V., and Koshelev, K. (1982). Formation and development of a micro–pinch region in a vacuum spark. *Soviet Journal of Plasma Physics*, 8:688–692.

Wagner, T., Eberl, E., Frank, K., Hartmann, W., Hoffmann, D., and Tkotz, R. (1996). Charge–exchange of plasma beams from instabilities in axial discharges and population inversion in highly charged ions. *Physical Review Letters*, 76(17):3124–3127.

Weinbrecht, E., McDaniel, D., and Bloomquist, D. (2003). The Z refurbishment project (ZR) at Sandia National Laboratories. In Giesselmann, M. and Neuber, A., editors, *Digest of Technical Papers. 14<sup>th</sup> IEEE International Pulsed Power Conference 2003*, pages 157–162. IEEE , Piscataway, NJ, USA.

Wessel, F., Etlicher, B., and Choi, P. (1992). Implosion of an aluminium plasma-jet onto a coaxial wire: a Z-pinch with enhanced stability and energy-transfer. *Physical Review Letters*, 69:3181–3184.

Young, F., Stephanakis, S., and Mosher, D. (1977). Neutron and energetic ion production in exploded polyethylene fibers. *Journal of Applied Physics*, 48(9):3642–3650.

## Appendix A

### APPLIED SPECTROSCOPIC METHODS

In order to introduce fundamental terms<sup>1</sup> and to describe spectroscopic methods, we present the basic theory of emission spectroscopy. As there are numerous spectroscopic methods (see, for example, Griem, 1964, 1974, 1997; De Michelis and Mattioli, 1981; Hauer et al., 1991; Thorne et al., 1999) we will deal only with those that were applied in our experiment. Besides the aforementioned papers, our approach was also inspired by several lectures of prof. H. J. Kunze and by the PhD thesis of one of his students (Aschke, 1999).

#### A.1 *Introduction*

The characteristic property of a plasma is the radiation in a large spectral range. Emission spectroscopy is therefore a diagnostic technique that has been applied to an evaluation of appropriate plasma parameters since the very beginning of plasma physics (Griem, 1964; De Michelis and Mattioli, 1981). By emission spectroscopy it is possible to measure plasma composition, electron temperature and density, ion temperature and density, electric and magnetic field, plasma motion or turbulence, plasma dynamics, ionization dynamics, etc. (Kunze, 1989). However, to obtain some information about a plasma, a lot of things have to be taken into account to exclude misinterpretation. That is also the reason why we would like to briefly delineate the process of how the plasma emission is formed. We shall start with radiative and collisional processes which influence the population of energy levels and hence the local emissivity of a plasma. After that we will deal with radiative transfer. And finally we will describe how the plasma parameters were estimated.

---

<sup>1</sup> Partial LTE, optical depth, rate equations, etc.

## A.2 Radiative Processes

Radiative processes in a plasma can be divided into three main groups according to the type of transition. We can distinguish transitions (i) between free and free electrons, (ii) between free and bound electrons, and (iii) between bound and bound electrons.

- *Free–free transitions* are associated with a gain or loss of an electron energy in the field of an ion<sup>2</sup>. The loss of the electron energy into the radiation is connected with the deceleration of electrons and that is why we speak about Bremsstrahlung. The absorption of a photon by an electron is called the inverse Bremsstrahlung. Free states are not quantised, therefore radiation/absorption is characterised by a broad continuum.
- *Free–bound transitions* correspond to the radiative recombination and photoionization processes. Recombination continuum extends from each bound state of an electron and is characterised by edges. Similarly, the absorption edges occur in the spectral dependence of the photoionization cross–section.
- *Bound–bound transitions* occur when an electron bounded by an ion makes a transition to another bound state. When the final state has lower energy than the initial one, the photon of well–defined energy is emitted. The inverse mechanism is the photoexcitation. The radiation is characterised by emission or absorption spectral lines.

The rate of spontaneous emission from an upper energy level “u” to a lower level “l” is defined by means of the Einstein probability coefficient  $A_{ul}$  as follows:

$$\left. \frac{dn_u}{dt} \right|_{u \rightarrow l} = -A_{ul} n_u \quad (A.1)$$

where  $n_u$  is the number density of electrons in the upper level. The overall rate of spontaneous radiative transitions from the upper level “u” is given by the sum of the rates from the upper level “u” to all lower levels

$$\frac{dn_u}{dt} = - \sum_{l < u} A_{ul} n_u = -A_{u \rightarrow} n_u \quad (A.2)$$

---

<sup>2</sup> The collision between two electrons cannot produce radiation by electric or magnetic dipole processes.

It is quantum electrodynamics that treats of the transition probability  $A_{ul}$  and offers selection rules. As far as our experiments with carbon fibres are concerned, we identified only (allowed) electric dipole transitions with  $\langle l|e\vec{r}|u\rangle \neq 0$ . The intercombination (spin-forbidden  $\Delta S \neq 0$ ) lines are not usually observed for low- $Z$  elements, such as carbon, where the spin-orbit interaction is small.

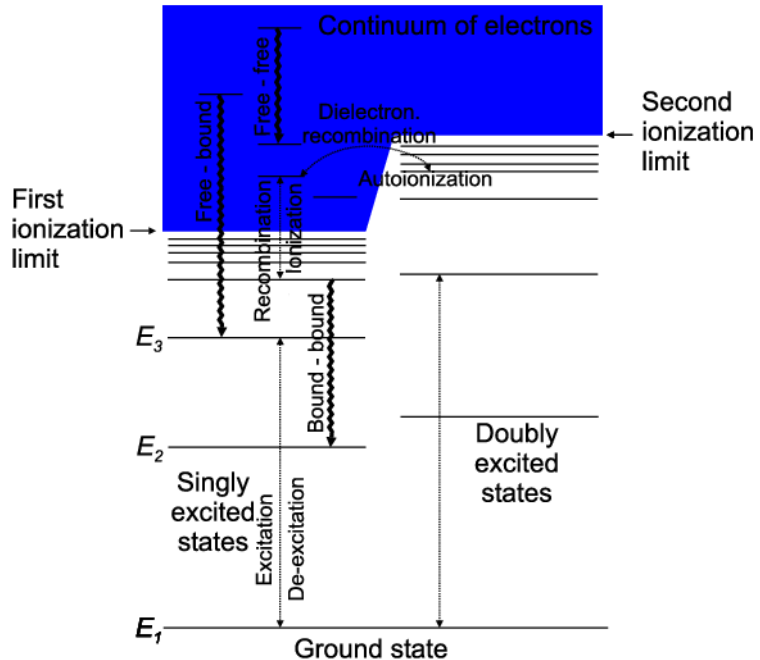
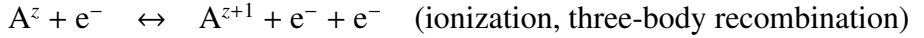


Fig. A.1: Several possible radiative and collisional processes. (Radiative processes are illustrated as wavy lines.)

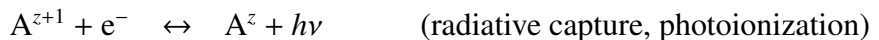
### A.3 Collisional Processes in Plasma

Similarly to radiative processes, we can distinguish between *collisional* excitation – de-excitation, ionization – recombination, etc. But on the contrary to radiative processes, collisional transitions between two states do not follow any selection rules. The crucial collisional process in a plasma is an *interaction of a bound electron with free electrons*. The collision of a bound electron with ions is much less significant due to the substantial difference in mass.

When a free electron collides with an electron bounded in an ion A, excitation or ionization of a bound electron can occur:



In three-body recombination, i.e. the inverse of collisional ionization, an excited bound state of the ion  $A^z$  is formed and the excess energy is given to a free (non-captured) electron. The cross-section of this reaction is increasing with the square of the electron density  $n_e$  and is larger for transitions into highly excited levels. On the contrary to that, the radiative capture (radiative recombination) of an electron occurs mainly into the ground state:



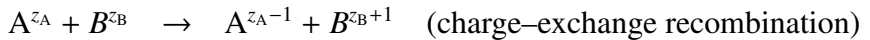
In the case of a high-temperature and low density plasma ( $n_e < 10^{16} \text{ cm}^{-3}$ ), the dominant recombination process is dielectronic recombination: a free electron is resonantly captured into an excited level, with simultaneous excitation of one of the electrons of the recombining ion  $A^{z+1}$ . A doubly-excited ion  $A^{z**}$  is formed:



As the doubly-excited state is above the first ionization limit of the recombined ion, it is highly unstable. The two electron excited state can either undergo the inversion process (autoionization) or radiatively decay by the emission of photons. Dielectronic recombination is responsible for the occurrence of satellite spectral lines on the long-wavelength side of resonance lines. Satellites on the long-wavelength side can be also emitted after the innershell excitation:



Lastly, we shall mention the charge-exchange recombination that happens during collision between two ions or between an ion and atom. When the charge of the ion A is greater than that of the ion B, the electron bounded in the ion A could be captured by the other ion B into a highly excited level:



The quantitative description of collisional processes begins with a microscopic cross-section  $\sigma(v)$ . The number of transitions “a” (of an ion A induced by electrons) per unit

time and per unit volume is given by equation

$$R_a = -\frac{dn_A}{dt} = \langle \sigma(v) \cdot v \rangle n_e n_A = C_a n_A \quad (\text{A.3})$$

where  $\langle \sigma(v) \cdot v \rangle = \int \sigma(v) f_e(v) v dv$  represents the so-called rate coefficient. The rate coefficient is calculated by the averaging of  $\sigma(v) \cdot v$  over the electron velocity distribution  $f_e(v)$ . For the excitation/deexcitation rate coefficient we usually use symbol  $X$ . Symbol  $S$  represents the ionization rate coefficient and symbol  $\alpha$  stands for the recombination coefficient. The quantity  $C_a$  is called the probability of collision “a” of one ion A with electrons.

## A.4 Charge State Distribution and Population of Energy Levels

The rate of radiative and collisional processes in a plasma determines the charge state distribution and population of each energy level.

### A.4.1 Charge state distribution

A given degree of ionization is given by ionization and recombination of two neighbouring ionization degrees as well as by diffusion and convection of ions. In principle, the charge state distribution can be solved from the equation of continuity

$$\frac{\partial n^z}{\partial t} + \nabla \cdot \Gamma_z = n_e (n^{z-1} S_{z-1} - n^z S_z) + n_e (n^{z+1} \alpha_{z+1} - n^z \alpha_z) \quad (\text{A.4})$$

where  $\Gamma_z$  stands for the flux density of ions with the charge  $z$ .

Some simplification can be made if transport of ions is neglected, i.e.

$$\frac{\partial n^z}{\partial t} = n_e (n^{z-1} S_{z-1} - n^z S_z) + n_e (n^{z+1} \alpha_{z+1} - n^z \alpha_z) \quad (\text{A.5})$$

In Z–pinch plasmas, one has to usually solve a time–independent system of equations

$$0 = n_e (n^{z-1} S_{z-1} - n^z S_z) + n_e (n^{z+1} \alpha_{z+1} - n^z \alpha_z) \quad (\text{A.6})$$

which leads to the so-called *ionization equilibrium*. This set of rate equations could be solved if plasma parameters and the recombination and ionization rate coefficients  $\alpha$ ,  $S$  are known.

### A.4.2 Level populations

Once the calculation of the charge state distribution was described, we are going to discuss the level populations in the particular ionization stage of interest.

In order to simplify notation, the rate of all collisions filling the upper level “u” will be marked as  $R_{\rightarrow u}^c$ . Similarly, the rate of radiative processes will be marked as  $R_{\rightarrow u}^r$  and the rate of collisions depopulating the level “u” as  $R_{u \rightarrow}^c = C_{u \rightarrow} n_u = X_{u \rightarrow} n_e n_u$ . The symbol  $A_{u \rightarrow}$  will stand for the radiative decay of the level “u”. By using these quantities we can write the following rate equation

$$\frac{dn_u}{dt} = R_{\rightarrow u}^c + R_{\rightarrow u}^r - C_{u \rightarrow} n_u - A_{u \rightarrow} n_u \quad (\text{A.7})$$

Compared with atomic time constants  $\tau_u = 1/(A_{u \rightarrow} + C_{u \rightarrow})$ ,  $n_e$  and  $T_e$  change usually slowly. It means that the population density  $n_u$  could be assumed to be in quasi-equilibrium, i.e.  $dn_u/dt = 0$ . From the rate equation A.7 we therefore obtain the population of upper level in *collisional-radiative equilibrium*

$$n_u = \frac{R_{\rightarrow u}^c + R_{\rightarrow u}^r}{A_{u \rightarrow} + C_{u \rightarrow}} \quad (\text{A.8})$$

An analytic solution taking into account all processes is too complicated and so it is necessary to use numerical simulation (for our purposes we used the time-dependent atomic physics code FLY described in appendix B). However, simplification of equation A.8 is still possible in two limiting cases. The first case is a low density plasma with  $n_e < 10^{14} \text{ cm}^{-3}$  where the population follows the *corona equilibrium*. In what follows, we will restrict to the second limiting case, to a high density plasma in *local thermodynamic equilibrium* (LTE).

## A.5 Local Thermodynamic Equilibrium

The criterion for LTE is that the collisional rates must be much larger than radiative rates. The radiative terms in Eq. A.8 can be then neglected and we get

$$n_u = \frac{R_{\rightarrow u}^c}{C_{u\rightarrow}} = \frac{n_e X_{\rightarrow u}}{X_{u\rightarrow}} \quad (\text{A.9})$$

From the principle of the detailed balance<sup>3</sup> follows that

$$\frac{X_{l\rightarrow u}}{X_{u\rightarrow l}} = \frac{g_u}{g_l} e^{-\frac{E_u - E_l}{kT_e}} \quad (\text{A.10})$$

where  $g_u$ ,  $g_l$  are statistical weights for levels with energies  $E_u$  and  $E_l$ , respectively. Applying Eq. A.10 to any two levels in atomic species and combining it with Eq. A.9, it is possible to derive the well-known Boltzmann distribution for the level population densities

$$\frac{n_u}{n_l} = \frac{g_u}{g_l} e^{-\frac{E_u - E_l}{kT_e}} = \frac{g_u}{g_l} e^{-\frac{h\nu}{kT_e}} \quad (\text{A.11})$$

When we extend Boltzmann relation to continuum states (Griem, 1997) we can arrive at the Saha equation

$$\begin{aligned} \frac{n_e n^{z+1}}{n^z} &= 2 \frac{Q^{z+1}(T_e)}{Q^z(T_e)} \left( \frac{2\pi m_e k T_e}{h^2} \right)^{3/2} e^{-\frac{E_{\text{ion}}}{kT_e}} \\ \frac{n_e n^{z+1}}{n^z} &= 6.10^{21} \frac{Q^{z+1}(T_e)}{Q^z(T_e)} T_e^{3/2} e^{-\frac{E_{\text{ion}}}{T_e}} \quad [\text{eV; cm}^{-3}] \end{aligned} \quad (\text{A.12})$$

which describes the total densities of adjacent ionization stages  $n^z$  and  $n^{z+1}$ . The term  $+ze$  represents the effective charge.  $E_{\text{ion}}$  stands for an ionising energy of an ion/atom with the density  $n^z$ .  $Q(T_e)$  is the partition function defined by

$$Q^z(T_e) = \sum_i g_i^z \cdot e^{-\frac{E_i - E_l}{kT_e}} \quad (\text{A.13})$$

The sum goes over all bounded states  $i$ . The number of terms that are included in the partition function depends not only on the plasma temperature but also on the density.

Since the collision processes are dominant we can further assume that the velocities of ions and electrons are described by a Maxwell distribution with a temperature identical with that of the Boltzmann distribution.

---

<sup>3</sup> Every process must be balanced by its exact inverse.

To sum up, local thermodynamic equilibrium represents the equilibrium between particles. Then the plasma can be described by the Maxwell, Boltzmann and Saha distribution with the same temperature  $T_e$ . Temperature  $T_e$  may vary from one place to another, hence the name “local”. The *complete* thermodynamic equilibrium is further described by the Planck blackbody function for radiation energy with the same temperature  $T = T_e$  as previous distributions. This may not be valid for plasma in LTE where the radiation density could be below the blackbody level.

## A.6 Prerequisites for Local Thermodynamic Equilibrium

The first necessary condition of LTE is a Maxwell distribution of electron velocities.

Another condition is given by the validity of reducing equation A.8 to equation A.9. It means that inequality  $A_{u \rightarrow} \ll C_{u \rightarrow}$  has to be satisfied. Usually a factor of ten is considered as sufficiently high, i.e.  $10 A_{u \rightarrow} \leq C_{u \rightarrow}$ . Unfortunately, it is impossible to derive any easy criterion for *complete* LTE (i.e. for populations of all levels of all ionic states). The review of De Michelis and Mattioli (1981) provides the necessary, though not sufficient, criterion

$$n_e \geq 1.8 \times 10^{14} \sqrt{kT_e} \Delta E_{ul}^3 \quad [\text{eV; cm}^{-3}] \quad (\text{A.14})$$

This criterion is difficult to satisfy especially for the largest energy level difference  $\Delta E_{ul}$  in the level scheme. Nevertheless, for any value of density  $n_e$ , the collisions still dominate between high-lying levels. Level, above which excited states are in equilibrium with the ground state of the next ionization stage, is called thermal limit. Then we talk about a plasma in *partial* LTE. We use the following criterion (Griem, 1964)

$$n_e \geq 7 \times 10^{17} \frac{(z+1)^6}{n_{TH}^{17/2}} \sqrt{\frac{kT_e}{E_H}} \quad [\text{eV; cm}^{-3}] \quad (\text{A.15})$$

that determines the minimal electron density  $n_e$  which is needed for partial LTE of levels above the principal quantum number  $n_{TH}$ . Here  $z$  is the effective nuclear charge and  $E_H \doteq 13,6 \text{ eV}$  is the ionization energy of hydrogen.

As regards our experiment, it follows from equation A.15 that the LTE approximation cannot be applied for K-shell lines of carbon ions. However, if the electron density is higher than a few times of  $10^{19} \text{ cm}^{-3}$ , PLTE may be valid for levels  $n \geq 2$  of Li-like oxygen ions (see Fig. 4.28 on page 105).

## A.7 Radiative Transfer

Until now we have been interested in the influence of collisional and radiative processes on the population of energy levels. It was important since the population of energy level  $n_u$  and the transition probability of spontaneous emission  $A_{ul}$  determine the local emission in a plasma. The local emission is described by the emissivity, the power emitted per unit solid angle per Hz by unit volume

$$\epsilon_\nu = \frac{d^3\Phi}{dVd\Omega d\nu} \quad (A.16)$$

The emissivity is given by all radiative transitions  $u \rightarrow l$

$$\epsilon(u \rightarrow l) = \frac{h\nu}{4\pi} A_{ul} n_u \quad (A.17)$$

The importance of emissivity lies in the fact that it contains information about local properties of the plasma. However, it is impossible to measure the emissivity directly by passive emission spectroscopy. We usually measure the spectral radiance  $L_\nu$  at the surface of a plasma: the power emitted per unit solid angle per Hz by unit projected area

$$L_\nu = \frac{d^3\Phi}{dA \cos \theta d\Omega d\nu} \quad (A.18)$$

The relation between these two quantities is trivial only in the case of an optically thin plasma where the absorption and re-emission of photons are neglected. Otherwise we have to solve the equation of radiative transport, which may be written for the line of sight along the  $x$ -axis as

$$dL_\nu(\vec{r}, \Omega) = \left[ \epsilon_\nu(\vec{r}, \Omega) - \kappa(\nu, \vec{r}) L_\nu(\vec{r}, \Omega) \right] dx \quad (A.19)$$

Here  $\kappa(\nu, \vec{r})$  represents the effective absorption coefficient that could be negative if stimulated emission occurs. Now we shall define a quantity called the source function  $S_\nu(\vec{r})$ .

It can be expressed as the ratio of the emissivity to the absorption coefficient

$$S_\nu(\vec{r}, \Omega) = \frac{\epsilon_\nu(\vec{r}, \Omega)}{\kappa(\nu, \vec{r})} \quad (A.20)$$

And by using the optical depth  $\tau(\nu, \vec{r})$

$$d\tau(\nu, \vec{r}) = \kappa(\nu, \vec{r})dx \quad (\text{A.21})$$

we can rewrite equation A.19 as follows:

$$\frac{dL_\nu(\vec{r}, \Omega)}{d\tau(\nu, \vec{r})} = S_\nu(\vec{r}, \Omega) - L_\nu(\vec{r}, \Omega) \quad (\text{A.22})$$

Unfortunately, this equation cannot be solved in general because the emissivity and absorption coefficient may have different spectral dependence. Moreover, the absorption of photons influences the population of energy levels and thus it is necessary to solve the equation A.22 together with the system of equations A.7.

The solution of equation A.22 can be found only in limiting cases. If we suppose the homogenous plasma with the characteristic length along the line of sight  $l_\Omega$  and the spatially isotropic source function  $S_\nu$ , we arrive at the relation

$$L_\nu = S_\nu(1 - e^{-\tau(\nu)}) \quad (\text{A.23})$$

where  $\tau(\nu) = \int d\tau(\nu, \vec{r}) = \kappa(\nu)l_\Omega$ .

One of the limiting cases occurs when the plasma is optically thin ( $\tau \ll 1$ ), i.e. without absorption, we can use the Taylor series  $e^{-\tau(\nu)} \approx 1 - \tau(\nu)$ . Then we obtain

$$L_\nu \approx \int \epsilon_\nu(\vec{r}, \Omega)dx = \epsilon_\nu l_\Omega \quad (\text{A.24})$$

Another limiting case is when  $\tau \gg 1$ . Then we can derive

$$L_\nu = S_\nu = \frac{\epsilon_\nu}{\kappa(\nu)} = \frac{2h\nu^3}{c^2} \cdot \frac{1}{e^{h\nu/kT} - 1} \quad (\text{A.25})$$

The last equality in equation A.25 is valid only in the case of the plasma in LTE. The limiting case  $\tau \gg 1$  is not reached in the entire spectral range. Since the absorption increases with  $\lambda^2$ , the plasma becomes optically thick towards long wavelength (Kunze, 1989). As far as shorter wavelengths are concerned, the emission lines become optically thick more readily than continuum.

From the spectroscopic point of view, it is necessary to recognise whether a spectral line is optically thick. For Doppler-broadened lines and the plasma in LTE, the optical thickness at the line centre  $\nu_0 = c/\lambda_0$  is given by

$$\tau(\nu_0) = r_B \sqrt{\frac{\pi M_i c^2}{2kT}} \lambda_0 f_{lu} n_l l_\Omega \quad (\text{A.26})$$

where  $r_B = e^2/4\pi\epsilon_0 m_e c^2$  is the classical (Bohr) electron radius. When substituting known constants in the previous equation, we get the relation

$$\tau(\nu_0) \doteq 1,08 \cdot 10^{19} \sqrt{\frac{M_i}{2kT}} \lambda_0 f_{lu} n_l l_\Omega \quad (\text{A.27})$$

Here the ion mass  $M_i$  is in atomic units  $m_u$ , temperature  $kT$  is in eV, the population of lower level  $n_l$  is in  $\text{m}^3$ , the wavelength  $\lambda_0$  is in nm, and the length of plasma  $l_\Omega$  is in m.

Whether the emission lines are optically thick or thin, can be checked experimentally by comparing relative intensities of close multiplet lines. The radiance ratio of two optically thin multiplet lines is determined by the statistical weights of lower levels  $g_l$  and the oscillator strengths  $f_{lu}$

$$\frac{L_{\nu_1}}{L_{\nu_2}} = \frac{f_{l_1 u_1} g_{l_1}}{f_{l_2 u_2} g_{l_2}} \quad (\text{A.28})$$

If the measured ratio is higher in favour of the weaker line, the spectral lines are not optically thin. As a result, the temperature cannot be easily determined by the intensity ratio of these spectral lines.

As regards our experiment, we found that the C VI Ly- $\alpha$  line and O VI 2p–3d line were almost always optically thick.

## A.8 Intensity of Spectral Lines

In the scientific literature there is often used the term *intensity* of a spectral line  $I$ . The fact of the matter is that the correct term is the spectral radiance  $L_\nu$  (mostly spatially and/or temporally integrated). However, as the term “intensity” became common, we use it in this thesis in spite of the fact that the spectral radiance would be more appropriate.

## A.9 Spectroscopic Measurements of Plasma Parameters

The emission spectroscopy of plasma belongs to one of the fundamental passive diagnostic technique. The emissivity of plasma contains much information about plasma properties and dynamics. The key issue is the choice of a suitable method which enables the estimation of plasma parameters, especially the electron temperature and density. Our choice of a method was predetermined by the properties of our grating spectrograph (see subsection 3.5.5 on page 52). The spectrograph enabled us to measure relative intensities of spectral lines only. The measurement of line profile was not possible due to limited spectral resolution. That is why the manifold choices of spectroscopic techniques (cf. Griem, 1964, 1997; De Michelis and Mattioli, 1981) are reduced to only several fundamental methods.

### *Spectroscopic measurement of temperature and density*

First, it is important to mention that spectroscopic measurement of temperature is actually the measurement of a parameter determining certain equilibrium distribution (Thorne et al., 1999). We can thus distinguish between the electron temperature  $T_e$  and the ion temperature  $T_i$ . Moreover, we can distinguish between the electron temperature occurring in the Maxwell velocity distribution, in the Boltzmann distribution A.11 (so-called population or excitation temperature), in the Saha–Boltzmann equation A.12 (ionization temperature), etc. Unless any equilibrium distribution exists, the temperature cannot be defined and the plasma has to be described by distribution functions themselves. Most of the spectroscopic temperature measurements primarily yield electron temperature  $T_e$ . The same was true in our case. The kind of the electron temperature (excitation, ionization, etc.) follows from the method used and it is not specified in our work.

In this thesis we applied the following spectroscopic methods of the temperature and density measurement:

- Very easy and undemanding method of a rough temperature measurement is the identification of ionic states in a plasma. It holds that an ionic state with ionization potential  $E_{\text{ion}}$  is reached in a plasma when the electron temperature obeys

$$T_e > C_i E_{\text{ion}} \quad (\text{A.29})$$

with  $C_i$  varying approximately between 0.1 and 0.3 (Hauer et al., 1991).

More accurate value of temperature can be obtained from calculation of ionization equilibrium (the temperature dependence of population of various ionic states). The free parameter in this calculation is the electron or ion density. To calculate ionization equilibrium we used atomic physics code FLY.

- Another common method is based on relative line intensities of the same ion. Provided that the plasma is in LTE or at least in partial LTE, the population of energy levels follows the Boltzmann distribution A.11. Then the ratio of two optically thin spectral lines is given by

$$\frac{L_\nu}{L_{\nu'}} = \frac{A_{ul}g_u\lambda'}{A_{u'l'}g_{u'}\lambda} \cdot e^{-(E_u - E_{u'})/kT_e} \quad (\text{A.30})$$

It can be clearly seen from Eq. A.30 that, except several constants, the ratio is dependent only on the electron temperature. The sufficient sensitivity is achieved for  $E_u - E_{u'} > kT_e$ . This method can be extended to a higher number of lines than two. We can make a graph with  $\ln(L_\nu\lambda/g_uA_{ul})$  on the  $x$ -axis and with the energy of upper level  $E_u$  on the  $y$ -axis. The slope of the line then equals  $-kT_e$ . This method was used in cases when the code FLY could not be applied, e.g. for Be-like ions.

- In the regions where (partial) LTE approximation is no more valid, the ratio of two spectral lines is not only temperature-, but also density-dependent. Under such circumstances a detailed accounting must be made of the ionization, recombination, excitation, deexcitation and radiative transfer. As far as this work is concerned, we used the code FLY not only to calculate the ratio of line intensities in non-LTE approximation (usually in collisional-radiative equilibrium) but also to reconstruct the whole synthetic spectrum for a particular temperature and density. Non-LTE requires more complicated treatment than LTE approximation, but on the other hand, it could provide the estimation of density which was very needed since the other methods of density measurement<sup>4</sup> cannot be applied.

---

<sup>4</sup> For instance, Stark broadening, depression of ionization potential, Inglis-Teller limit, the ratio of resonance and intercombination lines of He-like ions.

## Appendix B

### CODE FLY

#### B.1 Basic Parameters

FLY (Lee, 1995, 1996) is a commercially available suite of computer codes which was developed for analysing experiments where K–shell spectra<sup>1</sup> are observed. The FLY suite is capable of simulating K–shell emitters with the atomic number  $Z$  from 2 to 26, i.e. from helium to iron. The suite allows the user to calculate the population of the states in an LTE or non–LTE approximation by assuming steady–state or a time dependent evolution. The kinetics model FLY provides details of the level populations of hydrogen–, helium– and lithium–like ions. Less ionised species are represented as a ground state only. FLY is a “zero–dimension” suite of codes, thus the plasma is specified with the local conditions. The optical depth effects are approximated for a homogenous plasma “column” only. The most important characteristics of the suite can be summarised in the following items:

- 0-dimension post-processing of MHD.
- Atomic number  $Z$  from 2 to 26, i.e. from helium to iron.
- K–shell spectroscopy: detailed information on H–, He– a Li– like ion stages. K– shell satellite lines and also continuum radiation are included.
- Steady-state (either LTE, or non-LTE) as well as time–dependent solution of rate equations.
- Line profile synthesis: Doppler profile. Stark broadening for specific transition only.
- Effect of optical depth within the escape factor approximation.
- Possibility of external radiation field.
- Easy to use. Comparison of the synthetic spectrum with the experimental one.

---

<sup>1</sup> K–shell spectroscopy is engaged in the radiative transitions to the most inner shell (K–shell) of ions.

## *B.2 Description*

The suite of code consisted of three parts – FLY, FLYPAPER and FLYSPEC codes.

### *B.3 FLY*

The first code in the suite, FLY, calculates the level populations of hydrogen–, helium– and lithium–like ions. The population of energy levels can be solved either in non–LTE or LTE case. The rate equations for populations include the most relevant ionising, recombining, exciting and deexciting processes. The necessary input is the atomic number of interest together with the history of magnetohydrodynamic parameters. The other possible input is the grid of temperature and density for which the populations will be calculated. When the time history of plasma parameters is known, the code calculates a time–dependent evolution of the populations. When a grid of temperatures and densities is the input, the code computes a steady state approximation of population levels. The output file of the FLY code serves as an input into the other two codes of the suite — FLYPAPER and FLYSPEC.

### *B.4 FLYPAPER*

FLYPAPER code can be used to evaluate:

- populations of levels,
- the ratio of line intensities,
- optical depth

as a function of the time or plasma parameters (density and temperature).

### *B.5 FLYSPEC*

FLYSPEC code allows the reconstruction of the synthetic spectrum for a particular time or for particular temperature and density. The line profiles can be calculated for certain transitions: the Lyman and Balmer series for hydrogen–like ions,  $1s^2 \ ^1S_0 - 1s np \ ^1P$  transitions for helium–like ions, and transitions to the ground levels 2s, 2p in the case of lithium–like ions. The recombination emission is calculated for mentioned series only. In addition, the user can perform integrations of spectra over time.

## *B.6 Code Limitation*

Firstly, it should be stressed that the FLY suite is a 0–dimension code. Therefore, the correct treatment of radiative transfer (which is a non–local problem especially where a density gradient occurs) is not possible. Moreover, only Doppler broadening is incorporated in the FLY code and therefore the optical depth effects are overestimated.

Secondly, if we need to obtain synthetic spectra of L– or M– shell emitters we also need to use another code than FLY. This is true also for detail description of a Li–like ionization state because a lower excited state (Be–like) is described only by a single ground state<sup>2</sup>. Since the FLYSPEC code includes recombination for certain transition only, the continuum spectrum is underestimated.

Thirdly, the appropriate use of any post–processors assumes that preceding MHD modelling of plasma evolution is not influenced by the fact that the detail radiative processes are not included. This condition may not be fulfilled in a strongly radiating plasma consisting of high–Z elements.

Fourthly, another serious problem represents non–Maxwellian distribution of electrons since it often occurs along the  $z$ –axis in a Z–pinch plasma and cannot be described by means of electron temperature.

Lastly, it should be mentioned that the FLYSPEC programme provides insufficient instrumental broadening. In order to compare the synthetic spectra with the experimental ones, we have to therefore process the synthetic spectra with a spreadsheet programme.

## *B.7 Platform*

The kernel of the suite FLY was written in FORTRAN77 language. Running the code does not require any atomic and spectroscopic data since they are internally included. Programme runs on any UNIX/Linux workstation as well as on desktop PC under MS–DOS.

---

<sup>2</sup> This restriction was overcome in FLYCHK, the extension of FLY (Chung et al., 2003).

## Appendix C

### DEUTERATED FIBRE EXPERIMENT ON S-300 FACILITY

We have studied fibre Z–pinch not only on a small device Z–150 but also on a large pulsed power facility S–300 in Moscow. This appendix presents the results that were accepted for publishing in *Physica Scripta* in 2006.

#### C.1 *Introduction*

The dense Z–pinches initiated from cryogenic deuterium fibres were investigated in the 80’s and 90’s in connection with the research of controlled thermonuclear fusion and radiative collapse (Scudder, 1985; Sethian et al., 1987; Decker and Kies, 1989; Lebedev et al., 1998). The plan was to heat and ionise the fibre from frozen deuterium and to confine the high density and high temperature plasma column within a small diameter. The fibres from deuterated polymer were also employed (Stephanakis et al., 1972; Young et al., 1977; Kies et al., 1991; Mitchell et al., 1998) because their discharge behaviour was roughly the same (cf. Lebedev et al., 1998) and at the same time they were easily available and could be handled much easier than the frozen deuterium ones. Unfortunately, the development of MHD instabilities and global expansion of a pinch column were observed from the very beginning of the discharge and so the idea of the fibre Z–pinch as a fusion reactor was abandoned.

The purpose of our fibre experiments on the S–300 generator was (i) to compare results with the wire–array implosion onto a central fibre (Klír et al., 2004a, 2005) and (ii) to study the generation of XUV and X–ray radiation together with the neutron production which gives insight into the acceleration of ions and hence into the processes taking place in Z–pinches.

## C.2 Apparatus and Diagnostics

### C.2.1 Current generator and Z–pinch load

So far most experiments with dielectric fibres have been pursued on high impedance (about  $1 \Omega$ ) pulsed power generators since they are better optimised to drive currents into a high impedance load, which a dielectric fibre surely is (cf. Mitchell et al., 1996). Despite this, however, we carried out fibre Z–pinch experiments on a low impedance S–300 generator (3.5 MA, 100 ns,  $0.15 \Omega$ , Cherenko et al., 1996) at the Kurchatov Institute in Moscow. The experiments were performed at a current level of 2 MA with a rise time of about 150 ns. The Z–pinch was formed in a vacuum chamber from a deuterated polyethylene fibre of 100  $\mu\text{m}$  diameter and 1 cm length.

### C.2.2 Diagnostics

In order to study dynamics of Z–pinch plasma, an extensive set of diagnostic tools was used. The diagnostic set–up is displayed in Fig. C.1.

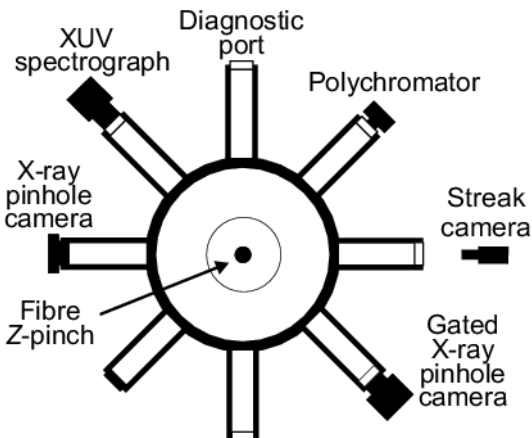


Fig. C.1: Diagnostic set–up on the S–300 generator, Moscow.

First, to provide time and space resolved information about visible emission, an optical streak camera was used. The streak camera was performed in the radial mode, i.e. with a slit parallel to the Z–pinch axis.

Second, X–ray radiation was detected with two X–ray pinhole cameras, XUV grazing incidence spectrograph, and 11-channel soft X–ray polychromator. One X–ray pinhole camera, which was gated, recorded 4 frames with 2 ns exposure and 10 ns inter-frame separation. All four frames were filtered with 24  $\mu\text{m}$  thick beryllium. The other pin-

hole camera, time-integrated and differentially filtered (without a filter, and with 5  $\mu\text{m}$  and 24  $\mu\text{m}$  mylar), was used to observe the plasma in various spectral ranges with the spatial resolution of 100  $\mu\text{m}$ . Even better spectral information was obtained by a time-integrated XUV grazing incidence spectrograph which recorded carbon K-shell lines. Time resolved studies of soft X-ray emission was conducted using an 11-channel polychromator. The various combinations of glancing incidence mirrors, transmission filters, and semiconductor detectors enabled the detection of photons in channels of 50, 80, 120, 180, 270, 365, 600, 800, 1000, 1200 and 2200 eV.

And finally, as far as neutrons are concerned, a time-of-flight analysis of neutrons was made possible by two axially positioned SSDI-8 scintillators at the distance of 2.70 m and 7.45 m (downstream). The neutron yield was measured by an indium activation counter. Since the activation counter has not been calibrated in situ and since we have some experimental evidence that the yield was underestimated by one order of magnitude, it is possible that the neutron yields should be multiplied by 10 throughout this article and references (Klír et al., 2004a, 2005).

## C.3 Experimental Results

### C.3.1 Current waveform and X-ray emission

The results of a number of diagnostic tools from the discharge no. 030606-1 are shown in Fig. C.2–C.5.

In Fig. C.2 we present the current waveform, optical streak photograph, and some X-ray characteristics. Time  $t = 0$  corresponds to the start of the current at the fibre. The streak photograph shows that the optical emission began early in the discharge. The optical emission was continuing for several hundreds of nanoseconds and its intensity was modulated by several peaks. Similarly, the soft X-ray power (measured by the 11-channel polychromator) was peaking more than once. The peak power of sub-keV radiation reached 30 GW near the maximum current. The total emitted energy exceeded 5 kJ.

Also, it could be observed that the pinch consisted of several distinct layers. We could distinguish a low density coronal plasma and higher density interior layers. The coronal plasma was expanding with the radial velocity of about  $2 \times 10^6$  cm/s (see Fig. C.2). Interior layers were displayed by the X-ray pinhole cameras (see Fig. C.3).

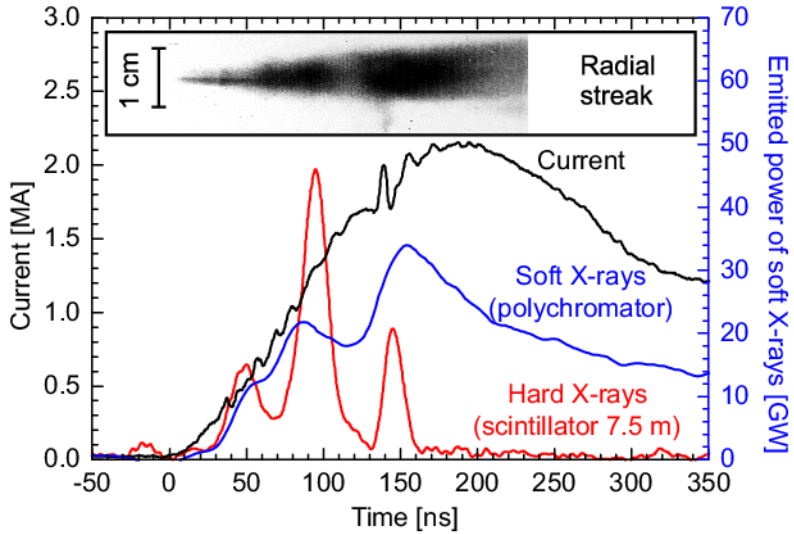


Fig. C.2: Current waveform, emitted power of soft X-rays, hard X-ray signal, and streak photograph, shot no. 030606-1.

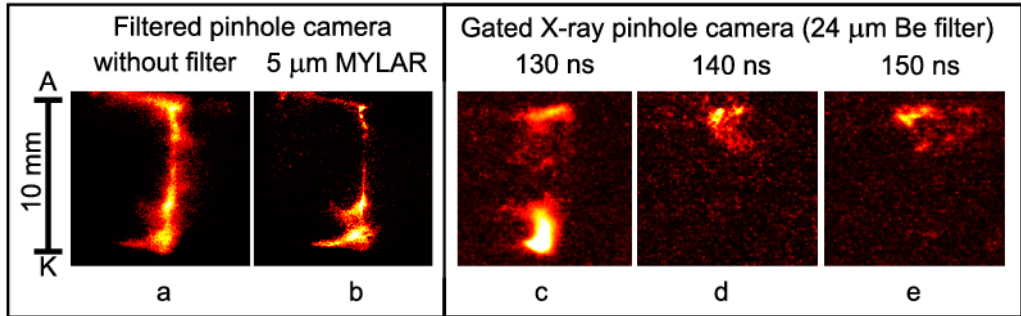


Fig. C.3: Time-integrated X-ray pinhole images and the sequence of gated X-ray images, shot no. 030606-1. The used filter and/or the time of exposure is shown on the top of each image.

The time-integrated soft X-ray images (Fig. C.3.a and C.3.b) show a radiating sub-millimetre core. Several bright spots were observed near the cathode and anode. Some of them were smaller than 100  $\mu$ m in diameter, i.e. smaller than the spatial resolution of the pinhole camera. At the peak of the soft X-ray pulse (Fig. C.3.d and C.3.e), the ‘harder’ radiation came from several bright spots near the anode. [Take note of the fact that the detection efficiency varied between sections of MCP detector. For that reason the decreasing emission recorded by the pinhole camera (Fig. C.3.c-C.3.e) did not correspond to the increasing power of soft X-rays (Fig. C.2).] Another noticeable feature in Fig. C.3 is the radiation from the anode which indicates runaway electrons in outer regions. On the basis of other experiments (Lebedev et al., 1998), we assume that the strong radiating plasma near the cathode (Fig. C.3.c) was the expanding electrode material.

Fig. C.4 presents the temporally and spatially integrated spectrum in the  $200 \div 600$  eV spectral range where K-shell lines of carbon ions occurred. The plasma parameters determination is somewhat problematic since the opacity effects with space- and time- dependence have to be taken into account. To simulate the spectrum with one temperature and one density was therefore impossible. Nevertheless, most features of the obtained spectrum were simulated with the “integrated” electron temperature  $T_e$  of 120 eV (cf. the synthetic spectrum in Fig. C.4). The estimation of the electron density  $n_e$  was ambiguous owing to its dependence on the choice of the optical path length  $l_\Omega$ . The only feature that was not included in the synthetic spectrum was the strong continuum of He-like ions. This continuum could originate from the part of plasma volume with higher density ( $n_e > 10^{21} \text{ cm}^{-3}$ ) and lower temperature ( $T_e < 120$  eV). As regards the emitted energy of the carbon Ly- $\alpha$  line, the 365 eV channel of the polychromator measured the total energy of about 30 J.

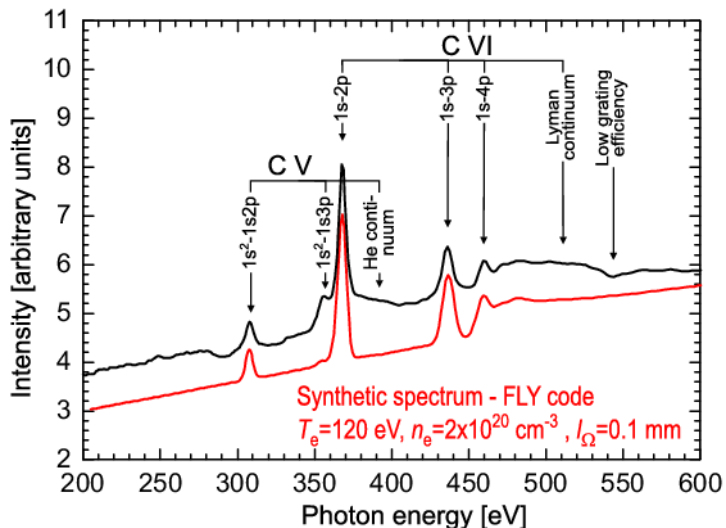


Fig. C.4: XUV spectrum in the  $200 \div 600$  eV spectral range, shot no. 030606-1.

### C.3.2 Neutron measurements

The results of neutron measurements are demonstrated on shot no. 030606-1 that was described above. In this shot, an indium activation counter detected the modest neutron yield of  $2 \times 10^7$ . The yield was calculated assuming the isotropic emission over a sphere.

Furthermore, we determined the production time and mean energy of neutrons from two time-of-flight scintillators situated at distances of 2.70 and 7.45 m away from the

pinch. The output from these two scintillators is shown in Fig. C.5. To make the graph in Fig. C.5 clear, X-ray pulses from both scintillators were placed over each other. The time-of-flight of X-rays and the delay of photomultiplier were included. Time  $t = 0$  corresponds to the start of the current and hence the time axis is the same as in Fig. C.2.

In Fig. C.5, three hard X-ray pulses emitted in shot no. 030606-1 can be seen. The time-of-flight analysis proved that each of X-ray pulses was accompanied with the neutron production. The X-ray pulse no. 1, 2, and 3 corresponded to the neutron pulses no. 1, 2, and 3, respectively. Most of the neutrons were emitted at the third hard X-ray pulse. As Fig. C.2 shows, the third X-ray pulse corresponded both to the peak of soft X-rays and to the noticeable change in the current waveform. The mean neutron energy (measured in the axial, downstream direction) of all three pulses was  $2.45 \pm 0.05$  MeV which corresponds to the D–D reaction.

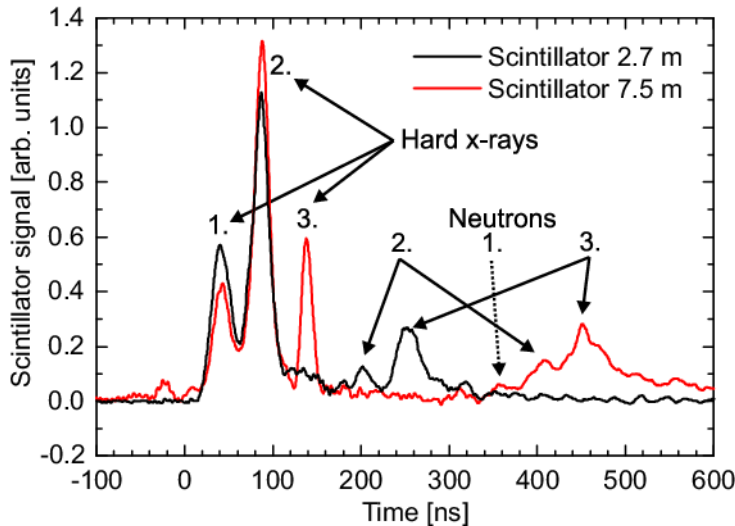


Fig. C.5: Scintillator signals in shot no. 030606-1, neutron yield  $2 \times 10^7$ .

## C.4 Discussion

The experimental results presented in this paper are similar to other fibre Z–pinch experiments. There was no indication of globally collapsing pinch although the Pease–Braginskii current (600 kA for polyethylene fibres) was exceeded. This rapid expansion is usually explained by the anomalous resistivity in a low density corona (Chittenden, 1995) and/or turbulent heating arising from MHD instability growth (Riley et al., 1996). As for MHD instabilities in our experiment, the evidence of an  $m = 0$  mode was given

by the X-ray pinhole camera which recorded bright spots.

The key issue of our experiment was the modest neutron yield of about  $10^7$  per one shot. Contrary to that, the neutron yields between  $10^9$  and  $10^{10}$  were typical in other fibre Z-pinch even with a lower current (cf. Stephanakis et al., 1972; Sethian et al., 1987; Kies et al., 1991; Mitchell et al., 1998; Lebedev et al., 1998). One of the possible explanations for that could be a diameter of a fibre used. Stephanakis et al. (1972) reported that neutron yield was decreasing with the increasing diameter of a fibre. For instance, 100  $\mu\text{m}$  diameter fibres produced ten times fewer neutrons than fibres of 20  $\mu\text{m}$  diameter. Another fact that could play an important role is the current generator. At this point we could mention the disappointing results and the modest neutron yield reported by Decker and Kies (1989) on a “low” impedance SPEED 2 generator.

Another significant result we obtained was the mean energy of neutrons, which was near the value of 2.45 MeV. In addition to that, the time of neutron production corresponded to the soft X-ray emission (cf. Fig. C.2 and Fig. C.5) and hence the detected neutrons could be of thermonuclear origin. This result would be consistent with the Z-pinch experiments initiated from thicker ( $> 40 \mu\text{m}$ ) fibres on the Gamble II (Young et al., 1977) and Kalif (Kies et al., 1991) generators. Such conclusion seems to be more optimistic than the beam-target mechanism reported on the Poseidon (Sethian et al., 1987) and MAGPIE (Mitchell et al., 1998) generators. However, the shift from 2.45 MeV could be too small to be identified. Therefore, it is still feasible that the neutron yield was caused by beam-target interactions at a relatively slow motion of dense plasma regions. The beam-target mechanism is also supported by the “integrated” electron temperature of 120 eV that is too low even for the modest neutron yield produced by thermonuclear way. This discrepancy was also observed by the HDZP group in Los Alamos National Laboratory. The explanation they proposed was the model of instability heating in which the ion temperature  $T_i$  was substantially higher than the temperature of electrons  $T_e$  (Riley et al., 1996). Ion temperature  $T_i$  higher than the electron temperature  $T_e$  was also observed during the stagnation in wire-array Z-pinch and was ascribed to ion viscous heating within fine-scale interchange instabilities (Haines et al., 2004). Another explanation how to reconcile the observed neutron yield with a low electron temperature is that only a small part of the plasma volume was heated to a sufficiently high temperature. Then the bulk of the plasma could remain cold. But even if the fusion mechanism were thermonuclear, it would still hold that the neutron yield was modest in our experiment

and that the yield higher than  $10^{10}$  has not been reported by other research groups.

Finally, we compare our fibre Z–pinch with the implosion of a wire–array onto a deuterated fibre. Both experiments were carried out on the same current generator S–300 with similar deuterated fibres and currents (Kl  r et al., 2004a, 2005). We found out that the neutron yield was one order of magnitude higher in the case of the implosion of a wire–array. Another difference we observed was a slight shift of the neutron mean energy from 2.45 MeV towards higher energies (Kl  r et al., 2005).

### *C.5 Conclusion*

The dense Z–pinch formed from a deuterated polyethylene fibre was studied on the “low” impedance S–300 pulsed power generator at the Kurchatov Institute. The majority of observed phenomena were in agreement with other fibre Z–pinch experiments carried out on “higher” impedance generators. The important result was obtained by the time–of–flight analysis which determined the mean neutron energy of about 2.45 MeV. However, the modest neutron yield of  $2 \times 10^7$  per shot was one order of magnitude lower than in our experiments with the implosion of a wire–array onto a fibre.

## Appendix D

### MATLAB SIMULATION OF $R-L-C$ CIRCUIT WITH TIME-DEPENDENT RESISTANCE

The equivalent circuit of our  $Z$ -pinch is shown in Fig. 3.6. We can substitute this circuit by the  $R-L-C$  circuit where  $C$  stands for  $C_0$ ,  $L$  stands for  $L_0 + L_P(t)$ , and  $R(t)$  stands for  $R_0 + R_P(t) + \dot{L}_P(t)$ . Because the plasma inductance  $L_P$  is much lower than  $L_0$  and depends on the pinch radius logarithmically, we consider the inductance  $L$  to be constant. It is therefore possible to solve the  $R-L-C$  circuit with a time-dependent resistance only.

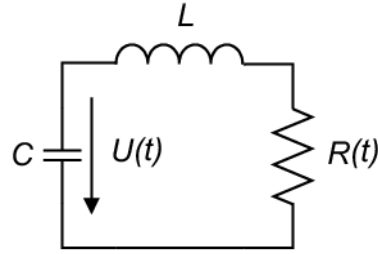


Fig. D.1:  $R-L-C$  circuit with a time-dependent resistance.

Then the voltage  $U(t)$  is given by

$$U(t) = U_0 - \int_0^t \frac{I(t')}{C} dt' = L \frac{dI(t)}{dt} + R(t)I(t) \quad (\text{D.1})$$

By differentiating this equation we obtain

$$-\frac{I(t)}{C} = L\ddot{I}(t) + R(t)\dot{I}(t) + \dot{R}(t)I(t) \quad (\text{D.2})$$

$$0 = \ddot{I}(t) + \frac{R(t)}{L}\dot{I}(t) + \left(\frac{\dot{R}(t)}{L} + \frac{1}{CL}\right)I(t) \quad (\text{D.3})$$

This ordinary differential equation was solved in MATLAB by the `ode45` function for various dependencies of resistance  $R(t)$ . We were looking for such resistance  $R(t)$  which produced  $U_P$  and  $dI/dt$  similar to experimentally measured waveforms.